Making and Breaking of Rydberg Atoms

VRIJE UNIVERSITEIT

Making and Breaking of Rydberg Atoms

ACADEMISCH PROEFSCHRIFT

ter verkrijging van de graad van doctor aan
de Vrije Universiteit Amsterdam,
op gezag van de rector magnificus
prof.dr. T. Sminia,
in het openbaar te verdedigen
ten overstaan van de promotiecommissie
van de faculteit der Exacte Wetenschappen \ Natuurkunde en Sterrenkunde
op donderdag 31 mei 2001 om 13.45 uur
in het hoofdgebouw van de universiteit,
De Boelelaan 1105

door

Cornelis Wesdorp

geboren te Amsterdam

Promotor: prof.dr. L.D. Noordam

"Most of the fundamental ideas of science are essentially simple, and may as a rule be expressed in a language comprehensible to everyone"

A. Einstein

"If you cannot, in the long run, tell everyone what you have been doing, your doing has been worthless"

E. Schrödinger

"Even for the physicist the description in plain language will be a criterion of the degree of understanding that has been reached"

W.K. Heisenberg

aan Ester

This thesis is based on the following publications:

Chapter 2	*Selective Field Ionization in Li and Rb, theory and experiment,* F. Robicheaux, C. Wesdorp, L.D. Noordam, Phys. Rev. A **62**, 43404 (2000)
Chapter 3	*Displacing Rydberg Electrons:* *The Mono-Cycle Nature of Half-Cycle Pulses,* C. Wesdorp, F. Robicheaux, L.D. Noordam, Phys. Rev. Lett., submitted for publication
Chapter 4	*The dynamics of Forced Autoionization,* C. Wesdorp, F. Robicheaux, L.D. Noordam, Phys. Rev. A **60**, R3377 (1999)
Chapter 5	*Half Cycle Microwave Stabilization of Rubidium Stark atoms,* C. Wesdorp, F. Robicheaux, L.D. Noordam, Phys. Rev. A **60**, 5122 (1999)
Chapter 6	*Field Induced Electron-Ion Recombination:* *A Novel Route towards Neutral (Anti-)matter,* C. Wesdorp, F. Robicheaux, L.D. Noordam, Phys. Rev. Lett. **84**, 3799 (2000)
Chapter 7	*Pulsed Field Recombination,* C. Wesdorp, F. Robicheaux, L.D. Noordam, Phys. Rev. A, submitted for publication
Chapter 8	*Rydberg Carbon Clusters, prepared by Pulsed Field Recombination,* C. Wesdorp, F. Robicheaux, L.D. Noordam, Chem. Phys. Lett. **323**, 192 (2000)
Chapter 10	*Pulsed Field Recombination,* C. Wesdorp, F. Robicheaux, L.D. Noordam, Nucl. Phys. A, accepted for publication
Chapter 11	*Antiwaterstof,* K. Wesdorp, T. Sonnemans, K. Eikema, T. Hijmans, B. Noordam, Nederlands Tijdschrift voor Natuurkunde (NTvN), jaargang 66, 6, 194 (2000)

In addition, the author participated in the following publications:

Dynamics of strongly perturbed Stark states in Ba,
F. Robicheaux, C. Wesdorp, L.D. Noordam,
Phys. Rev. A **60**, 1420 (1999)

Stepwise Electron Emission from Autoionizing Magnesium Stark States,
J.B.M. Warntjes, C. Wesdorp, F. Robicheaux, L.D. Noordam,
Phys. Rev. Lett. **83**, 512 (1999)

Supersnelle meting van stapsgewijze elektronen emissie,
M. Warntjes, K. Wesdorp, F. Robicheaux, B. Noordam,
Nederlands Tijdschrift voor Natuurkunde (NTvN), jaargang 65, 9, 266 (1999)

First Positron Cooling of Antiprotons,
G. Gabrielse, J. Estrada, J.N. Tan, P. Yesley, N. Bowden, P. Oxley, C. Storry,
M. Wessels, J. Tan, D. Grozonka, W. Oelert, G. Schepers, T. Sefsick, H. Fuhrman,
H. Zmeskal, W. Breunlich, H. Kalinowsky, C. Wesdorp, J. Walz, K. Eikema, T. Hänsch,
Phys. Lett. B, accepted for publication

The results of chapter 6-9 are reviewed in:

Coaxing Shy Particles Into an Atomic Jar,
A. Hellemans, Science, 788-789 (May 5, 2000)

Through the Looking Glass,
A. Hellemans, Nature, 556-558 (August 10, 2000)

An Insect Trap for Electrons,
Physical Review Focus, (April 21, 2000)

Promotiecommissie:

dr. H.J. Bakker
prof. dr. ing. J.F.J. van den Brand
prof. dr. W. Hogervorst
prof. dr. G.J.M. Meijer
prof. dr. F. Robicheaux
prof. dr. S. Stolte
prof. dr. J.T.M. Walraven

The experiments described in this thesis were performed at the following institutes:

FOM Institute for Atomic and Molecular Physics (AMOLF),
Kruislaan 407,
1098 SJ, Amsterdam, The Netherlands
http://www.amolf.nl

European Organization for Nuclear Research, CERN,
CH - 1211 Geneva 23, Switzerland
http://cern.web.cern.ch

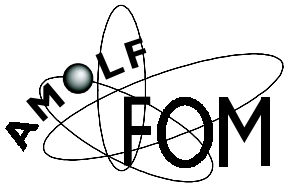

This work is part of the research program of the Stichting voor Fundamenteel Onderzoek der Materie (Foundation for Fundamental Research on Matter) and was made possible by financial support from the Nederlandse Organisatie voor Wetenschappelijk Onderzoek (Netherlands Organization for the Advancement of Research).

Contents

1 Introduction **13**
- 1.1 Making and Breaking . . . 13
- 1.2 Rydberg Atoms . . . 14
- 1.3 Ionization, Breaking of Rydberg Atoms . . . 16
- 1.4 Frustrated Breaking . . . 19
- 1.5 Recombination, Making of Rydberg Atoms . . . 19
- 1.6 Anti-Matter . . . 23

2 Selective Field Ionization **25**
- 2.1 Bound State Characterization . . . 25
- 2.2 Theoretical Method . . . 28
- 2.3 Matching Experiment with Theory . . . 32
- 2.4 Limitations of the Calculation . . . 37
- 2.5 Discussion and Conclusions . . . 37

3 THz Ionization of High Rydberg States **39**
- 3.1 Half-Cycle Pulse Ionization . . . 39
- 3.2 Experimental Realization . . . 42
- 3.3 Experimental Results . . . 43
- 3.4 Classical Calculations . . . 45
- 3.5 Discussion and Conclusions . . . 49

4 Forced Autoionization **51**
- 4.1 Introduction to Forced Autoionization . . . 51
- 4.2 Frequency Domain Experiments . . . 53
- 4.3 Time Domain Experiments . . . 54
- 4.4 Multi-Channel Quantum Defect Theory . . . 57
- 4.5 Discussion and Conclusions . . . 59

5 Frustrated Breaking **61**
- 5.1 Rydberg Atoms in Time-Dependent Electric Fields . . . 61
- 5.2 Experimental Realization . . . 62
- 5.3 Experimental Results: Frustrated Ionization . . . 64
- 5.4 Experimental Results: Lifetime Measurements . . . 65

5.5 Origin of the Oscillations . . . 65
5.6 Critical Slew Rate . . . 69
5.7 Connection to Other Experiments . . . 69

6 Pulsed Field Recombination 73
6.1 A Novel Recombination Scheme . . . 73
6.2 Experimental Realization . . . 75
6.3 Experimental Results and Classical Description . . . 77
6.4 Discussion and Conclusions . . . 79

7 Pulsed Field Recombination with a Penning Trap 81
7.1 The Pursuit of Anti-Hydrogen . . . 81
7.2 Scheme and Efficiency . . . 82
7.3 Experimental Realization . . . 84
7.4 Experimental Results . . . 87
7.5 Interaction Volume . . . 92
7.6 Discussion and Conclusions . . . 94

8 Rydberg Carbon Clusters Prepared by Pulsed Field Recombination 97
8.1 Why Rydberg Carbon Clusters? . . . 97
8.2 Pulsed Field Recombination Scheme . . . 98
8.3 Experimental Realization . . . 99
8.4 Results: Interaction Volume . . . 101
8.5 Results: Rydberg State Distribution . . . 101
8.6 Semi-Classical Calculations . . . 102
8.7 Discussion and Conclusions . . . 105

9 Pulsed Field Recombination at CERN 107
9.1 Introduction to Anti-Hydrogen . . . 107
9.2 Anti-Proton and Positron Trap at CERN . . . 108
9.3 Anti-Proton and Positron Detectors . . . 110
9.3.1 Non-Destructive Detection . . . 110
9.3.2 Destructive Detection . . . 112
9.4 Pulsed Field Recombination . . . 112
9.4.1 Experimental Realization . . . 112
9.4.2 Implementation of the PFR Scheme at ATRAP . . . 114
9.4.3 Integration of the Equations of Motion of a Charged Particle in the Trap . . . 115
9.4.4 Positron Pulses . . . 116
9.4.5 Calibrating the Electric Field in the Trap . . . 118
9.4.6 Pulsed Field Recombination . . . 119
9.5 Future Direction . . . 122

10 Summary **127**
10.1 Motivation of the Research . . . 127
10.2 Scheme and Efficiency . . . 128
10.3 Experimental . . . 129
10.3.1 Photoelectron Setup . . . 130
10.3.2 Penning Trap Setup . . . 131
10.4 Recombination of Lithium and Rubidium . . . 131
10.5 Recombination of Carbon Clusters . . . 133
10.6 Anti-Hydrogen . . . 134
10.7 Conclusions and Outlook . . . 135

11 Samenvatting **137**
11.1 Maken en breken van Rydberg atomen . . . 137
11.2 Wat is antimaterie? . . . 138
11.3 Wat maakt antiwaterstof interessant? . . . 141
11.4 Ingrediënten voor koud antiwaterstof . . . 142

Bibliography **145**

Nawoord **153**

Chapter 1

Introduction

1.1 Making and Breaking

There are many ways to destroy a state of matter and most often it is done without very much effort. The time inverse of destroying a state of many bodies may physically not be forbidden but can be difficult to achieve and highly improbable. With fewer bodies, a time reversed process is more likely. In this thesis we investigate how atoms can be destroyed, and how they can be made. That is to say, how an atom breaks apart into an electron and an ion, and how an electron and an ion make an atom. We restrict our studies to atoms in which the outer electron is in a highly excited orbit: the so called Rydberg atom. Rydberg atoms can be any atom in which the outer electron has a large principal quantum number (n) and can be seen as a quasi one-electron system. Since this electron is most often far away from the ionic core, it experiences effectively a $+1$ charge of the ion. Therefore the Rydberg atom closely resembles a hydrogen atom.

A careful study of the *breaking* of an atom often reveals new insights on atomic dynamics. To study the atomic dynamics, tools are required which probe the atom in a very precise manner. A laser is such a tool, and can be used to create, or destroy a Rydberg state. A very short laser pulse is required when the Rydberg atom is studied on an atomic timescale, and a laser with a very well defined energy (narrow bandwidth) is required when one tries to subtract energy information of a certain Rydberg state. A Voltage generator to produce (time varying) electric fields, is another tool to study the atomic dynamics of Rydberg atoms, since Rydberg states are easily perturbed by external fields. A strong electric field will break an Rydberg atom apart, but a strong time varying electric field can frustrate this breaking and make new Rydberg states.

The *making* of a Rydberg atom from an ion and an electron not only reveals information on atomic dynamics, but more importantly enables us to make bound states difficult to produce otherwise. Most commonly a Rydberg state is made by exciting an atom with a laser. In some cases laser-excitation fails and a Rydberg state cannot be made with the aid of a laser. In this thesis a new and efficient recombination scheme is described where we show that a well defined Rydberg state can be made by recombining an electron and an ion in a controllable manner. We foresee that this recombination scheme can be used

to recombine any sort of (molecular-)ion with an electron.

The same scheme can be used to produce neutral anti-matter, by recombining an anti-proton and a positron (anti-electron) into an anti-hydrogen atom. An anti-proton is very similar to a proton except for the most striking difference that it has opposite charge. The same holds for the positron and the electron. A lot is still unknown about anti-matter: for example, the sign and magnitude of the gravitational acceleration has not yet been measured on anti-matter. Neutral anti-matter would be much easier to use for such an experiment than charged anti-matter, for reasons we will discuss later. It would also be appealing to determine the energy levels of anti-hydrogen and compare them with hydrogen. This would be the first direct comparison of matter with anti-matter. Such a comparison can be used as a test for Quantum Field theories which predict the structure of anti-matter. In the following sections we describe some features of Rydberg atoms (section 1.2), how they break apart (section 1.3) or how the breaking is frustrated (section 1.4). Next we discuss the mechanisms of making Rydberg atoms (section 1.5) and the potential application in the production of anti-hydrogen (section 1.6).

1.2 Rydberg Atoms

The Rydberg formula [1] describes the energy spectrum of Hydrogen:

$$E_n = -R\frac{1}{n^2} \tag{1.1}$$

with R the Rydberg constant and n the principal quantum number (an integer number). Rydberg (1854-1919); found that his formula also applies to other atoms when he replaced the principal quantum number with an effective principal quantum number: $n^* = n - \delta$, this δ is known as the quantum defect of the atom. For high n the energy levels of the non-hydrogenic atoms or molecules can be described by:

$$E_n = -R\frac{1}{n^{*2}} = -R\frac{1}{(n-\delta)^2}. \tag{1.2}$$

This quantized behavior of the energy spectrum made Bohr postulate the following notions (1913):

1: Electrons move in orbits restricted by the requirement that the angular momentum is an integral of $\frac{h}{2\pi}$ and furthermore the electrons in these orbits do not radiate in spite of their acceleration. They are in stationary states;

2: Electrons can make discontinuous transitions from one allowed orbit to another, and the change in energy, E_n-$E_{n'}$ will appear as radiation with a frequency: $\nu = \frac{E_n - E_{n'}}{h}$

so that Rydberg's observation could be explained. However, Bohr's theorem did not predict when the electrons make their transition between states. A quantum theory had to be developed to explain all the observed phenomena satisfactorily. In 1925 the

modern theory of quantum mechanics started with the work of Heisenberg, Born, Jordan, Schrödinger, and Dirac.

The dynamics of a Rydberg state is simple and is often sufficiently described in a classical manner. The size of a Rydberg state can be enormous and is given by the expectation value of the radial coordinate (with an angular momentum: $l = n-1$, atomic units are used unless stated otherwise):

$$\langle r \rangle = 2n^2. \tag{1.3}$$

An atom with a principle quantum number of $n = 200$ already has a radius of $\sim$4 μm. The roundtrip time of the electron in its orbit around the nucleus, is related to the energy spacing with respect to the neighboring n states and is given by:

$$T = 2\pi n^3. \tag{1.4}$$

For a $n = 200$ state this roundtrip time is in the nanosecond regime (1.3 ns). This is a convenient time scale since both lasers and electronical devices are available which produce pulses in the sub-nanosecond regime, in order to probe atomic dynamics. Notice the analogue with the third Kepler law: *the square of the period of a planet (T) in its orbit around the Sun divided by the cube of the semimajor axes (R) is constant:*

$$\frac{T^2}{R^3} = \text{constant} \tag{1.5}$$

and thus the orbit of the outer Rydberg electron is often referred to as a Kepler orbit around the nucleus.

The dynamics of these Rydberg states are highly susceptible to external electric fields, since the electric field of the Coulomb potential is strongly reduced at large distances from the core. In Fig. 1.1 the Coulomb potential is depicted (dotted line) and compared to the modified Coulomb potential. A saddle point is created at some distance from the nucleus. If the radius of the created Rydberg state extends to this saddle point the system will ionize and this process is called field ionization. The relation between the electric field needed to ionize an atomic state and the principal quantum number of that state is given by:

$$F = \frac{1}{16n^4} \tag{1.6}$$

and thus an electric field of $\sim$ 0.2 V/cm is required to field ionize a $n = 200$ Rydberg state.

Besides the modification of the Coulomb potential by the presence of an electric field, the energy levels are also perturbed. This is known as the Stark effect. In zero field, all the angular momentum states (quantum number: l) belonging to a state with a certain principal quantum number n are degenerate, due to the spherical symmetry. When a Rydberg atom finds itself in a external field this spherical symmetry is broken and l is

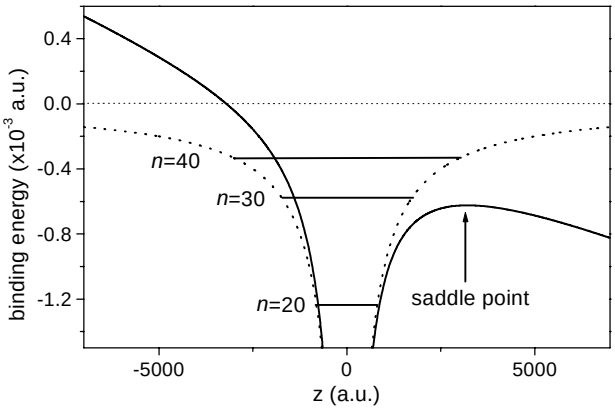

Figure 1.1: *Dotted line: field-free Coulomb potential along the z-axis:* $V = -\frac{1}{r}$. *The energy positions of three Rydberg states (with a principal quantum number of* $n = 20$, 30, *and* 40*) are depicted by a vertical line. Solid line: modified Coulomb potential by an external field of 500 V/cm along the z-axis:* $V = -\frac{1}{r} - Fz$.

no longer a good quantum number. The result is that the degenerate angular momentum states belonging to a certain n fan out with increasing field strength (Fig. 1.2) and crossings between states can occur. If the long-axis of the Rydberg orbit is oriented "uphill" in the modified Coulomb potential the binding energy of the Stark state is greater than the zero field binding energy. If the long-axis of the Rydberg orbit is oriented "downhill" in the modified Coulomb potential the binding energy is smaller than the zero field binding energy.

Rydberg atoms often show their dual nature in that they can be understood and described with both a semi-classical and a quantum mechanical model. This makes Rydberg atoms ideal for studying the onset of quantum mechanical effects. Sometimes the classical picture suffices, and sometimes a full quantum mechanical description is needed. A good example of this is the existence of two theories to describe atomic dynamics: 1) Multi Channel Quantum Defect theory [2] which is a successful quantum mechanical theory to describe atomic dynamics, and 2) Closed Orbit Theory, which is a semi-classical theory. Often, the Closed Orbit Theory predicts the overall atomic dynamics quite decently, and only the detailed dynamics require a quantum theory.

1.3 Ionization, Breaking of Rydberg Atoms

A Rydberg state can be made by exciting an atom from its electronic ground state to an excited state, by employing a laser which has a frequency (ν) matching the transition frequency of the ground state and the excited state ($E_n = h\nu$). Studies of these Rydberg states can be performed in the time domain or in the frequency domain. In the frequency

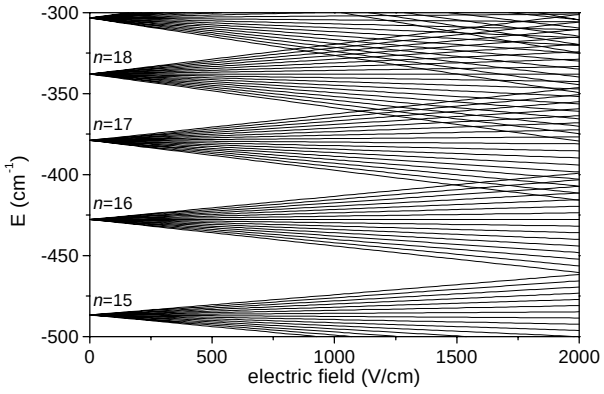

Figure 1.2: *Stark splitting of n-manifolds due to an external field.*

domain one would like to record the energy spectrum of the atom under study with high resolution. Preferably one does this with a laser which has a very narrow bandwidth. The atomic dynamics are retrieved from the energy levels. The spacing between levels is related to the roundtrip time of the excited electron and the width of the resonance is inversely proportional to the lifetime of the state. In the time domain one would like to excite the atom with a very short pulse. This creates a Rydberg electronic wavepacket that evolves along the Rydberg orbit in time.

There are two methods to detect the atomic dynamics of a Rydberg state. The first is that a bound Rydberg state can be probed by an electric field which increases in time so that the atom ionizes and an electron can be recorded (see Fig. 1.3a-b). This process is known as Pulsed Field Ionization [2]. The second is that a static electric field can be used. Laser-excitation can then create a quasi-bound Rydberg state, which due to the finite lifetime will ionize (see Fig. 1.3c-d). The time integrated electron flux or the time resolved electron emission can then be measured

In the second chapter of this thesis, the ionization behavior of Rydberg states due to time dependent electric fields is investigated. This is done by preparing a well defined Rydberg state of an atom and then slowly ramping the electric field. The relationship between the ionizing fieldstrength and the principal quantum number of Rydberg state is investigated for two different atoms: rubidium and lithium. In this manner we can deduce the effect of a non-hydrogenic core on the field ionization behavior, since the very light lithium atom (3 protons, and 4 neutrons) resembles much more a Hydrogen atom than a rubidium atom (37 protons, and 48 neutrons). In almost every experiment reported in this thesis, this relationship between the principal quantum number n of a Rydberg state and the electric field associated with it to ionize the state is used to determine the state distribution after performing an experiment.

The ionization of Rydberg atoms by half-cycle pulses closes the gap between ionization by (non-propagating) time dependent electric fields and ionization by electromagnetic radiation. A half-cycle pulse is characterized as half of a cycle of THz (10^{-12} Hz) radiation,

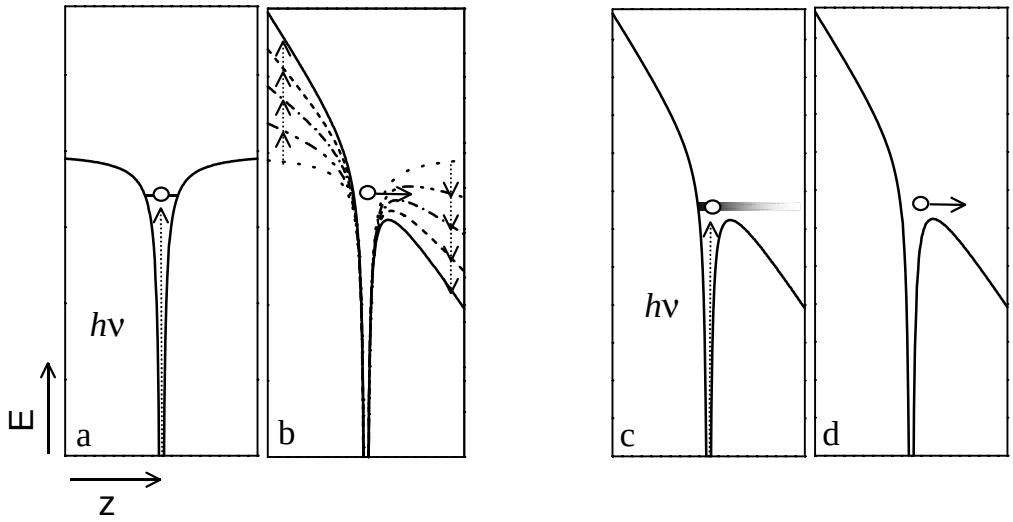

Figure 1.3: *Schematic representation of ways to detect the atomic dynamics of Rydberg atoms. a: laser excitation ($h\nu$) of a well defined Rydberg state in zero field. b: If an electric field is ramped in time, a saddle point is created which eventually will be deep enough to ionize the Rydberg state. c: Laser excitation ($h\nu$) of a well defined Rydberg state in an electric field above the saddle point. d: due to the finite lifetime of the Rydberg state, ionization will occur.*

or a unipolar electromagnetic wave of $\sim$ 0.5 ps duration. This description is not fully correct since Maxwell's equations demand that the time integral of the electric field in time is zero in free space. In fact the THz pulse consists of a very short half cycle pulse (duration: $\sim$ 0.5 ps), followed by a much slower half cycle ($\sim$ 10 ps) of opposite polarity and a much lower amplitude, so that the time integral of this mono-cycle is zero [3]. Jones *et al.* have studied half-cycle pulse ionization of Rydberg states with a principal quantum number of 15 - 35 [4] (roundtrip time: 0.5 - 6.5 ps) and demonstrated a new scaling law of n^{-2} for 10 % ionization. This is understood if one assumes that the first half-cycle acts as an impulsive kick ($\Delta\mathbf{p}$) which is shorter then the round trip time of the Rydberg electron and leads to an energy change (ΔE) of the Rydberg atom:

$$\Delta\mathbf{p} = -\int_{-\infty}^{\infty}\mathbf{F}(t)dt \text{ and } \Delta E = \frac{1}{2}\left[2p_0\cdot\Delta\mathbf{p} + (\Delta\mathbf{p})^2\right] \tag{1.7}$$

with p_0 the initial momentum of the Rydberg electron. Since the second, opposite half-cycle, is much slower it does not affect the ionization process of Rydberg states with principal quantum numbers of $\leq$ 35. In Chapter 3 the ionization behavior of Rydberg states with a principal quantum number of 60 - 180 is discussed. In this regime the roundtrip time of the Rydberg electrons is $30 - 1000$ ps and an effect of the second unipolar feature is observed for high n. The second unipolar feature is now also becoming impulsive on the atomic time scale and thus the Rydberg atom experiences two unipolar

kicks of opposite direction: a start and a stop pulse. This results in a displacement of the Rydberg atom, with hardly any energy change. Since there is hardly any energy gain or loss, ionization is suppressed.

Finally in Chapter 4, the ionization dynamics of a doubly excited state is investigated. A doubly excited state is a state in which both electrons of a two valence atom are promoted to Rydberg states. An investigation in the time- and frequency domain [5–7] of such a doubly excited state in an electric field is presented, with the aid of narrow- and broadband optical laser pulses. The atomic system has the classical analogue with two coupled oscillators, where one oscillator can transfer energy to the other. Ionization can occur when two electrons within the same atom are excited and have a certain coupling with each other. Each time they meet, energy transfer can occur. If the combined energy is larger than the binding energy of one of these electrons, there is the possibility that after an encounter ionization occurs. This process is known as autoionization.

1.4 Frustrated Breaking

An electric field will not always have a destructive effect on Rydberg atoms. In hydrogen, Stark states are completely uncoupled, but for non-hydrogenic atoms there exists a coupling between these states. If one populates one certain state in a static electric field and then varies the field in time so that this state crosses another state, one can transfer population from the initial state to another diabatically due to the non-zero coupling.

In Chapter 5 an experiment is discussed which shows that population transfer by time dependent electric fields can have a stabilizing effect against ionization. In the experiment a slow (compared to the atomic dynamics) electric field kick (a unipolar pulse) is used to transfer part of an ionizing state to a non-ionizing one (see Fig. 1.4). Due to this time dependent electric field, a state which was initially above the saddle point in the Coulomb potential ($F = \frac{1}{16n^4}$), can be coupled with states below the field induced saddle point, resulting in frustrated ionization. Not all the observed effects can be described by the Landau-Zener theory and a model is presented which incorporates interference effects between the Stark states by the time varying field, revealing quantum mechanical behavior.

1.5 Recombination, Making of Rydberg Atoms

Recombination is the time inverse of ionization. Due to this relationship, the process which is easier to realize is more often studied. In most cases ionization is more convenient to study. An example of this is dielectronic recombination, which is the time inverse of autoionization. In dielectronic recombination a free electron and ion are recombined via an intermediate step, where a doubly excited state of an atom is created. If one of the electrons then radiative decays to a more deeply bound state, the total energy can become less then zero, so that a bound state of an atom is created. Detailed

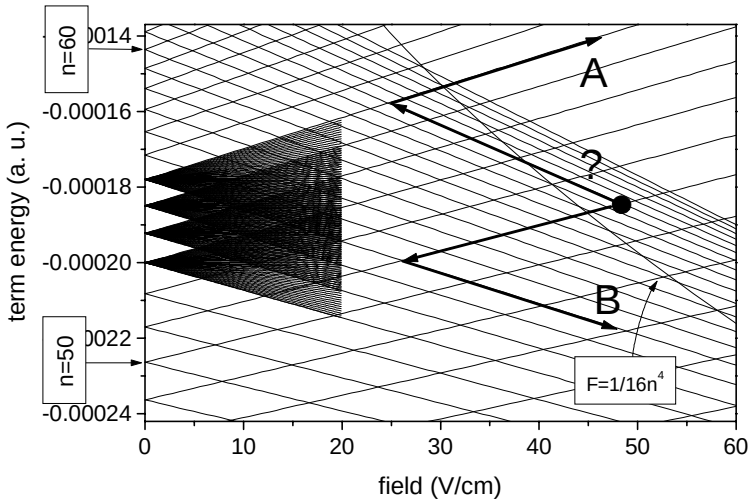

Figure 1.4: *Frustrated ionization. A unipolar field pulse induces Landau-Zener transitions between Stark states so that part of an initially ionizing Stark state can be transferred into stable states below the classical ionization limit ($F = \frac{1}{16n^4}$, route B). A competition is present between transfer to more highly excited states (route A) and more deeply bound ones (route B).*

studies of autoionization processes resulted in a thorough understanding of dielectronic recombination.

There are several ways that a bound state of an electron and an ion can be made out of a free electron and an ion. All of these schemes have in common that excess energy has to be taken away in some manner when a bound state is formed. This can be done by the emittance of a photon, or by a third spectating particle. In general: a third body is required to conserve energy.

The study of recombination began more than a century ago when in 1895 Röntgen (1845-1923) discovered X-rays [8]. Thomson and Rutherford then proved that the conductivity of a gas after exposing it to X-rays arises from the presence of ions, and suggested that the decay in conductivity is due to recombination. After several refinements of this theory, Kramers launched his theory of electron radiative recombination (1923) where an ion and an electron recombine into a bound state under the emission of a photon, to explain the observed decay:

$$A^+ + e^- \rightarrow A(n) + h\nu. \tag{1.8}$$

Notice that the time inverse of this process is photo-ionization. Radiative Recombination is a non-resonant process with a diverging cross section at zero center-of-mass energy which continuously decreases towards higher center-of-mass energies [9, 10]. The recombination rate per ion in an electron plasma with a density of $n_e = 10^6 - 10^7$ cm^{-3}, and a thermal

energy of 4.2 K, is given by the following equation [11]:

$$\Gamma_{rr} = 3 \times 10^{-11}(4.2/T)n_e s^{-1} \tag{1.9}$$

this results in 10^{-4} recombinations per second, per ion.

Research on the earth's ionosphere then showed that the rate for this recombination process alone is too low to account neutralization of the oxygen ion. Massey and Bates suggested in 1942 a new recombination mechanism, termed: dielectronic recombination [12]. In this mechanism recombination takes place through an intermediate doubly excited state of the oxygen atom which then decays to a stable state:

$$O^+(2p^3\ ^4S) + e^- \rightleftarrows O(2p^3\ ^2D\ 3p\ ^3F) \rightarrow O(2p^3\ ^2D\ 3s\ ^3D) + h\nu. \tag{1.10}$$

The time inverse of this process is called autoionization [2] and is the topic of Chapter 4.

The Radiative Recombination rate (Γ_{rr}) can be enhanced by stimulated transitions in an external light field, the rate (Γ_{srr}) is then increased from Γ_{rr} to $(1+G)\Gamma_{rr}$. The trade-off is that the same light field can also ionize the recombined atoms again and thus the Gain (G) is limited. Studies of (Stimulated) Radiative Recombination can be found in ref. [13, 15–18], a detailed description of Stimulated Radiative Recombination can be found in [14].

Not necessarily does the recombination process have to be governed by emitting photons. Already in 1932 Darrow [19] postulated that recombination could also occur in a three body process [11, 20]:

$$A^+ + e^- + e^- \rightarrow A(n) + e^- \tag{1.11}$$

where the excess energy of the formation of a bound state is taken away by a second electron. The time inverse of this process is electron impact ionization [2]. In fact at high ion and electron (n_e) densities and low temperatures (T) the rate (Γ_{tbr}) per ion of this process can be significant [11, 23–25]:

$$\Gamma_{tbr} = 6 \times 10^{-12}(4.2/T)^{9/2} n_e^2\ \mathrm{s}^{-1}. \tag{1.12}$$

A rate of 10^2 recombinations per second is expected to occur for ions in an electron plasma with a density of $10^6 - 10^7$ at 4.2 K. Notice that the rate decreases very rapidly for higher temperatures ($n_e = 10^6 - 10^7$ and $T = 42\ K$ results in: $\Gamma_{tbr} = 10^{-3}\ s^{-1}$).

In this thesis a novel, controllable and efficient recombination scheme is discussed: Pulsed Field Recombination (PFR). The scheme is based on the usage of time dependent electric fields to create bound states out of free electrons and ions. One can say that the effect of the third body, stimulating the recombination through its time dependent electric field, is now applied 'by hand' in the form of tailored pulses. In Fig. 1.5 the mechanism of this recombination scheme is sketched. Notice that the time inverse of this novel recombination scheme is Pulsed Field Ionization (Chapter 2).

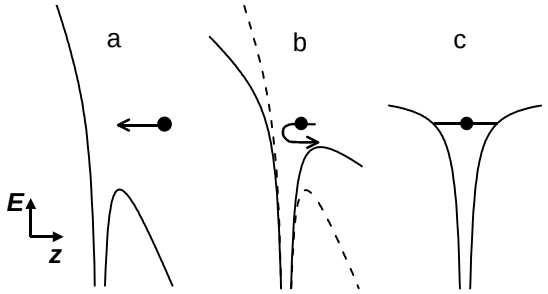

Figure 1.5: *Sketch of the PFR scheme. Suppose an electron is approaching a proton in the presence of an electric field (a), such that the electron just passes over the saddle point of the barrier (b). Eventually the electron will leave the potential over the same barrier. The electron spends about 1 nanosecond at the turning point near the proton. The key point of the proposed recombination scheme is to reduce the static field while the electron is near the proton. In this way the electron ends up below the saddle point in a Rydberg state and can not escape again (c).*

Photo-ionization studies revealed that the ionization probability of a Rydberg atom is dependent on the frequency of the ionizing light. In the regime where just one photon is required to ionize a Rydberg state, lower frequencies of the ionizing light are more efficient. Since the time inverse of ionization is recombination, it can be understood that the same holds for (stimulated) radiative recombination. Therefore, it makes sense to construct a recombination scheme in the low frequency limit. For electro-magnetic radiation this limit is the microwave regime (1 GHz$-$1 THz). Realizing that a photon field is associated with a time-varying electric field, it is not surprising that a slow (beyond the microwave regime) time varying electric field can be employed to realize an efficient recombination scheme.

In Chapter 6 the first realization of the Pulsed Field Recombination scheme is described with Rb ions and free electrons. Chapter 7 reports on the production of Rydberg carbon clusters with Pulsed Field Recombination, showing that Pulsed Field Recombination can be used to produce a Rydberg state in any kind of atom or molecule. In Chapter 8 Pulsed Field Recombination is discussed in a configuration resembling the experimental conditions in which one would like to produce anti-hydrogen. Also a more thorough discussion is presented on the dynamics involving Pulsed Field Recombination. Finally in Chapter 9 a progress report is presented of the realization of Pulsed Field Recombination with anti-protons and positrons at the ATRAP experiment at CERN to produce cold anti-hydrogen: the bound state of a positron and an anti-proton.

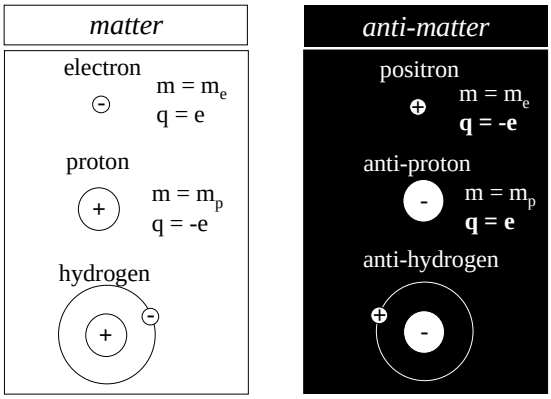

Figure 1.6: *Matter versus anti-matter.*

1.6 Anti-Matter

For every elementary particle there exist an anti-particle with opposite charge, magnetic moment and other internal quantum numbers (e.g. lepton number, baryon number, strangeness, charm, etc.), but the same mass, spin and lifetime (see Fig. 1.6). When an anti-particle collides with its matter counterparticle, they annihilate, and all the mass is converted into energy: $E = mc^2$. Dirac predicted the existence of anti-matter in 1928 when he formulated his version of quantum mechanics.

After the theoretical prediction of anti-matter, the anti-electron was observed in 1931 by Anderson [21, 22] and was named: the positron. It took a longer time to observe the more heavy anti-matter particles since more energy is required to produce these particles. With the advent of accelerator rings enough energy could be made to produce and observe anti-protons in the nineteenfifties. From this moment on, all the ingredients are available to make an anti-atom: anti-hydrogen. Still it took until 1996 to observe the first anti-hydrogen atoms.

In 1996 Baur *et al.* [26] observed 9 statistically significant events of the formation of anti-hydrogen. These anti-atoms were produced with relativistic energies and therefore it was impossible to study these anti-atoms in detail. The production of cold anti-hydrogen will enable the study of the properties of neutral anti-matter. For instance, the direct comparison of the anti-hydrogen energy spectrum with that of hydrogen can be a test of the CPT theorem. The CPT theorem states that every physical process is invariant under the combined operation of Charge conjugation (C), Parity inversion (P), and Time reversal (T). Measuring an identical energy spectrum of anti-hydrogen compared to hydrogen will support the CPT theorem. In fact this comparison can be done with great precision: recently Niering *et al.* [27] reported on an absolute frequency measurement of the hydrogen 1S-2S two-photon transition in a cold atomic beam with an accuracy of 1.8 parts in 10^{14}. Performing the same experiment with a cold atomic anti-hydrogen beam would be the most stringent CPT comparison of neutral matter with neutral anti-matter.

One can also think of gravity experiments of neutral anti-matter. Einstein's equivalence principle states that the influence of gravity on a particle and its complementary anti-particle is exactly the same. Some Quantum Field theories predict that the sign of the gravitational acceleration is the same but the magnitude is different. So far no conclusive measurement has been performed to determine the sign or magnitude of the gravitational acceleration on anti-matter since charged particles are much more susceptible to electric fields then to the gravitational field. For instance, the gravitational force on an anti-proton is already compensated by an electric field of 10^{-9} V/cm, and thus the smallest stray field in an experimental apparatus already disables an accurate measurement. Neutral anti-matter would be a much more accurate testing ground for this theory since it is not susceptible to external (electric) fields. However a precise measurement of the gravitational acceleration of anti-matter requires cold anti-matter since the potential energy difference when an anti-hydrogen atom is translated over one meter is extremely small: $\Delta E_{pot} = mgh \approx 10^{-7}$ eV ≈ 1 mK. If the anti-hydrogen atom has a kinetic energy greater then 1 mK the gravitational movement can be completely compensated, it is therefore necessary to cool the anti-hydrogen atoms below 1 mK, with for instance laser cooling.

Finally in Chapter 9 a first attempt is described of the creation of anti-hydrogen by Pulsed Field Recombination. The experiment is performed at CERN for the ATRAP [28] collaboration, where recombination is studied of trapped positrons and anti-protons. These charged anti-matter species are trapped in Penning traps. A Penning trap employs the combination of electric and magnetic fields to trap a charged particle. It is expected that Rydberg anti-hydrogen should be formed, by Pulsed Field Recombination, in the current configuration with a temperature of at least 4 K. It appeared that the strong magnetic field (6 T) frustrates the formation of Rydberg anti-hydrogen.

Chapter 2

Selective Field Ionization

We present a direct comparison between calculated and measured ionization in Li and Rb when an initially bound Rydberg electron is stripped from the atom by ramping an electric field [0.350 V/(cm ns)]. We describe the method used to calculate the field dependence of the ionization. The essential feature of the method is the repeated application of the Landau-Zener approximation for all of the level crossings as the field is ramped. We also give a description of the dynamics of Li and Rb in the ramping field. We observe that the Li selective field ionization is sensitive to the Stark levels within an n-manifold, while for Rb only an n-dependence is observed.

2.1 Bound State Characterization

In the experiments discussed in this thesis, the technique of Selective Field Ionization (SFI) will be used as an experimental tool to determine the state distribution of a Rydberg atom. In Chapters 6-9 the time inverse of SFI will be employed as a novel and efficient scheme to recombine a free electron and an ion: Pulsed Field Recombination (PFR). In this chapter a detailed experimental and theoretical study is presented on the SFI mechanism. In SFI, the Rydberg atom is subjected to an electric field that ramps to higher strengths over times that are very long compared to the classical period of the electron. Eventually the field strength is large enough to rip the electron from the atom. Often, the field at which the electron is removed from the atom is when the energy of the state is greater than the classical ionization threshold, in atomic units $E = -2\sqrt{F}$ or equivalently $F = 1/16n^4$ (Eq. (1.6)); in other units, this relationship is often expressed as $E(\mathrm{cm}^{-1}) = 6.12\sqrt{F(\mathrm{V/cm})}$. We will discuss an interesting violation of this rule below. The signal is the electron current versus field strength (or time); see Refs. [29–35] for early discussions of the process. The technique has been used to characterize the Rydberg population in many different situations: from the collision of slow ions with Rydberg atoms [36] to the ZEKE [37] states used to measure the ro-vibrational thresholds of complicated molecules [38]. A feature of this method is that a given initial state will produce an electron current with a well defined distribution in field strength that depends on the ramp rate of the electric field. Due to the long time scales of the ramp (typically 1

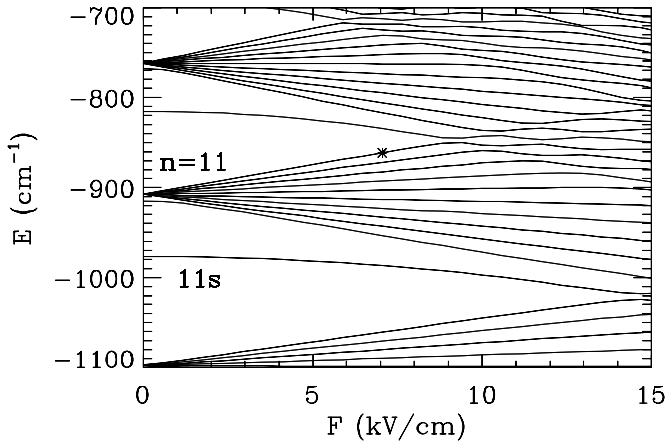

Figure 2.1: *Energy levels of $m = 0$ states of Li as a function of static electric field strength. These are energies around the $n = 11$ manifold. Asterisk: see text. The notation 11s denotes a Rydberg state with a principal quantum number of 11 and an angular momentum of 0.*

μs) compared to atomic times, no information about relative phases of the excited states is obtained; for example, if the atom is in a wave packet of two states, the SFI signal will be the incoherent sum of the currents from the two states.

This experimental technique is widely used to characterize the population of highly excited states in an atom, but the quantitative, theoretical description of the method does not exist. In some cases, the lack of a theory has not impeded the use of SFI since all aspects could be investigated experimentally. One obtains the field distributions for specific initial states experimentally by exciting the states with a narrow bandwidth pulsed laser and then ramping the electric field; afterwards, unknown excited state populations can be characterized by comparing the resulting field distribution with the previously measured distributions from specific initial states. This method is called Pulsed Field Ionization [35] (PFI), when the integrated electron flux due to a field ramp is measured, and is used when only the amount of bound state population needs to be determined. There are cases where the lack of a theoretical method for calculating an SFI signal has prevented the direct comparison between theory and experiment; often, the relevant states can not be easily excited by a narrow bandwidth pulsed laser. The purpose of this paper is to present a method for calculating the SFI signal for a simple atom and to test the method through a quantitative comparison with measured SFI spectra.

In Fig. 2.1 we plot the energy levels of Li versus the strength of a static electric field for a simple region near $n = 11$ states. The field strength range is chosen to show how the levels from adjacent n-manifolds start to cross as the field strength increases. Suppose that all of the population is in the highest energy state of the $n = 11$ manifold which is marked by an asterisk in Fig. 2.1. All of the population will remain in this state until the field is ramped to ~ 9 kV/cm where the lowest state from the $n = 12$ manifold crosses it. The

population can be split amongst different states at each field strength where levels nearly cross. The amount of population that is on each level can be approximated by a formula from Landau and Zener. For Selective Field Ionization, the population continues through many avoided crossings until reaching a level that is strongly coupled to the continuum at which point it leaves the atom. The size of the avoided crossings is crucial for the SFI behavior. The average energy splitting at a crossing is roughly proportional to the sum of the differences of the quantum defects from integers. We have studied two extreme cases in alkali atoms: Li with quantum defects (μ_l) of $\mu_0 = 0.4$, $\mu_1 = 0.05$, and $\mu_2 = 0.002$ and Rb with quantum defects of $\mu_0 = 3.14$, $\mu_1 = 2.64$, $\mu_2 = 1.35$, and $\mu_3 = 0.02$ (only the non-integer parts of the quantum defects are important, giving $\bar{\mu}_0 = 0.14$, $\bar{\mu}_1 = -0.36$, $\bar{\mu}_2 = 0.35$, and $\bar{\mu}_3 = 0.02$).

There has been little theoretical work investigating the idea of selective field ionization. In Refs. [39, 40], a model of the crossing of many levels of two adjacent n-manifolds was explored; in both papers, all of the crossings were treated within the Landau-Zener approximation with the difference that the phase accumulation on different paths [41] was neglected in Ref. [39] but incorporated in Ref. [40]. These papers are essentially exploring the first step of SFI where the levels of the n-manifold start crossing the levels of the $n \pm 1$ manifolds.

Simple estimates show why there has been little theoretical work on this system. If one attempts to perform a brute force numerical integration of Schrödinger's equation, several difficulties soon become apparent. The first is that the electron leaves the atom, so it is necessary to use a method that will effectively let the electron escape without reflection from unphysical boundaries (either in position space or in basis set space). Once this difficulty is overcome, there is the much more problematic aspect that is related to the relative slowness of the electric field ramp. For states near $n = 50$, the field free period is roughly 20 ps which is a factor of 50,000 smaller than the ramping time which is measured in μs. Thus, a prohibitively large number of time steps in the numerical integration prevents a direct solution of Schrödinger's equation. Here we have explored an approximation scheme for the calculation of the field distribution of ejected electron current.

The method we have developed was inspired by the treatment in Refs. [39,40] and extends these ideas into a form that can be used to calculate the field distribution. The basic idea is to follow the population through a series of level crossings using the Landau-Zener approximation to obtain the population of each level after a crossing. As in Ref. [39], we ignore the phase accumulation in each path; thus, we follow populations instead of amplitudes. This is a very good approximation for SFI since there are a very large number of paths that lead to ionization at field, F, with nearly randomly varying phases on the different paths; the differing phases essentially guarantees that the interference between different paths will average to zero. In the model of Ref. [40], the phases needed to be retained because all of the phase differences were integer multiples of a basic phase difference; this property does not correspond to the actual SFI. Physically our approximation should make sense because the field distribution of when the electron is stripped from the atom is insensitive to the macroscopically small, but on an atomic level huge, variations

in ramp rate that are present in every experiment. The innovation of this paper is to give a method for obtaining all of the information that is needed for all of the Landau-Zener crossings up to the point the electron leaves the atom.

As a test of the theory, we compared calculated and measured field distributions from states near $n = 55$ in Li and Rb. We chose these two atoms to illustrate the different type of SFI spectra that result when the coupling between levels is small (Li) or large (Rb). We excited Li from the $2p_{3/2}$ excited state by a one photon transition at a specific wavelength with a pulsed, narrow-band dye laser ($\Delta E < 0.2$ cm^{-1}). The initial $2p_{3/2}$ was excited by a narrow-band pulsed dye laser ($\Delta E < 0.2$ cm^{-1}) laser from the ground state (2s) with the polarization perpendicular to the electric field. We varied the wavelength and polarization of the laser that excites the atom from the initial state to the Rydberg states in order to access different Rydberg states. In both experiments, laser power was kept low to avoid AC-Stark shifting of the Rydberg states. The wavelength range was chosen to excite states in zero field n manifolds from $n = 52$ to 55. We also performed the SFI measurements and calculations when the excitation was performed in a static electric field between 0 and 40 V/cm. Next we performed experiments and calculations in Rb under similar conditions; we excited the Rb atoms from the ground state in a non-resonant two photon process with a narrow-band dye laser $\Delta E < 0.2$ cm^{-1}. These variations allowed us to test the theory in many different situations.

2.2 Theoretical Method

We first describe the simple theory for SFI when the electron is in a pure Coulomb potential giving a total potential $(-1/r) + Fz$. The Hamiltonian separates in parabolic coordinates ($\xi = r+z$ and $\eta = r-z$) for a static, homogeneous electric field plus Coulomb potential. For the slow ramp rates that are used in SFI, the wave function diabatically evolves so that a state that has n_1 nodes in the up-potential coordinate (ξ) will continue with n_1 nodes. The behavior of the wave function in the down-potential direction is slightly more complicated. For zero field, the wave function has n_2 nodes in the down-potential coordinate, η. Once an electric field is turned on, all states become continuum states and have an infinite number of nodes in the down-potential direction. This appears to create ambiguities for the definition of the state. However, we can retain conceptual and physical simplicity by noting that the electron starts in the region near the atom and the time to tunnel through the potential barrier is very long on experimental time scales unless the electron has an energy near the top of the barrier. Thus, we will define n_2 to be the number of nodes in the down-potential coordinate, η, in the region between the nucleus and the maximum of the potential. For the slow ramp rates in SFI experiments, n_2 does not change with increasing field. The only parameters that change are the energy and the tunneling rate for a given n_1, n_2. From these ideas, we find that

$$\dot{P}_{n_1 n_2} = -\Gamma_{n_1 n_2}[F(t)] P_{n_1 n_2} \tag{2.1}$$

where $P_{n_1 n_2}$ is the population in the n_1, n_2 state and $\Gamma_{n_1 n_2}[F(t)]$ is the tunneling decay rate which depends on the field strength F at time t. Two general trends to remember:

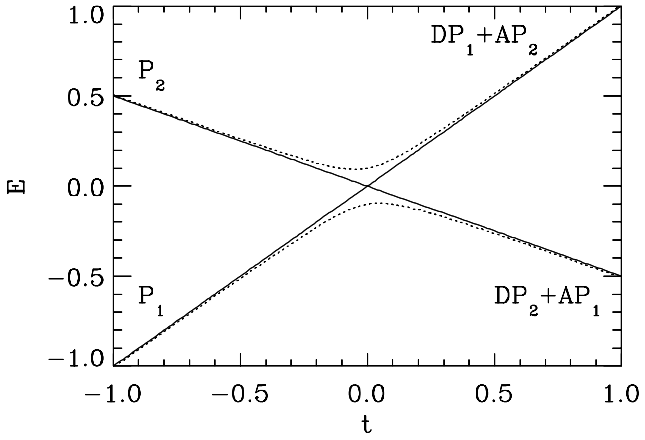

Figure 2.2: *Schematic drawing of two levels crossing. The solid lines neglect the interaction between the levels and the dotted lines give the adiabatic energies. Both the time and energy are in arbitrary units.* P_1 *and* P_2 *are the original populations.* D *is the probability to evolve diabatically through the crossing and* $A = 1 - D$ *is the probability to evolve adiabatically through the crossing.*

states with $n_1 < n_2$ ($n_1 > n_2$) decrease (increase) in energy with increasing field strength and states with the same $n_1 + n_2$ decay faster by tunneling as n_2 increases. The tunneling rates are calculated numerically using a WKB approximation [42]; see Refs. [43, 44] for discussions of analytic and semi-classical calculations of the tunneling decay.

Our method for calculating the SFI distribution for non-hydrogenic atoms generalizes the simple theory for H in two respects. The first generalization is that the non-Coulombic potential causes couplings between the different n_1, n_2 states; the possibility for population to change quantum numbers when energy levels cross is included through the Landau-Zener approximation. The second generalization is that once the energy of a state is larger than the classical ionization threshold, $-2\sqrt{F}$, it is energetically allowed to escape the atom without tunneling *if* states in closed n_1 channels couple to open channels. This coupling is again mediated through the non-Coulombic potential near the nucleus.

We first describe the generalization due to level crossings. We think of all of the levels as crossing diabatically for the purpose of indexing the states. This is only a book-keeping device and does not reflect any choice about the description of the physics. In Fig. 2.2 we give a schematic drawing of a two level crossing and the parameters that characterize the populations before and after the crossing. We define P_1 and P_2 to be the populations in states 1 and 2 (respectively) before the crossing and $\bar{P}_1$ and $\bar{P}_2$ to be the populations after the crossing. We will use A to be the probability that state 1 evolves adiabatically into state 2 after the crossing and D to be the probability that state 1 evolves diabatically into state 1 after the crossing; by symmetry, the probability for 2 to evolve into 1 is A and for 2 to evolve into 2 is $D = 1 - A$. The conservation of probability demands that

$A + D = 1$. Thus after the crossing the populations are

$$\bar{P}_1 = D \cdot P_1 + A \cdot P_2 \quad \text{and} \quad \bar{P}_2 = A \cdot P_1 + D \cdot P_2. \tag{2.2}$$

The only difficulty is in calculating A or D and the field dependence of the energies of all the states.

The first step is in obtaining the adiabatic or diabatic transition probabilities in terms of general parameters. Using the Landau-Zener approximation, gives the diabatic probability, D as

$$D = \exp(-2\pi |V_{12}|^2 / \left| \frac{dE_1}{dt} - \frac{dE_2}{dt} \right|) \tag{2.3}$$

with all parameters evaluated at the crossing; atomic units are used in this equation and throughout the paper unless stated otherwise.

The derivative of the energy with respect to time can be recast as $dE/dt = \dot{F} dE/dF$ where $\dot{F}$ is the ramp rate for the electric field and dE/dF is the derivative of the energy with respect to the field strength. In the calculations, we used the experimental ramp rate of $\dot{F} = 415$ V/(cm$\cdot \mu$s). The energies are calculated using a WKB approximation [42] by first quantizing the motion in the up-potential coordinate, ξ, to obtain the separation parameter β_1 and then forcing the phase accumulated between the nucleus and the maximum of the potential to be $(n_2 + 1/2)\pi$ in the down-potential coordinate, η. The position of the crossings and the dE/dF are obtained numerically from the WKB quantized energy levels. Note that all crossings can be made more diabatic by simply increasing $\dot{F}$ which is an experimentally controllable parameter.

The coupling matrix elements, V_{12}, can be calculated by using the quantum defects of the zero field energy levels. First we define a reduced quantum defect $\bar{\mu}_l = \mu_l + j$ where j is an integer such that $-0.5 < \bar{\mu}_l < 0.5$. The effect of the non-Coulombic potential is to shift the energy of the state with energy $-1/2n^2$ by an amount $-\bar{\mu}_l/n^3$; this gives the expectation value of the non-Coulombic potential for energy normalized Coulomb waves as

$$\int f_l^2(r) V(r) dr = -\bar{\mu}_l. \tag{2.4}$$

The coupling between energy normalized waves in parabolic coordinates uses the transformation coefficients between the functions in spherical coordinates and parabolic coordinates to give: $\bar{V}_{\beta\beta'} = -\sum_l U^0_{\beta l} U^0_{\beta' l} \bar{\mu}_l$; the U^0 are given by Eqs. (17,21,62) in [42]. The last remaining task is to convert the functions that are normalized per unit energy to functions that are normalized per unit volume. This is not completely obvious because there are no bound states in the field; as in the definition of the number of nodes in the ξ direction, we only use the part of space from the nucleus to the maximum of the potential in the ξ direction.

With these restrictions, the factor to convert from energy normalization to space normalization is obtained from the energy derivative of the WKB phase between the first two classical turning points in ξ. The conversion factor is $N_\beta^2 = \pi (d\Delta/dE)^{-1}$ given in

Eq. (A3) of [42]; the subscript β indicates the value of the separation constant for the wave function in parabolic coordinates. With these factors, the coupling between two states defined by the separation parameters β and β' is

$$V_{\beta\beta'} = -N_\beta N_{\beta'} \sum_l U^0_{\beta l} U^0_{\beta' l} \bar{\mu}_l. \tag{2.5}$$

There is an interesting point of physics that arises from scaling arguments. The rate of change of E depends on the dipole moment which is proportional to n^2; the coupling matrix element is proportional to $1/n^4$. Thus, the evolution of states rapidly becomes diabatic as n increases. This was seen in the experiments of Ref. [33].

The other generalization that needs to be incorporated is the coupling between the "closed" channels, β_c, where the electron needs to tunnel to escape and "open" channels, β_o, where the electron can classically leave the atom. The reason for these two types of channels at the same energy is that the electron can partition its available energy between two different degrees of freedom, ξ and η. For $E > -2\sqrt{F}$, the electron can classically leave the atom if the energy is partitioned such that a large enough fraction is in the down-potential, η, direction. If too much is in the up-potential, ξ, direction, the electron will have to tunnel to escape. For hydrogen, the energy and motion in the two different directions are uncoupled and thus the electron *must* tunnel if it is in a closed channel. For all other atoms, the motion in the two different directions are coupled through the non-Coulombic potential from the core electrons and thus the electron can scatter from a closed to an open channel and leave without tunneling.

The possibility of scattering and leaving the atom adds to the decay rate of the state. Using time dependent perturbation theory, the decay rate to go from a closed channel to an open channel is $\Gamma = 2\pi|V_{oc}|^2$ where the open channel function is normalized per unit energy and the closed channel is space normalized. We can use the coupling matrices from above but now only space normalize the closed function to obtain an additional decay rate:

$$\Gamma_c = 2\pi N^2_{\beta_c} \sum_{\beta_o} \left| \sum_l U^0_{\beta_c l} U^0_{\beta_o l} \bar{\mu}_l \right|^2 \tag{2.6}$$

where the sum over all open channels, β_o, is necessary to get the total decay rate.

These are all of the pieces necessary to calculate when the electron is stripped from the atom. To summarize: (1) at each time step, there is a check to see if two levels cross each other; if there is a crossing the populations are redistributed using the Landau-Zener approximation, and (2) a decrease in population can occur by tunneling or by scattering from a closed channel into an open channel; the two decay rates are added incoherently due to the different quantum numbers in the final channels. These steps are repeated until the population on the atom decreases to less than 1% of the original population. The calculations presented in this paper used field steps of 0.2 V/cm; the $m = 0$ results for Li were obtained with less than 100 steps for a total of $\sim 2 \times 10^4$ crossings while the $m = 2$ results were obtained with roughly 1000 steps for a total of $\sim 5 \times 10^4$ crossings. The SFI signal is minus the time derivative of the total population.

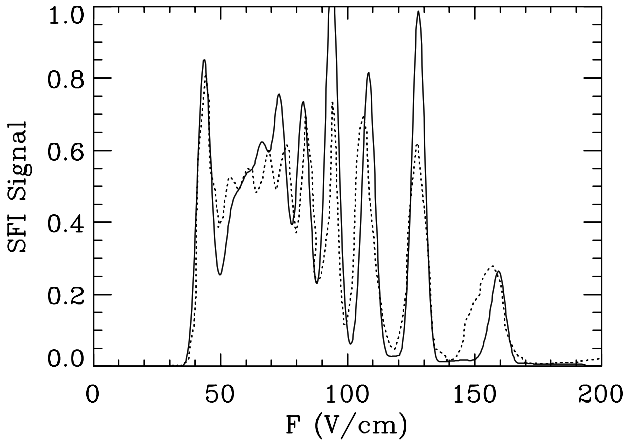

Figure 2.3: *A comparison between the calculated (solid line) and measured (dotted line) SFI signal for Li excited from the $2p_{3/2}$ state with an energy 39.25 cm^{-1} below the zero field threshold and polarization perpendicular to the electric field. The atom is originally in a static field of 35 V/cm before the field is ramped. The signal is given in arbitrary units.*

2.3 Matching Experiment with Theory

To gauge the effectiveness of this method, we present a comparison between calculated and measured SFI distributions in Li and Rb. In Fig. 2.3, the measured and calculated SFI spectrum for Li is presented for the case when the second laser excites the atom to an energy of 39.25 cm^{-1} below the zero field ionization threshold, is polarized perpendicular to the field axis, and the atom is in a 35 V/cm static field at the excitation; this is a typical level of agreement that was achieved between the calculation and experiment. It is clear that all of the features are accurately reproduced and the approximations work well for this atom. The SFI spectrum is a superposition of the spectra from 3 different final m symmetries: $m = 0, 1, 2$. In Fig. 2.4, we present the calculated SFI signal from Fig. 2.3 but separated into m-components (solid line is $m = 0$, dotted line is $m = 1$, and dashed line is $m = 2$).

We present a contour plot of the calculated SFI signal versus energy and ramp field for excitation by a photon parallel to the field in Fig. 2.5 and perpendicular to the field in Fig. 2.6. In both figures, the excitation was performed in a 35 V/cm static field. These figures show some of the general trends that we observed in the SFI spectra.

There are a number of interesting features of Figs. 2.3-2.6 that can be understood at a qualitative level. One important feature is that the excitation laser has a bandwidth of roughly 0.15 cm^{-1}. Thus, there are roughly 5-10 Stark states of each m-component that are initially populated. For fields of $\sim$ 35 V/cm, the different states that are excited belong to different n-manifolds and have substantially different dipole moments; thus, the variation in the division of energy between the two parabolic coordinates is much more

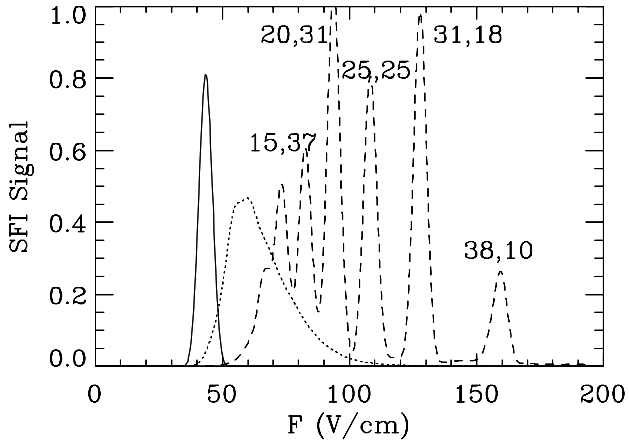

Figure 2.4: *A separation of the different m-components of the calculated SFI signal from Fig. 2.3: solid line ($m = 0$), dotted line ($m = 1$), and dashed line ($m = 2$). All m-components have the same initial central energy and width. Note that the signal for $m = 2$ distinguishes the separation of energy between the up- and down-potential directions. The peaks in the $m = 2$ spectrum can be classified using the number of nodes, n_1, in the up-potential coordinate and the number of nodes, n_2, in the down potential coordinate with the notation (n_1, n_2, n) where $n = n_1 + n_2 + |m| + 1$; another notation that is sometimes used is the quantum number $k = n_2 - n_1$. We have labelled the last 5 peaks associated with the $m = 2$ states using n_1, n_2 notation. Starting from the peak at 160 V/cm to the early peaks at 70 V/cm, the states are (38,10,51), (31,18,52), (25,25,53), (20,31,54), (15,37,55), (11,42,56) and (7,47,57). The last two states are stripped first and overlap each other near 70 V/cm. At the initial field strength of 35 V/cm, all of these states are within 0.2 cm^{-1} of each other.*

substantial than the variation of total energy of the different states.

Another important feature determining the Li SFI spectra is the large difference in quantum defects for the low-l partial waves. The quantum defects are $\mu_0 = 0.4$, $\mu_1 = 0.05$ and $\mu_2 = 0.002$. The differences in quantum defects give quite different behaviors for the different m-states in the SFI experiment. The results for a final polarization parallel to the electric field only gives final states of $m = 0$ and $m = 1$ character for the spatial part of the wave function since the initial state has $m = 0$ and $m = 1$ spatial components. We observed somewhat different SFI spectra when we used the $2p_{1/2}$ excited state as the initial state. This is because the composition of the final m-states changes due to the different m-components of the orbital angular momentum in the $2p_{1/2}$.

These considerations are very important because the different m-states behave quite differently in the SFI ramping. The coupling matrix elements only depend on the quantum defect of states with $l \geq m$; thus, $m = 0$ states can couple through $l = 0, 1, 2$ scattering but $m = 2$ states can only couple through $l = 2$ scattering. The $m = 0$ states go through almost every crossing adiabatically; the large $l = 0$ quantum defect provides

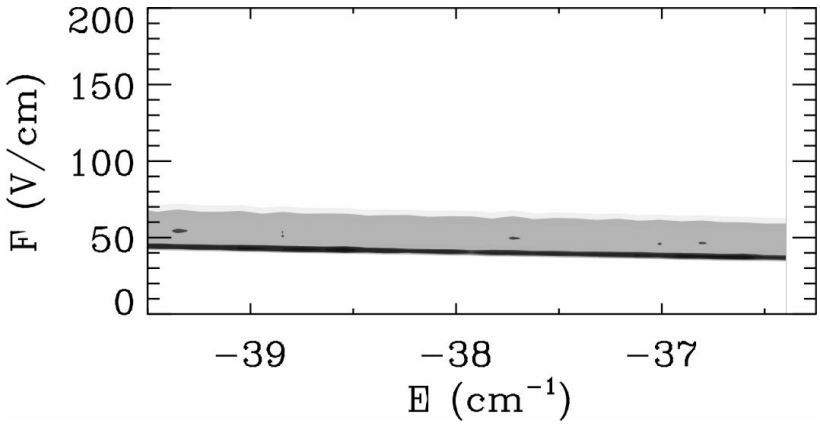

Figure 2.5: *Intensity map of the calculated SFI signal for Li excited from the $2p_{3/2}$ state with a polarization parallel to the electric field. The atom is originally in a static field of 35 V/cm before the field is ramped.*

strong coupling between the different states because these are the states that suffer most from core scattering. As a result, the population tends to stay on a few levels that are closely grouped in energy. This means that soon after a state has an energy above the classical ionization threshold, $-2\sqrt{F}$, it will scatter into open channels and decay rapidly. Thus, the $m = 0$ states are in the SFI signal as a sharp peak at relatively small F. The $m = 1$ states evolve largely diabatically but with a non-negligible adiabatic interaction at each crossing. Although the purity of the population through each crossing is roughly the same as for $m = 0$, the large variation in dipole moments causes the total energy of each state to become quite different. At each crossing, there is a non-negligible probability to mix with states of differing dipole moment which prevents the total energy differences between the states from becoming as large as in hydrogen. The $m = 2$ states evolve almost completely diabatically and they do not scatter into open channels once the energy is above $-2\sqrt{F}$. Because of the small quantum defects for $l \geq 2$, the states only decay once the energy of the n_1, n_2 level can classically decay at which point the electron leaves very rapidly. Thus, the $m = 2$ states give a series of peaks at very separated field strengths which reflects the original partitioning of energy into the up- and down-potential degrees of freedom and not the total energy of the state that is excited; this is an interesting feature which has not been observed before.

There are a couple of features in the contour plots of Figs. 2.5 and 2.6 that can be interpreted without recourse to extensive calculations. The first obvious feature is that the peak associated with $m = 0$ states emerges at smaller F as the energy increases. This occurs because the n levels increase with increasing energy; the $m = 0$ states evolve almost purely adiabatically and their energy hardly changes during the field ramp. The $m = 0$ levels are ionized as soon as the field strength is larger than $\sim 1/16n^4$ and are easier to ionize for larger n. Similar considerations hold for the $m = 1$ levels; although individual crossings are mainly diabatic, the sheer number of crossings gives an overall

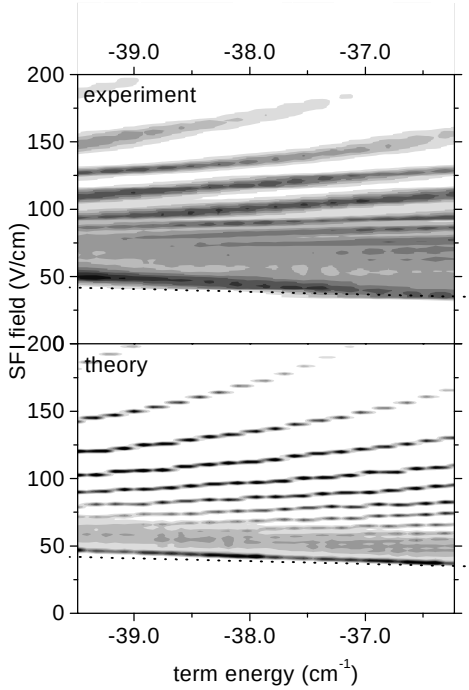

Figure 2.6: *Experimental and theoretical intensity map of the calculated SFI signal for Li. Same parameters as Fig. 2.5 but for perpendicular polarization. The dotted line shows* $F = (E/2)^2$.

spreading of energy without large energy shifts.

The SFI signal from the $m = 2$ states display a quite different feature (see Fig. 2.6). The $m = 2$ SFI consists of sharp horizontal bands that move to larger F as the energy increases. The explanation of this phenomenon is somewhat counter intuitive. One band does not correspond to a single state. This can be seen from the part of the bands above 150 V/cm; there it is clear that each band actually consists of short horizontal bands that step up to higher F as the energy increases. The explanation is that each band corresponds to an n-manifold. As the energy is increased, the state that is excited in each manifold is at higher energy (see Fig. 2.1) and thus has a dipole more strongly oriented to the up-potential side of the atom; in other words, states with more nodes in the up-potential coordinate, ξ, are being excited as the energy increases. These states evolve diabatically for $m = 2$ and thus are not stripped until very high field since the stripping field must increase when more energy is in the up-potential coordinate. The horizontal width of the mini-bands for $F > 150$ V/cm stems from the laser bandwidth assumed in the calculation.

We present a comparison between the experimental and calculated SFI signal for Rb in a 5 V/cm static field to contrast a more standard signal with the Li signal(Fig. 2.7); the ionization yield is peaked near $F = 1/16n^4$. The Rb atoms are excited from the

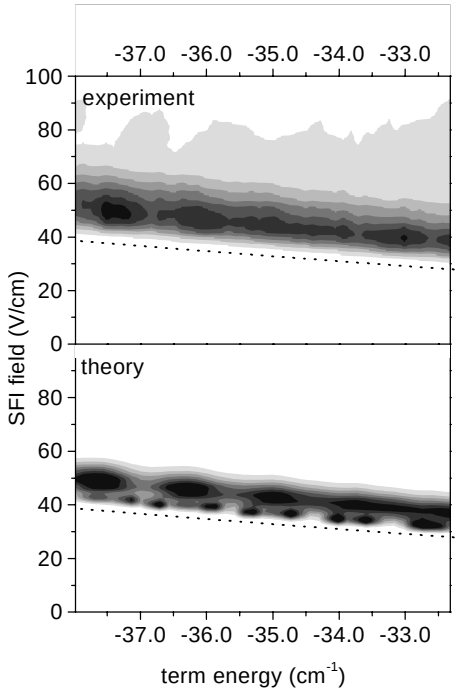

Figure 2.7: *Experimental and theoretical Rb SFI yield as a function of the term energy below the zero field ionization threshold and as a function of the SFI field. The Rb is excited in a non-resonant, two-photon transition with the laser polarized perpendicular to the electric field axis. The atom is in a static 5 V/cm field during the excitation. The dotted line shows* $F = (E/2)^2$.

ground state using a two-photon, non-resonant transition; the polarization of the laser is perpendicular to the field axis. Both $m = 0$ and $m = 2$ final states are excited with a ratio of 1:3. For Rb, the quantum defects are large for $l \leq 2$ and thus all of the levels cross adiabatically for both $m = 0$ and $m = 2$; the reduced quantum defects for Rb are $\bar{\mu}_0 = 0.14$, $\bar{\mu}_1 = -0.36$, $\bar{\mu}_2 = 0.35$, and $\bar{\mu}_3 = 0.02$. Thus, for Rb, the SFI signal is not sensitive to which Stark state in the n-manifold is excited; the SFI signal is only sensitive to the energy of the state. The Rb SFI can be made to behave more like that for Li by going to higher n states, ramping the field much faster, or by using an excitation scheme that would access $m = 3$ states.

Unlike the Li SFI signal, Rb only shows adiabatic ionization in this energy range and ramp rate. The peak value of F decreases as the energy increases because the electron is easier to remove as its binding energy decreases. Typically, the SFI signal is contained between $(2E/3)^2 > F > (E/2)^2$ when E is measured from the zero field threshold; as E increases, E^2 and F decrease.

2.4 Limitations of the Calculation

While our theoretical approach worked well for the cases presented here, there are some easily recognizable situations where the approximations may fail. For example, the approximations may fail if the ramping field does not have a simple form; a ramping field that has an oscillating component could cause trouble by having the phase on different paths become simply related to each other (see also Chapter 5). A more troublesome case is when the heavier alkali atoms are ramped from *zero* field; the method presented here works best when the electric field is strong enough to mix levels of different n-manifolds. In the method presented here, each population of a Stark state is propagated to higher field strength incoherently; for heavier atoms at weak fields, there are several low-l states that are essentially unmixed with the n-manifold and these should be treated as a coherent superposition of Stark states. Thus, the amplitudes should be propagated and not the population. Another difficulty with the heavier alkali atoms is that the spin-orbit interaction mixes states of different m at low field strength. Both deficiencies can be simply fixed by doing a numerical propagation of the Schrödinger equation to the n-mixing regime and then using the method described here to obtain the SFI distribution.

As a contrast, the SFI of ZEKE states should be simply accomplished using the methods described here. The reason is that the low angular momentum states can not be strongly populated for the molecule to have long lived Rydberg states. In typical ZEKE states, this is accomplished by an applied or a stray electric field that mixes the different l-states of an n-manifold. This is precisely the starting point of these calculations.

The last problem is that the method treats every crossing as separate and only involving two levels. There is the possibility for 3 level crossings once the field gets larger than $\sim 2/(3n^5)$. Examining the energy map for fields larger than this clearly show many 3 and 4 level crossings that are not a priori isolated, although clearly the majority of crossings are isolated 2 level crossings. The errors due to treating all crossings as isolated will need to be examined. It is our feeling that multiple crossings play very little role in the SFI signal. The reason is that it will take nearly perfect degeneracy between 3 levels to get an effect when the levels evolve mainly diabatically, $D \gg A$; but in this case most of the population will stay in the original state and thus the errors will be negligible. When the probability for an adiabatic transition, A, is not small, then the population does not spread far from the adiabatic path; thus most of the population remains within an energy width (determined by the 2 level crossings) of the original population and again there will be little error.

2.5 Discussion and Conclusions

We have presented a direct comparison between measured and calculated SFI distributions for Li and Rb. The computational method is an extension of well known techniques. The main innovation was to use WKB methods to obtain the parameters needed in the evolution of the wave function to the point the electron leaves the atom. We were able to interpret many features of the spectrum. When the atom is excited in a static electric field

and the states evolve diabatically, the SFI method is much more sensitive to the division of energy between the two parabolic coordinates than to the total energy of the state. This was the case for Li $m = 2$ states presented here; in this situation, the SFI method may be used for the characterization of a state distribution of the Stark levels within an n-manifold. This has relevance for ZEKE states. The ZEKE states arise through the mixing of high-l and m states with the initially excited low-l state; thus, the SFI spectrum of ZEKE states should behave most like SFI of hydrogen. Another important finding is that the calculation of SFI distributions is not as difficult as had been thought. This technique may be applicable to calculating properties of Rydberg atoms manipulated by other types of time dependent fields; for example, this method might be useful in calculations of ions scattering from Rydberg atoms.

Chapter 3

THz Ionization of High Rydberg States

A study of Rydberg atoms exposed to THz "half-cycle" pulses is presented. The THz "half-cycle" pulse can best be described as a fast (0.5 ps) unipolar pulse, followed by a much slower unipolar pulse of opposite polarity. Two regimes are observed where Rydberg atoms react different to the interaction with these "half-cycle" pulses. In the first regime the roundtrip time of the Rydberg electron (τ_n) is longer than the first fast unipolar pulse (τ_{hc}), but shorter than the duration of the full asymmetric mono-cycle (τ_{mc}): $\tau_{hc} < \tau_n < \tau_{mc}$. In the second regime the roundtrip time of the Rydberg atom is much longer than the full asymmetric mono-cycle: $\tau_n >> \tau_{mc}$. In the latter regime, ionization suppression and a much stronger redistribution is observed. Classically the observations can be explained by the following intuitive picture: the first fast unipolar feature corresponds to a start kick of the Rydberg electron, while the second unipolar feature acts as a stop kick. This results in hardly any energy exchange (ionization suppression). Instead a displacement of 2 μm of the Rydberg electron is realized, and the Rydberg state is altered.

3.1 Half-Cycle Pulse Ionization

The investigation of Rydberg atoms by "half-cycle" pulses in the THz regime has gained widespread interest since the possibility to generate these nearly unipolar electromagnetic waves. The first experiments [4] revealed that the interaction of Rydberg atoms by "half-cycle" pulses can best be described as an impulsive kick, since the duration of the "half-cycle" pulse (~ 0.5 ps) is much shorter than the roundtrip time of the Rydberg electron around the nucleus. The change in momentum ($\Delta\mathbf{p}$) is given by (atomic units are used, unless stated otherwise):

$$\Delta\mathbf{p} = -\int_{-\infty}^{\infty} \mathbf{F}(t)dt \tag{3.1}$$

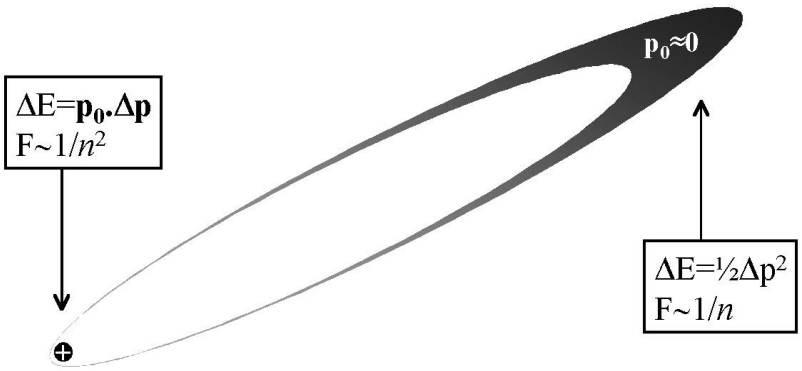

Figure 3.1: *Sketch of a Kepler orbit with low angular momentum. The electron spends most of its time far away from the core (indicated by the thickness of the black line). Close to the nucleus, "half-cycle" pulse ionization scales as* $\frac{1}{n^2}$*, while far away from the core ionization scales as* $\frac{1}{n}$.

where $\mathbf{F}(t)$ is the (time varying) electric field. The change in momentum corresponds to an energy change of:

$$\Delta E = \frac{1}{2}(2\mathbf{p}_0 \cdot \Delta\mathbf{p} + (\Delta\mathbf{p})^2). \tag{3.2}$$

If this energy change (ΔE) is greater than the binding energy of the Rydberg electron ($E = -\frac{1}{2n^2}$) the atom will ionize. In typical experiments, the Rydberg state is prepared by exciting a ground state atom with one or two lasers, resulting in a Rydberg state with low angular momentum (l). In such a elliptic orbit the Rydberg electron spends most of its time at the outer point of its Kepler orbit (see Fig. 3.1), where p_0 is zero. In that case $\Delta E = \frac{1}{2n^2} = \frac{1}{2}(\Delta\mathbf{p})^2$ and thus the field required to ionize is: $F \backsim \Delta p = \frac{1}{n}$. However, when the electron is close to the nucleus, p_0 is very large and will be the dominant term in Eq. (3.2): $\Delta E = \frac{1}{2n^2} = \mathbf{p}_0 \cdot \Delta\mathbf{p}$, resulting in $F \backsim \Delta p = \frac{1}{n^2}$. At low fields the ionization stems from electrons near the core and the ionization probability scales as $F \backsim \frac{1}{n^2}$, while large ionization probabilities scale as $F \backsim \frac{1}{n}$. It has experimentally been demonstrated and confirmed that an ionization probability of 10% of an ensemble of Rydberg atoms scales as: $F_{10\%} \backsim \frac{1}{n^2}$, while a 50% ionization probability scales as: $F_{50\%} \backsim \frac{1}{n^{3/2}}$ [4,45].

The term "half-cycle" pulse is not fully correct since Maxwell's equations demand that the time integral of the electric field in time is zero in free space for a propagating electromagnetic wave. The THz pulse can best be described by a very short half cycle pulse (duration: ~ 0.5 ps), followed by a much slower half cycle of opposite polarity and a much lower amplitude (typical pulse asymmetry: 13 : 1 [3,46]), so that the time integral of this asymmetric mono-cycle is zero (see Fig. 3.2a). The duration of the full asymmetric mono-cycle is then as long as $\sim$ 70 ps. For Rydberg states with a orbiting time much shorter than the duration of this second unipolar pulse but longer than the duration of the

first unipolar pulse, ionization occurs during the first half-cycle of the asymmetric mono-cycle. The ionization can than be described by "half-cycle" pulse ionization, neglecting the second unipolar feature. When the redistribution of these Rydberg states by "half-cycle" pulses is studied in this regime, the second unipolar feature acts as a DC offset for the Rydberg electron, so that it does not significantly contribute to the redistribution process [47].

However, the orbiting time of a Rydberg state scales as $\tau_n \backsim n^3$ (τ_n = 77 ps, for $n = 80$), and thus for Rydberg states with a sufficiently large principal quantum number, the orbiting time can become much longer than the duration of the full asymmetric mono-cycle. Beyond this principal quantum number, the duration of the full mono-cycle is short compared to the orbiting period of the Rydberg electron and the change in momentum is $\Delta\mathbf{p} = \int_{-\infty}^{\infty} \mathbf{F}(t)dt \approx 0$. This would result in very little energy change of the Rydberg electron.

Such an asymmetric mono-cycle does not leave the Rydberg state completely unaffected since the first unipolar feature kicks an electron in the direction of the polarization of the "half-cycle" pulse, while the second delayed unipolar pulse stops the electron again. Therefore, a displacement of the electron probability is introduced, by the fast start and the slow stop kick of the mono-cycle. For a free electron this displacement is ($m_e = e = 1$, in atomic units):

$$\Delta x = \int_{-\infty}^{\infty} dt' \int_{-\infty}^{t'} \mathbf{F}(t)dt. \tag{3.3}$$

In Fig. 3.2b the displacement of an unaccelerated electron by an asymmetric mono-cycle with a peak amplitude of 2 kV/cm (as is depicted in Fig. 3.2a) is plotted.

A Rydberg electron with an orbiting time much longer than the duration of a "half-cycle" pulse will be significantly displaced by such a "half-cycle" pulse since the change of velocity in an unperturbed orbit is negligible on the timescale of the duration of a "half-cycle" pulse. A displacement of 1.5 μm of a free electron is calculated for the "half-cycle" pulse of Fig. 3.2a, which means that the expectation value of the radial coordinate $\langle r \rangle$ of a Rydberg electron can be changed by as much as 1.5 μm ($< r >= 2n^2 \rightarrow n = \sqrt{\frac{1}{2} < r >} = 119$).

In this Chapter we investigate the effect of the second unipolar feature of half-cycle pulses in their interaction with Rydberg atoms, by studying the ionization and bound state redistribution of Rydberg atoms subjected to such THz radiation. For low principal quantum numbers ($n < 80$) hardly any redistribution is observed, and ionization probabilities are measured in accordance with the classical ionization laws. A strong ionization suppression, and bound state redistribution is observed for Rydberg states with high principal quantum numbers ($n >> 80$). A classical model is presented in which the ionization behavior and bound state redistribution of Rydberg states by these asymmetric mono-cycles is qualitatively explained.

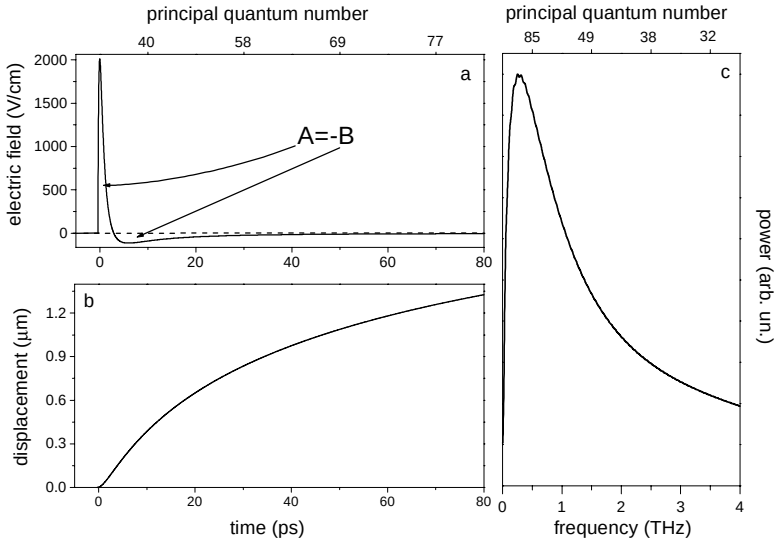

Figure 3.2: *a: A THz "half-cycle" pulse consists of a short unipolar feature, followed by a much slower unipolar feature of opposite polarity. On the top axis time (the Rydberg orbitting time) is converted into a principal quantum number:* $n = \left(\frac{t}{2\pi}\right)^{1/3}$. *b: A free electron is displaced by more than* $1.2\ \mu m$ *if it is exposed to the half-cycle pulse of Fig. 3.2a (amplitude:* $2\ kV/cm$*). c: Fourier transform of the pulseshape depicted in Fig. 3.2a. On the top axis frequency is converted into a principal quantum number:* $h\nu = E = \frac{1}{2n^2}$.

3.2 Experimental Realization

The preparation of Rydberg atoms in Li was done in a similar experimental configuration as described in Chapter 2. The setup is depicted in Fig. 3.3. A thermal beam of gas-phase lithium atoms, produced by a resistively heated oven, was directed in between two capacitor plates, to provide a homogeneous electric field. A hole (∅ 10.0 mm) in the center of the anode plate, was covered by a grid to minimize distortions on the electric field. This enabled the detection of ionized electrons, on a Micro Sphere Plate detector located 5.0 cm away from the anode plate. The cathode plate was connected to a pulse generator, which could ramp the voltage in a well defined time. The anode plate was connected to ground.

The unfocused output of two, narrowband, dye lasers were colinear directed in between the parallel capacitor plates on to the lithium atoms in crossed beam arrangement (see Fig. 3.3). The first laser excited the lithium atoms from the ground state to the $2p$ level (670.97 nm), while the second laser ($\sim$ 700 nm) was frequency doubled to excite lithium atoms from the $2p$ level to a well defined Rydberg state. The wavelength of the second exciting laser could be scanned in order to excite different Rydberg states.

Half-cycle THz radiation was produced by illuminating a biased GaAs semiconductor

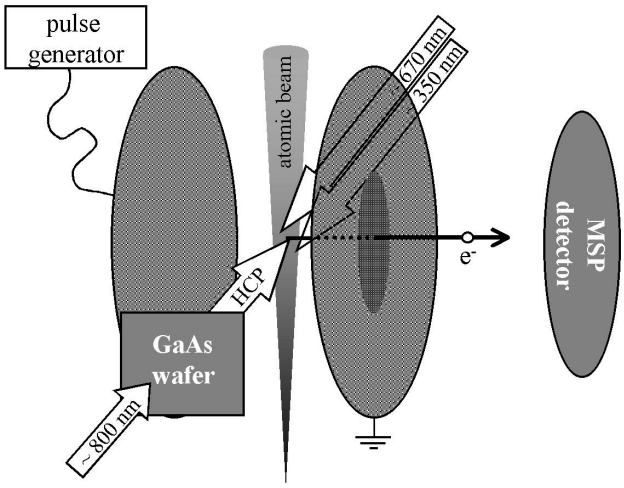

Figure 3.3: *Sketch of the experimental set-up.*

wafer with a short ($\sim$ 150 fs) laser pulse ($\sim$ 800 nm), originated from a Ti:Sapphire chirped pulse amplifier synchronized to the dye lasers. This radiation was aligned collinear with the optical laser beams, onto the Rydberg atoms. The peak value of the electric field of the half-cycle radiation, when it reaches the Rydberg atoms is proportional to the bias voltage over the wafer. The half-cycle pulse reached the Rydberg atoms approximately 500 ns after the excitation by the second narrowband laser.

Ionization and state redistribution has been monitored with the technique of Selective Field Ionization [2, 50] (SFI, Chapter 2). This technique makes use of the fact that every Rydberg state has a electric field strength associated with it for which it will ionize: $F = \alpha\frac{1}{n^4}$. This field strength can be calibrated (determining α) by exciting specific Rydberg states by a narrowband laser and determining the field required to ionize the Rydberg state. If one ramps the static electric field in time (ramping the voltage on the cathode plate) and monitors at which time ionization occurs one can deduce the bound state distribution of an atomic system. The integrated electron flux due to field ionization is a measure for the amount of bound state population.

3.3 Experimental Results

A THz ionization curve for a Rydberg state with a principal quantum number of $n = 70$ is depicted in Fig. 3.4a. The recorded "S-curve" is a typical signature of THz ionization. In Fig. 3.4b the corresponding SFI traces are depicted which show that mainly depletion of the initially prepared state occurs, with little redistribution. To validate that the ionization could be described by impulsive kicking of the Rydberg electron away from the nucleus, additional THz ionization curves were recorded for Rydberg states with a principal quantum number less than $n = 70$. Fig. 3.4c shows how the THz ionization probability of Rydberg atoms scales for the $n = 53$, 61, and 70 Rydberg states. Clearly the

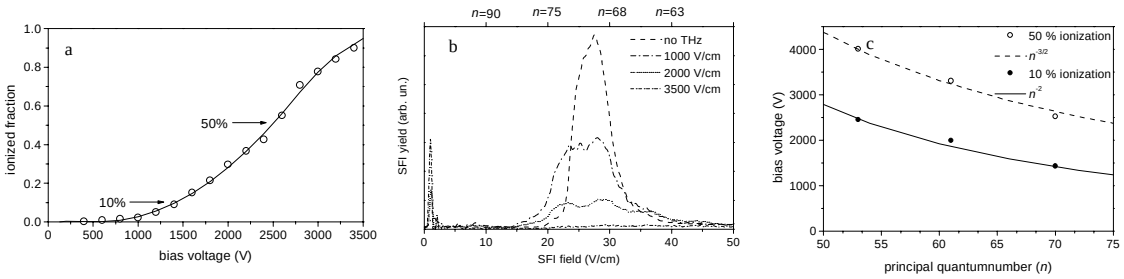

Figure 3.4: *Experimental THz ionization data for Rydberg states with a roundtrip time shorter than the duration of the asymmetric mono-cycle:* $\tau_n < \tau_{mc}$. *a: An experimental THz-ionization curve for a Rydberg state with* $n = 70$. *The two arrows denote what fieldstrength is required to ionize 10% and 50% of the Rydberg atoms. b: Three SFI traces obtained after exposing Rydberg atoms to a THz "half-cycle" pulse of* $n = 70$ *for three different amplitudes of the "half-cycle" pulse. c: Experimentally observed ionization probabilities for Rydberg states of* $n = 53$, 61, *and* 70. *The open dots correspond to 50% ionization probability, while the closed dots correspond to an ionization probability of 10%. The 10% and 50% ionization probability closely follow a* $\frac{1}{n^2}$ *(solid line:* $F = c_{10}\frac{1}{n^2}$, *with* $c_{10} = 7.0 \times 10^6$ V/cm*) and* $\frac{1}{n^{3/2}}$ *(dotted line:* $F = c_{50}\frac{1}{n^{3/2}}$, *with* $c_{50} = 1.6 \times 10^6$ V/cm*) scaling law respectively.*

$F \sim \frac{1}{n^2}$ (10% ionization) and $F \sim \frac{1}{n^{3/2}}$ (50 % ionization) scaling laws are retrieved. The 10% ionization probability dependency can be fitted by: $F = c_{10}\frac{1}{n^2}$, with $c_{10} = 7.0 \times 10^6$ V/cm, while the 50% ionization probability can be fitted by: $F = c_{50}\frac{1}{n^{3/2}}$, with $c_{50} = 1.6 \times 10^6$ V/cm. A ratio of $\frac{c_{10}}{c_{50}} = 4.5$ is obtained, in good agreement with the ratio determined from ref. [4] (there a ratio of $\frac{c_{10}}{c_{50}} = \frac{2.0 \times 10^6}{0.5 \times 10^6} = 4.0$ was observed).

For these Rydberg states, the roundtrip time ($\tau_n = 2\pi n^3$) of the Rydberg electron ranges from 22 ps ($n = 53$) to 52 ps ($n = 70$), which is shorter than the duration of the full asymmetric mono-cycle (τ_{mc}), but much longer than the duration of the first unipolar feature (τ_{hc}) in THz "half-cycle" pulses (see Fig. 3.2a) [4], and therefore the ionization can be understood as treating the THz pulse as a true half-cycle impulsive kick. In this study we focus on the regime where the duration of the second unipolar feature acts impulsive as well. This means that the duration of the full asymmetric mono-cycle should be much shorter than the roundtrip time of the Rydberg electron: $\tau_{mc} << \tau_n$. In this regime it is expected that the ionization mechanism of Rydberg states with these half-cycle pulses is altered by the second slower unipolar feature. This would correspond to Rydberg states of $n >> 80$ ($\tau_n = 77$ ps), since the duration of the whole asymmetric mono-cycle is as long as ~ 70 ps (see Fig. 3.2a).

In Fig. 3.5a the ionization probability is plotted versus the bias voltage of the semiconducting wafer for a Rydberg state with a principal quantum number of $n = 135$ ($\tau_n = 371$ ps). Two striking results are apparent. Firstly, it is not possible to achieve

a 100% ionization probability (the maximum recorded ionization probability was 75%). Secondly, there is a strong deviation of the classical ionization scaling law, since for low ionization probabilities less peak amplitude is required for ionization than predicted by the classical scaling laws (denoted by the dots in Fig. 3.5a). A Rydberg state with a principal quantum number greater than $n = 60$ (binding energy: $E = -\frac{1}{2n^2} = -1.4 \times 10^{-4}$ a.u.) has already some probability to be ionized by a single high frequency photon of the "half-cycle" pulse (1 THz$\cong$ 30 cm^{-1} $\cong$ 1.37×10^{-4} a.u., see also Fig. 3.2c). Therefore, the observation that lower amplitudes are required of the "half-cycle" pulse than predicted by the classical scaling laws can be explained by the fact that we are studying ionization in the one-photon ionization regime for these high Rydberg states ($n > 70$) as opposed to the multi-photon regime for Rydberg states with a principal quantum number smaller than $n = 70$, from which the classical scaling laws were deduced. It does however, not explain the ionization suppression (see section 3.5).

In Fig. 3.5b three SFI traces are depicted for $n = 135$ Rydberg atoms exposed to "half-cycle" pulses of different amplitudes (bias voltage: 250 V/cm, 500 V/cm, and 2000 V/cm). The SFI trace obtained with no THz shows the initial state distribution. Apparently, for these high n states, redistribution to mainly higher n-states occurs, instead of ionization. Notice that also more deeply bound states are created. This significant redistribution is not observed when we start out with Rydberg states with a principal quantum number below $n = 70$ as shown in Fig. 3.4b, indicating that the redistribution occurs due to the impulsive character of the second slower unipolar feature in "half-cycle" pulses. The shape of the SFI trace obtained by exposing Rydberg atoms to a "half-cycle" pulse of 500 V/cm, was not significantly altered when the amplitude of the "half-cycle" pulse was increased (up to 2000 V/cm).

THz ionization curves for Rydberg states of different n ($n > 70$) are depicted in Fig. 3.5c, showing that ionization suppression is stronger for Rydberg states with a higher principal quantum number. Moreover a clear disagreement is observed between the experimentally determined ionization probability and the ionization probability predicted by the classical scaling laws (Fig. 3.5d), accounting for the first unipolar feature only. In the next section we discuss a classical model which qualitatively explains the ionization suppression and redistribution to higher Rydberg states by asymmetric mono-cycle pulses.

3.4 Classical Calculations

Classical calculations were performed, taking into account the second slow unipolar feature in "half-cycle" pulses, to understand the observations. The equations of motion of a Rydberg electron around a nucleus in a time varying field were solved by the Runge-Kutta numerical integration method. The ionization probability of a "half-cycle" pulse of a fixed amplitude was calculated by determining the energy of a Rydberg electron after interaction with the "half-cycle" pulse, for various starting times of the "half-cycle"pulse during one Kepler orbit time. The probability is then determined by the sum of all the orbits which resulted in ionization ($E > 0$), divided by the number of different starting

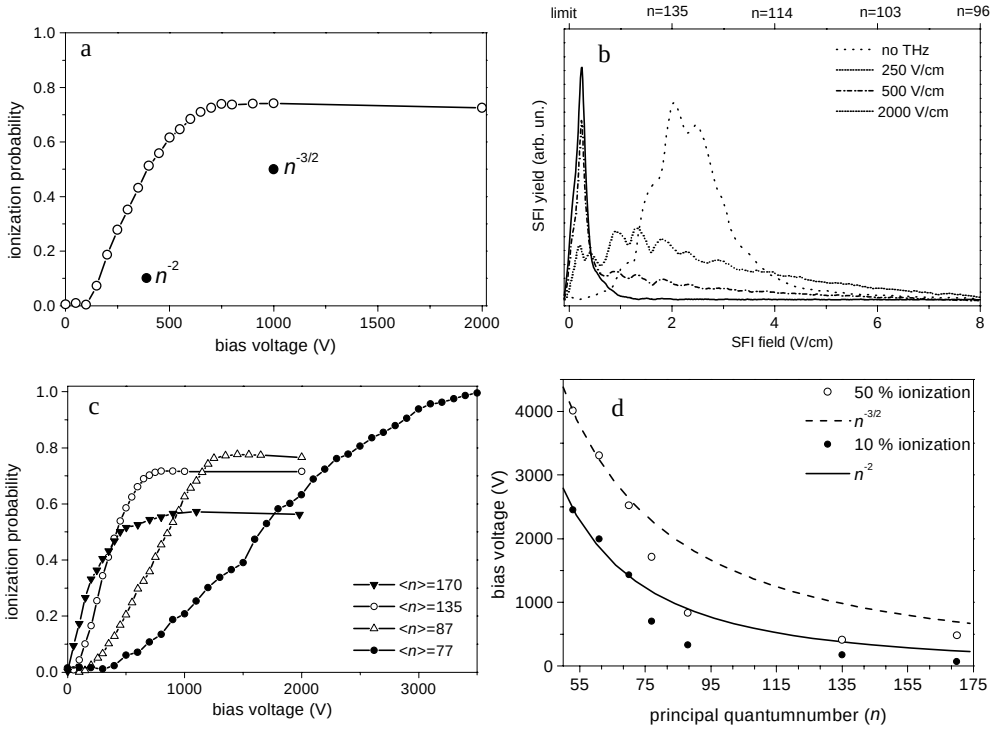

Figure 3.5: *Experimental THz ionization data for Rydberg states with a roundtrip time ($\tau_n = 371$ ps) much longer than the duration of the full asymmetric mono-cycle: $\tau_n >> \tau_{mc}$. a: THz ionization curve for a Rydberg state of $n = 135$. For these high n-states it is impossible to achieve 100% ionization. The two dots (•) denote what amplitude is required, predicted by the classical ionization laws, to obtain a 10% and 50% ionization probability. b: Two SFI traces obtained after exposing Rydberg atoms to a THz "half-cycle" pulse of $n = 135$ for two different amplitudes of the "half-cycle" pulse. The dotted line depicts the SFI trace when the Rydberg atoms were not exposed to THz radiation. c: THz-ionization curves for $n > 70$, showing that ionization is suppressed for higher Rydberg states. d: The experimentally determined 10% and 50% ionization probabilities compared to the classical scaling laws ($F_{10\%} \backsim \frac{1}{n^2}$, and $F_{50\%} \backsim \frac{1}{n^{3/2}}$). A strong deviation is observed for Rydberg states with $n > 70$.*

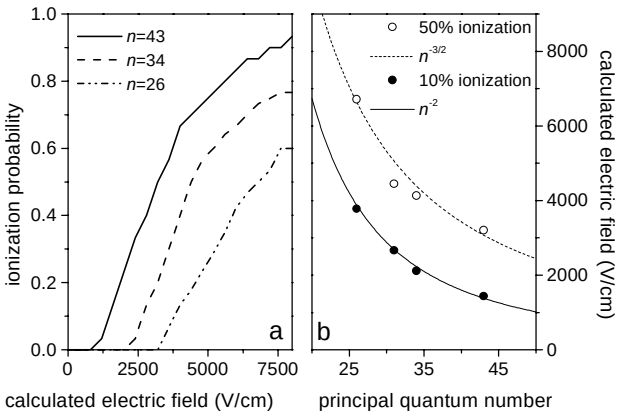

Figure 3.6: *Calculated ionization pobabilities for Rydberg states with a roundtrip time shorter than the duration of the full asymmetric mono-cycle:* $\tau_n < \tau_{mc}$. *a: Ionization probabilities for Rydberg states with an orbitting time much shorter than the duration a full THz asymmetric mono-cycle, but longer than the duration of the first unipolar feature in a THz "half-cycle" pulse. b: The 10% and 50% ionization propabilities, determined from the calculations, compared to the classical scaling laws (*$F_{10\%} \backsim \frac{1}{n^2}$, *and* $F_{50\%} \backsim \frac{1}{n^{3/2}}$*).*

times[1]. In Fig. 3.6a the calculated ionization probability is plotted for several Rydberg states ($l = 2$) with a principal quantumnumber of: $n = 26$, 34, and 43 by a "half-cycle" pulse which envelope is depicted in Fig 3.2a. Identical ionization curves were calculated, when the same calculations were performed with a true half-cycle pulse (only using the first fast half-cycle as the time varying field in the calculations) instead of the asymmetric mono-cycle of Fig. 3.2a. This shows that for Rydberg states with a sufficiently low principal quantum number (so that $\tau_n << \tau_{mc}$), the second slow unipolar feature does not significantly contribute in the ionization process. From the calculated THz ionization curves we determined the field required to obtain a 10% and 50% ionization probability, and the classical scaling laws were retrieved (see Fig. 3.6).

If the same model is applied to a Rydberg state with $n = 135$ ($l = 2$), a different ionization behavior is obtained. Due to the second unipolar feature, ionization is strongly suppressed. This can be seen in Fig. 3.7a where a calculated ionization curve by the asymmetric mono-cycle (as depicted in Fig. 3.2a) is compared to the calculated ionization curve by a "true" half-cycle pulse (FWHM 0.5 ps). For a free electron the energy exchange is zero, and thus it is understood that ionization is suppressed. The small ionization

[1]This is identical to performing a calculation where the starting time of the "half-cycle" pulse is fixed but the electron starts at different positions in its Kepler orbit, where the ionization probability is then obtained by summing all the orbits which resulted in ionization weighted by the expectation value of the starting position of each individual orbit.

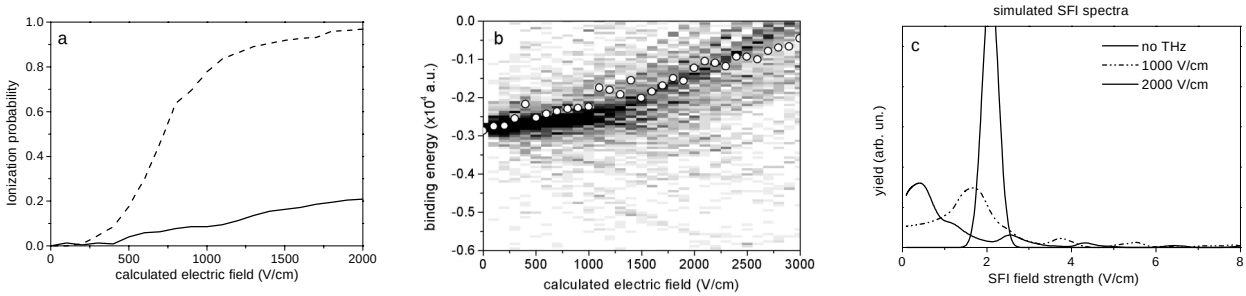

Figure 3.7: *a: Calculated THz ionization curves for a Rydberg state with a principal quantum number of $n = 135$ ($l = 2$). The roundtrip time of such a Rydberg state is much longer ($\tau_n = 371$ ps) than the duration of the asymmetric mono-cycle. Dotted line: calculated THz ionization for a true half-cycle pulse. Solid line: calculated THz ionization with a pulseshape as depicted in Fig. 3.2. b: Calculated redistribution of a $n = 135$, $l = 5$ Rydberg state as a function of the amplitude of the asymmetric mono-cycle. The open dots reflect to which average principal quantum number redistribution occurs, while the contour graph reflect the actual state distribution. c: Simulated SFI spectra from the state (re-)distribution obtained by the calculations. Notice the very good agreement with the experimental results depicted in Fig. 3.5b.*

probability comes from the fact that the velocity of the electron in its orbit around the nucleus is time dependent and thus $\Delta E = \int_{-\infty}^{\infty} \mathbf{v} \cdot \mathbf{F}(t)dt$ is not exactly zero resulting in some ionization.

Classical calculations were used to deduce in what manner the orbit of the Rydberg state is altered, since the suppression of ionization is qualitatively described classically. This can be done by calculating the interaction of a Rydberg state with a "half-cycle" pulse and determining the energy distribution of the Rydberg state afterwards. In Fig. 3.7b the calculated redistribution of a $n = 135$ Rydberg state is depicted. An average re-distribution to higher Rydberg states is observed. The SFI spectrum was simulated (Fig. 3.7c) for a fixed amplitude of the "half-cycle" pulse starting form the calculated state (re-)distribution. This was done by converting the principal quantum number of a Rydberg state into a field strength for which the specific Rydberg state would field ionize ($F = \alpha \frac{1}{n^4}$). These simulations reproduce the experimental observations very accurately (compare Fig. 3.7c with Fig. 3.5b). From the experimental SFI traces it is deduced that with a bias voltage of 2000 V redistribution occurs to Rydberg states with a principal quantum number of $n = 200$. The expectation value of the radial coordinate of the initial $n = 135$ Rydberg state is $< r >= 2n^2 = 2.1$ μm, and for a Rydberg state of $n = 200$ this expectation value is: $< r >= 4.2$ μm. Therefore, a Rydberg state of $n = 135$ is displaced by an asymmetric mono-cycle with a bias voltage of 2000 V/cm by ~ 2 μm.

3.5 Discussion and Conclusions

In this Chapter it is demonstrated that Rydberg atoms with a high principal quantum number ($n >> 80$) are robust against ionization by "half-cycle" pulses. Instead of complete ionization, redistribution to high Rydberg states is observed. Noël *et al.* [48] observed a similar effect when they exposed Rydberg atoms to few-cycle ($\sim$ 5 cycles) microwave radiation (4 GHz) with an amplitude 40$\times$ larger than required to ionize the initial state. Instead of ionizing the Rydberg atoms, "population trapping" in high n-states was observed. The observations presented in this Chapter close the gap between "half-cycle" pulse ionization of Rydberg states with $n < 70$, and few-cycle microwave ionization.

This experiment also relates to the study of ionization by short, far-infrared laser pulses by Hoogenraad *et al.* [49]. That study demonstrated that ionization of Rydberg states in the one-photon regime was suppressed for pulse durations shorter than the orbit period of the Rydberg electron. This was explained semi-classically: the wavefunction of a Rydberg electron performs a Kepler-like orbit around the nucleus. Only the wavefunction near the core can be ionized by the laser pulse. Since not all of the wavefunction passes near the core for a laser pulse much shorter than the Kepler orbiting time, the wavefunction far from the core is stable against ionization. The same semi-classical explanation cannot be applied to the observations reported in this chapter, since the ionization of Rydberg atoms by half-cycle pulses is understood as impulsively kicking the electron away from the nucleus. Therefore, ionization can still occur even when there is no wavefunction near the core.

An intuitive mechanism for the ionization suppression is presented in which the "half-cycle" pulse can best be described by a fast start kick and a slow stop kick of opposite polarity and lower amplitude. Instead of kicking the Rydberg electron away from the nucleus, the "half-cycle" pulse induces a new Rydberg orbit in which the expectation value of the radial coordinate of the Rydberg electron is altered. In other words: the Rydberg electron is displaced. This only holds in the regime where the time duration of the asymmetric mono-cycle is shorter than the roundtrip time of the Rydberg electron. In this regime population transfer mainly to high Rydberg states is predicted by classical calculations in agreement with experimental observations. The simulated SFI spectra from the calculated state distribution were in very good agreement with the experimental SFI spectra. It was experimentally and theoretically demonstrated that a $n = 135$ Rydberg state can be displaced by as much as 2 μm.

Redistribution of Rydberg states with a principal quantum number of $n = 50$ by slow unipolar (9 ns FWHM) electric field pulses, is discussed in Chapter 5. There it is demonstrated that even unipolar features in the nanosecond regime can have a strong effect on Rydberg states with a relatively low principal quantum number, and thus that in most cases one cannot neglect the mono-cycle nature of half-cycle pulses.

Chapter 4

Forced Autoionization

In this chapter we report on the autoionization dynamics of the 5d7d doubly excited state in barium in a static electric field. The different experiments and theory show Stark beatings in the autoionization process. It also appeared that the total spin of the two valence electrons, plays a major role in the ionization dynamics. Absorption spectroscopy revealed the ionization dynamics near the core, while an atomic streak camera was used to record the time-dependent electron emission, probing the wave function when it is far from the core. Calculations based on Multi-channel Quantum Defect Theory are compared to experimental data and we are able to predict the singlet-triplet mixing.

4.1 Introduction to Forced Autoionization

An atom in a doubly excited state has two electrons populating levels different from the ground state. These excited states can couple to states in which one electron has relaxed to the ground state and the other carries all the energy. If the total energy shared by the two electrons exceeds the binding energy, the second electron is forced to escape; the doubly excited state has decayed by autoionization into a ground state ion plus a free electron. If the total energy is less than the binding energy, the doubly excited state can only couple to bound Rydberg states. However, in the presence of a sufficiently strong electric field such Rydberg states couple to continuum states; the electric field introduces a saddle point in the core potential over which the electrons can escape (see Fig. 4.1). The process by which the doubly excited state couples to a Rydberg state, which in turn couples to the field-induced continuum, is known as forced autoionization [51] (see also Eq. (1.10)).

In this chapter we investigate the dynamics of such a forced autoionization process in the alkaline earth atom barium to learn more about the complex electron dynamics of a decaying two electron system. Starting from the ground state ($6s^2$) the 5d7d doubly excited state is laser-excited via the 5d6p laser-excited intermediate state. We studied the dynamics of the coupling to the $6s\epsilon k$ Rydberg series followed by the ionization of the Rydberg Stark states. The approach of our study is threefold. First we performed a high resolution spectroscopy study. This conventional means of studying the system [52, 53]

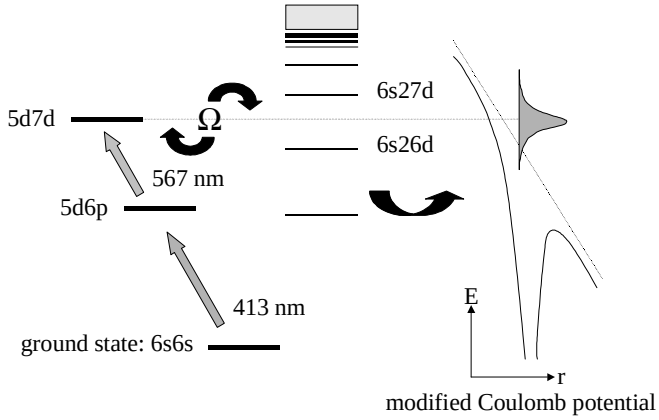

Figure 4.1: *The process of forced autoionization as studied in Ba. A doubly excited state is created by means of two consecutive laser pulses. The doubly excited state (5d7d) couples strongly to the 6snd Rydberg states through configuration interaction. These states in turn are coupled to a continuum in a strong electric field and can therefore autoionize.*

yields dynamical information equivalent to optical pump-probe studies with short laser pulses [54]. In such a pump-probe study the pump pulse creates a Rydberg wavepacket, Ψ, and after a delay time τ a second wavepacket is launched by the probe pulse. The interference of the two wavepackets is measured. Since the Rydberg wavepacket Ψ is a projection of the groundstate wave function on the Rydberg states, the launched wave packet $\Psi(t = 0)$ is near the core. As a result both spectroscopy and pump-probe experiments yield information on the low angular momentum character of the wavepacket near the core. With help of the recently developed atomic streak camera we are able to measure the outgoing electron flux with a picosecond resolution and thus probe the electronic wave function near the saddle point. Finally we applied a version of Multi-channel Quantum Defect Theory (MQDT) [42, 55–57] describing the dynamics probed by both types of experiments accurately.

We report on two remarkable findings on the forced autoionization dynamics of the barium 5d7d state. First, both the spectroscopy and the electron emission data showed a beating of the autoionization process. The angular momentum degeneracy is lifted by the electric field. The resulting Stark states are coherently excited, yielding an oscillation of the angular momentum (Stark beating) [58, 68]. However, the dynamics as seen with both techniques is not the same since they probe different parts of the wave function. Secondly, the nature of the dynamics is somewhat more complex than sketched above since also the spin of the two electrons is involved. The spin of the outgoing electron is anti parallel or parallel to the spin of the electron which is in the ground state Ba^+ (6s). We find that the dynamics of electron emission in the two spin channels is dramatically different. While direct ejection of the electron results mostly in a singlet state, the triplet emission is dominant for longer times.

4.2 Frequency Domain Experiments

Both experiments were performed in a vacuum chamber with a background pressure of 5.0×10^{-7} Torr. In our spectroscopy experiment, revealing the electron dynamics near the core, we populated a doubly excited state in barium by means of two narrowband pulsed dye lasers in a static electric field. The first pulse, with a central wavelength of 413.4 nm and polarization parallel to the electric field, excited ground state electrons in barium to a 5d6p intermediate state. The 5d7d perturber region was excited by a second ns pulse with a central wavelength near 567 nm and a bandwidth of < 0.1 cm^{-1}. The polarization of this pulse was either chosen to be parallel or perpendicular to the electric field. An atomic barium beam was produced by a resistively heated oven. The barium atoms were excited between two parallel capacitor plates 10.0 mm apart. The electrons, created by the autoionization process, are pushed through the grid in the anode plate towards a set of Multi Channel Plates. By scanning the second laser over the 5d7d perturber at a certain field strength we obtained the electron yield as function of the detuning from the perturber. Care is taken not to saturate the spectra with too much power, typically the power of the second laser was kept below $\sim$2 W/cm^2.

In Fig. 4.2 (top) a typical absorption spectrum is depicted. The sharp features are the resonances arising from the Stark states in the 6sϵk channels, while the overall broad feature is due to the coupling between the 6s channels and the 5d7d perturber and can be described by a Fano profile [66] with an asymmetry parameter (q) of -25. The width of this broad feature ($\approx$15 cm^{-1} FWHM) is representing the coupling strength between the perturber and the Rydberg series. The positions of the different resonances from the 6sϵk channels can be related to positions of the very blue Stark states [54] of lower lying n-manifolds (as low as $n = 22$, for 1600 V/cm). The reason that we are only seeing the blue states is because the wave function of these states is localized far from the saddle point, hence these states are long lived as opposed to red states which ionize instantaneously. A further investigation of Fig. 4.2 also shows that the resonances in the 6s channels appear as dips (window resonances) on the blue side ($\Delta E > 0$) of the perturber and as peaks on the red side of the perturber. This is due to the interference between electron waves from the different channels in the continuum channel. A theoretical calculation is depicted and the theory is in excellent agreement with experiment. To connect this absorption spectroscopy experiment to the Rydberg electron dynamics, we multiply an absorption spectrum with a Gaussian with a width and a central frequency corresponding to the width of a short broadband laser pulse. The Fourier Transform of the achieved spectrum shows the recurrence spectrum in which we can see Stark beats due to the coherent superposition of the 6sϵk Stark states. In Fig. 4.2 (bottom) a Fourier Transform is depicted for a Gaussian pulse with a central wavelength of 566.77 nm and a pulse duration of 7.5 ps. Clearly, a beating pattern is resolved which is inversely proportional to the energy separation of the different Stark states (in atomic units): $\tau = \frac{2\pi}{\Delta E}$.

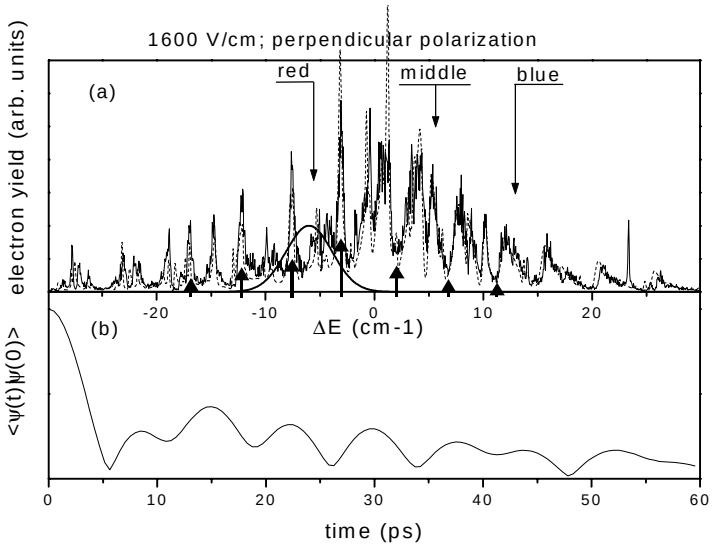

Figure 4.2: *(a) Ionization signal as a function of the detuning of the second narrowband laser pulse. The barium atoms were excited with a polarization perpendicular to a static electric field of 1600 V/cm. The energy is with respect to the zero field position of the 5d7d state (41841.66 cm^{-1}). The markers red, middle, blue will be used as a reference in Fig. 3 and 5. The bold vertical arrows denote the position of the 7 bluest Stark states of n=22, showing window resonances on the blue side of the perturber, where the arrows line up with valleys in the experimental spectrum. The sharp resonance at $\sim$ 23 cm^{-1} is due to a slight (0.1 %) strontium contamination of the barium sample. Note the excellent match with theory (dotted line). (b) Fourier Transform of a convoluted spectrum with a width of 5.0 cm^{-1} and a detuning of -6.0 cm^{-1} (denoted by the Guassian curve in the upper graph).*

4.3 Time Domain Experiments

In order to measure the electron emission of the forced autoionization process, we have used an atomic streak camera [67] with picosecond resolution. The principle is as follows and is sketched in Fig. 4.3. Barium atoms are excited in a crossed beam arrangement between two plates (separation = 10.0 mm) over which the static field is applied. The second plate has a slit parallel to the beam direction through which the electrons can leave the interaction region. Behind this plate a sweeping electric field is created (synchronized with the laser pulse) between two deflection plates, perpendicular to the previous plate set and perpendicular to the direction of the electron flux. This electric field typically sweeps from -0.5 kV to +0.5 kV in 500 ps. Therefore electrons arriving at different times in the deflection region experience a different voltage and are recorded on a different position on a set of Multi Channel Plates in combination with a phosphor screen which images the deflected electrons.

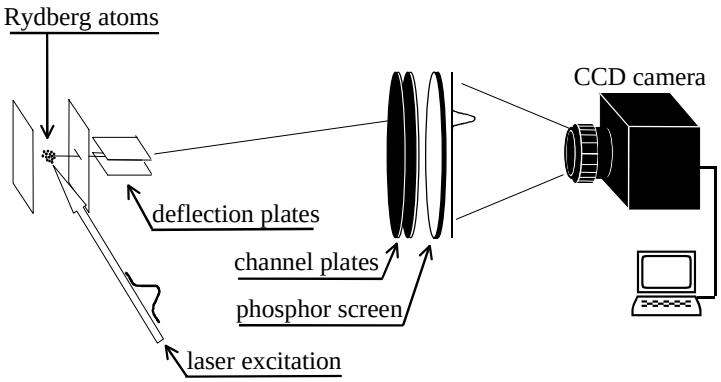

Figure 4.3: *The atomic streak camera setup. A doubly excited state in Ba atoms is created by means of a ns dye laser and a short ps dye laser (see text). Due to the presence of a strong electric field, Forced Autoionization occurs. The emitted electrons are accelerated to the right in the figure and arrive between two deflection plates. One of the deflection plates can be rapidly charged by a capacitor, triggered by optically switching a piece of GaAs. The time difference between electrons arriving between the deflection plates is thus converted into a deflection angle. The electrons strike a Multi Channel Plate set and the resulting signal is detected by a Phsophor screen. A CCD camera is used to record the light of the phosphor screen.*

This experiment involved the investigation of the same doubly excited bound state, with the same excitation scheme as in the absorption spectroscopy experiment, except that the second narrowband pulse is replaced by a picosecond pulse with a tunable central frequency. The recorded autocorrelation width of the amplified pulses (500 μJ, 10 Hz) of 10 ($\pm$1) ps corresponding to a pulse duration of 7 ($\pm$0.7) ps indicates that the pulses are near transform limited given the spectral width of 5 ($\pm$1) cm^{-1}.

The streak camera experiment in its turn reveals information on when the wavepacket is far from the core and the atom emits electron flux. In Fig. 4.4 three different electron emission traces (filled circles) are depicted at the same field strength (1600 V/cm) but for different values of the central wavelength of the ionizing broadband pulse. Note that the electron emission is not instantaneous, which could be expected due to the relatively strong coupling between the perturber and the structured continuum (a coupling of 15 cm^{-1} corresponds to a coupling time of 0.8 ps). Instead Stark beatings are resolved especially to the red side of the perturber. It appears that the ionization dynamics strongly depends on which wing of the perturber one is exciting: recurrences are strongest when one is detuned from the perturber and the overall structure is strongly influenced by the central wavelength of the ionizing pulse. At the center of the perturber there seems to be no effect of angular recurrences and the streak trace seems to follow an monotonic decay. At these three frequency positions we have performed Fourier Transformations from the spectroscopy data in Fig. 4.2, and the results are depicted in Fig. 4.4 (solid line). The

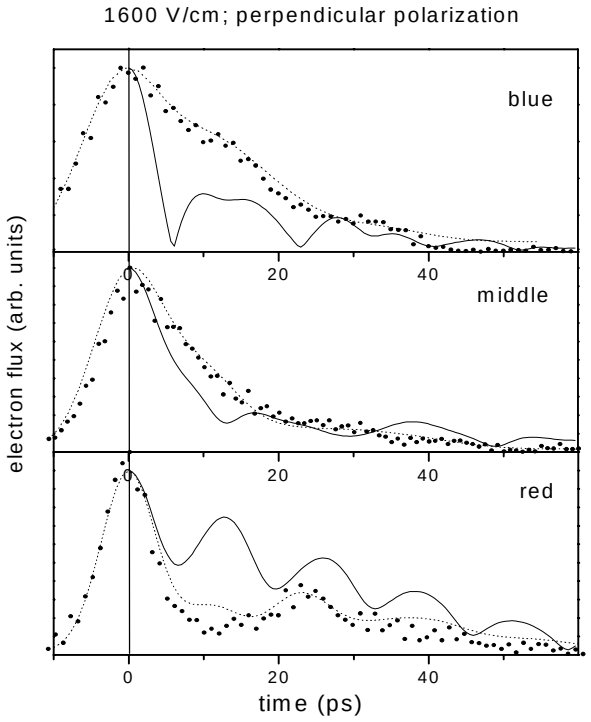

Figure 4.4: *Three electron emission traces (filled circles) taken with a 7.1 ps pulse at positions in the frequency domain corresponding with the labels in figure 4.2. Red has a detuning of -11.0 cm^{-1} , middle a detuning of 1.2 cm^{-1}, and blue a detuning of 10.0 cm^{-1} with respect to the perturber. Each trace is compared to theory (dotted line). Also Fourier Transforms are depicted (solid lines) at the corresponding positions in the frequency domain.*

stronger recurrences on the red side of the perturber are due to the sharp resonances compared to the window resonances on the blue side. This effect can also be seen in the Fourier Transform spectra. We have now probed the wavefunction of a two electron system both near the core and when it is near the saddle point where it can autoionize due to the field. Note that the recurrence lifetime is not the same as the lifetime deduced from electron emission. This is particularly clear at the blue side, where the optical pump-probe experiment suggests that the lifetime is much shorter than the streak traces show. In fact these measurements show that the electron is still bound (still signal to come in electron emission) but not near the core (no more signal in recurrence spectrum).

We also studied the effect of changing the saddle point position. Because strong electric fields are used the saddle point is far away from the relevant 6sϵk states in energy, and the detuning of the laser which excites to the 5d7d perturber has a negligible effect on the position in energy of the created wavepacket above the saddle point. Therefore one can investigate the effect of the static electric field (that is: the position of the saddle

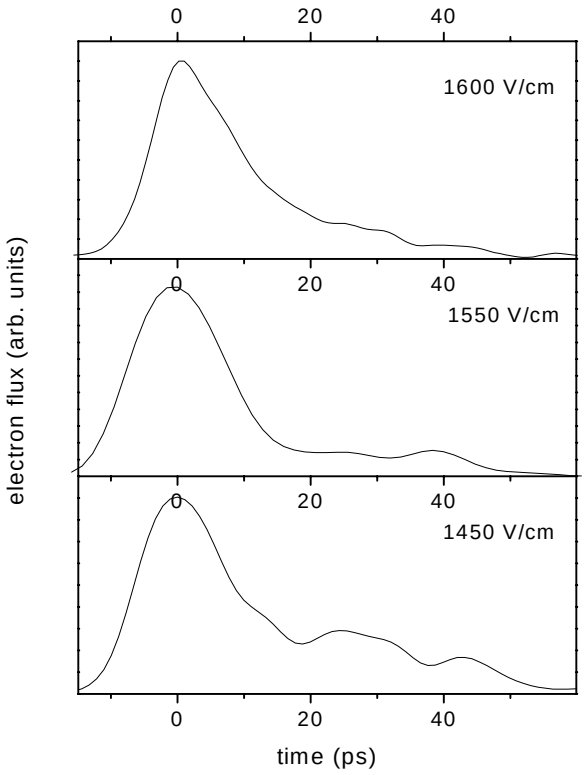

Figure 4.5: *Three electron emission traces with zero detuning but taken with different electric field strengths, for perpendicular polarization. The field-strength is known with a 10% accuracy.*

point) and the detuning independently. The field at which the n∼26 Stark states are at the saddle point is 702 V/cm ($F = \frac{1}{16n^4}$) and one would expect that it will be harder for the wavepacket to escape over the saddlepoint, as the field decreases towards this value. In Fig. 4.5 this effect is indeed observed: the electron flux extends out to much later times when the perturber is excited in a field which brings the perturber closer to the saddle point. Also we observe that even though we are exciting at the center of the perturber, recurrences are starting to appear at 1440 V/cm, while at higher field strengths the streak traces at this position show a monotonic decay.

4.4 Multi-Channel Quantum Defect Theory

This series of experiments was also supported by theory and in Fig. 4.4 each streak trace (filled circles) is compared to the calculation (dotted line). Clearly we have shown how powerful the theory is in reproducing the data from the two experiments. The calculations are based on the Multi-channel Stark Theory developed in Ref. [56, 57, 59], which are also described in Chapter 2. This formulation uses the WKB treatment of the Stark problem

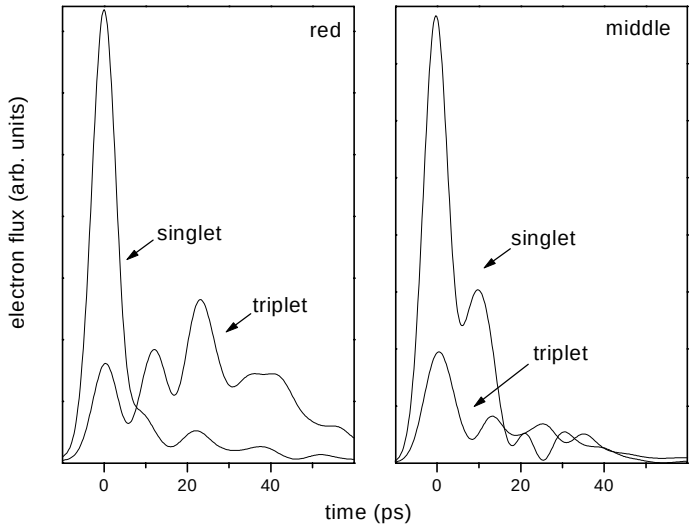

Figure 4.6: *The two panels show the calculated character of the electron flux at different energies (labels of figure 2). Clearly singlet-triplet mixing is observed, especially for the red case.*

developed by Harmin [42, 55] to obtain the dipole matrix elements and the wave function far from the nucleus. With this information and the asymptotic form of the wave function, we calculate the time-dependent flux of electrons when the system is excited by a pulsed laser. Previous (nondynamical) theoretical investigations of non-alkali atoms in external fields are described in Refs. [51, 60–65].

The calculation proceeds in two stages. In the first stage, we obtain the zero-field dipole matrix elements and K-matrices for Ba by slightly modifying the results from an R-matrix calculation in LS-coupling [59]. The spin-orbit effects are incorporated by using an LS to jQ frame transformation for the dipole matrix elements and the K-matrices and using the experimental threshold energies to obtain the zero-field Rydberg states at the correct energies. In the second stage, the wave functions in spherical coordinates are transformed into parabolic coordinates [42, 55] to account for the effects from the electric field in a nonperturbative manner. The time-dependent flux of electrons into the streak camera is simulated by superposing the energy-dependent wave functions with the appropriate coefficients which are the dipole matrix elements and the energy-dependent amplitude for the photon [56, 57]. In a previous investigation [51] of the same system a simpler model gave quantitative agreement due to lower resolution and the application of higher field strengths which induced rapid field induced ionization.

With the help of this extended theory we are now able to probe the effect of mixing which could not be retrieved from the experiments. We focused especially on the singlet-triplet mixing of the 6sϵk channels. The two relevant channels are denoted as the 6snd $^1D_2$ and the 6snd $^3D_2$ channel. In Fig. 4.6 a surprising effect is shown. The two graphs show the calculations of the electron flux with either singlet or triplet character. It appears

that even though if one initially excites mainly singlet character (red position), nearly all the electron flux coming out at later times is due to mixing of singlet character into triplet, while the singlet character decays almost instantaneously. Apparently only the sharp resonances have a long enough lifetime to acquire substantial mixing. Therefore at the perturber, where the decay is relatively fast, the singlet-triplet mixing is strongly suppressed. The effect is the strongest to the red side of the perturber where in the frequency spectrum the sharpest resonances were seen.

4.5 Discussion and Conclusions

In conclusion, we have measured the process of forced autoionization both in the time- as in the frequency-domain. Both experiments revealed complementary dynamical information, which could be interlinked by performing Fourier Transformations. Stark beatings are observed in both experiments, even though we initially excite a deeply bound doubly excited state (5d7d). Theoretical calculations yielded good agreement for both experiments. Therefore we were able to use theory as a third tool to study the dynamics involved in the forced autoionization process. In particular we focused on the effect of the singlet-triplet mixing. It appears that singlet character ionizes almost immediately while the decay at later times has mainly triplet character.

Chapter 5

Frustrated Breaking

We report on the observation of stabilization of laser-excited rubidium Stark atoms above the classical ionization limit with the help of short (9 ns) unipolar electric field pulses. Dipping the field down from 40 V/cm to 0 V/cm and back to 40 V/cm 30 ns after the photoexcitation into the continuum, yields a large bound state population.

5.1 Rydberg Atoms in Time-Dependent Electric Fields

In this Chapter we demonstrate that the ionization of a laser-excited Rydberg state can be frustrated by an external time-varying electric field. Frustrated ionization has a close resemblance to the recombination of a free electron and an ion, since a new bound state is made from a classically unbound system. In fact this study was performed as a "pilot" study for the development of a novel and controllable recombination scheme as discussed in Chapter 6, 7, and 8.

The behavior of Rydberg atoms in fast oscillating electric fields has been studied extensively by several groups [41,69–75]. Especially, the ionization behavior with microwave electric field pulses has been of interest. For ionization of Rydberg atoms in a static field, the corresponding electric field F is given by $F = \frac{1}{16n^4}$, at microwave frequencies ionization already occurs at fields as low as $F = \frac{1}{3n^5}$ [74] (atomic units are used unless stated otherwise). In a microwave field successive Landau-Zener crossings between a Stark state from a certain n-manifold to a Stark state from one higher lying n-manifold causes the ionization to occur. Once in the continuum successive Landau-Zener transitions can still occur within the lifetime of the continuum states (route A in Fig. 5.1).

The question now rises if the inverse process can also occur: would it be possible to induce bound states with microwave fields starting out in a (static) field induced continuum and make a Landau-Zener crossing to more deeply bound states by half of a cycle of the microwave field (route B in Fig. 5.1). And if this is possible: does a microwave field play an important role when the electron is in the field induced continuum? Bensky *et al.* [78] reported on similar "recombination" schemes using half cycle pulses in the sub-

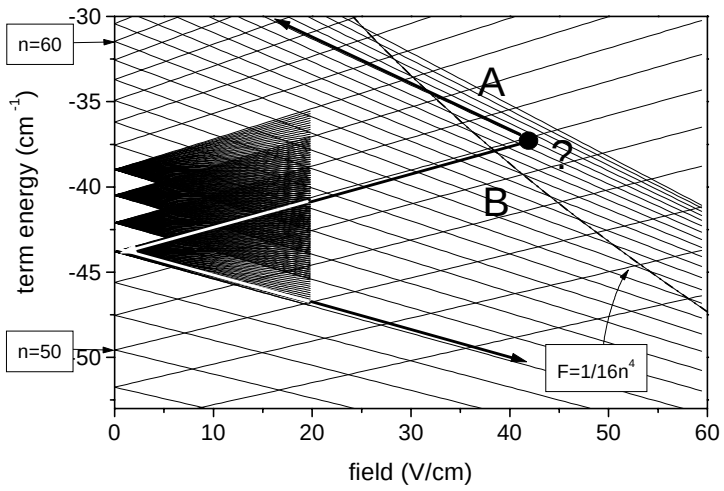

Figure 5.1: *Stark-map of rubidium, only the lowest and highest k-states of each n-manifold are shown. The dotted line depicts the position of the classical ionization limit. In the experiments the atoms are photo excited above the field ionization induced threshold and after a fixed delay a unipolar field pulse is applied, which dips the field down and back up again within 9 ns. The question rises in what manner the ionizing states are affected: two trajectories (A and B) are suggested to play a role.*

picosecond (THz) regime (Chapter 3). In this chapter we report on the remarkable finding that actually unipolar pulses in the nanosecond regime can be used to "recombine" an electron in the field induced continuum with its parent ion. For the THz experiments reported in Ref. [78] the half-cycle pulse is much shorter than the Kepler orbit period and the action of the pulse can be described as a momentum kick: $\Delta p = \int_{-\infty}^{\infty} F dt$. For the nanosecond field pulse reported here, the pulses are relatively slow and a description in terms of level crossings seems to be more applicable. The study of novel schemes to recombine free particles is interesting from the point of view that there has still not been found an efficient way to recombine an ion with an electron.

5.2 Experimental Realization

Schematically the experimental procedure we use is as follows (see also Fig. 5.2): first we excite gas-phase rubidium atoms with an 8-ns laser pulse above the classical field induced saddlepoint ($F = \frac{1}{16n^4}$), then we apply an unipolar pulse by which we hope to induce bound states, and finally we use Pulsed Field Ionization [2, 35] (PFI, Chapter 2) to determine the bound fraction. By increasing the electric field gradually one can ionize a highly excited atom due to the suppression of the ionization limit by the static electric field, and the amount of bound state population can be determined. A thermal atomic rubidium beam (produced by a resistively heated oven) is pointed in between two

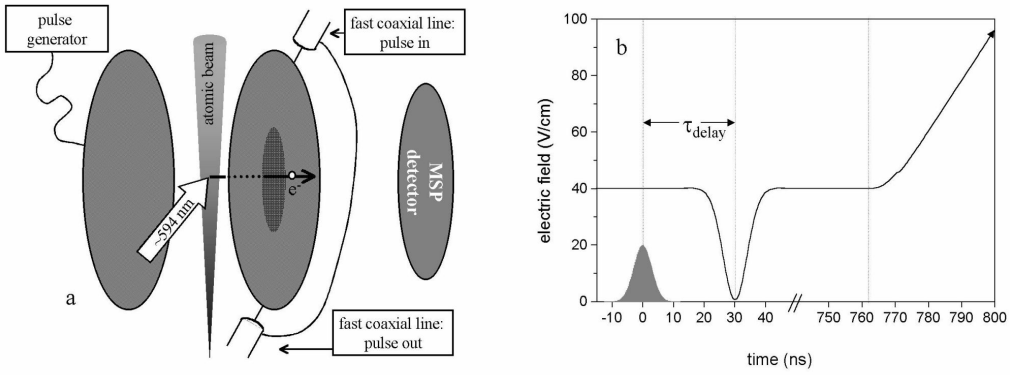

Figure 5.2: *a: Experimental configuration. Rubidium is excited inbetween two parallel capacitor plates. The cathode plate is connected to a slow pulse generator for PFI detection (see text). The anode plate is connected to a fast pulsegenerator with the aid of fast coaxial lines. b: Timing scheme of the experiment: at t=0 a ns, narrowband, laser pulse is used to excite Rydberg states in the vicinity of the saddlepoint in rubidium in a static field of 40 V/cm. After 30 ns the field is dipped down to zero field and back up again to 40 V/cm within 9 ns. After ∼750 ns an electric field ramp is applied to determine the fraction of the excited state population that is stabilized in a bound state.*

capacitor plates (diameter: 50 mm, thickness: 1 mm), separated by 10.0 mm. The Rb atoms are excited in a non-resonant two-photon process by means of a narrowband ($\Delta\lambda \leq 0.2$ cm^{-1}) dye-laser pulse above the classical ionization limit in a static field of 40 V/cm (see Fig. 5.2a). The plate furthest away from the detector (a set of micro sphere plates) is connected to a box that generates the (slow) voltage ramp for the pulsed field ionization detection (-400 V in 500 ns) superimposed on an offset of -40 V. The plate closest to the detector (the anode plate) is connected to the HP 8141a pulse generator, which produces the 9 ns (FWHM) unipolar pulses, the amplitude of which could be tuned from 1.00 to 50.00 V. Through this plate a hole (diameter: 10 mm) is drilled, which is covered by a grid to minimize the distortion on the electric field. Approximately 35 ns (variable) after excitation, the field is ramped down to 0 V/cm and back up to 40.0 V/cm within 9 ns. Ringing was minimized by matching the impedance of the pulse generator to the anode plate by using fast coaxial lines connected on two opposite sides of the capacitor plate (see Fig. 5.2a). One coaxial line was directly connected to the HP 8141a pulse generator while the other was used as a monitor line to measure the pulse profiles and calibrate the amplitudes, using an appropriate termination (50 Ω). Approximately 750 ns after excitation, the field is increased to 400 V/cm in 500 ns to field ionize the bound states created by laser-excitation. The parameters varied accurately in this experiment were the frequency of the dye laser, which photo-excited rubidium atoms, and the delay of the field pulse relative to the laser pulse.

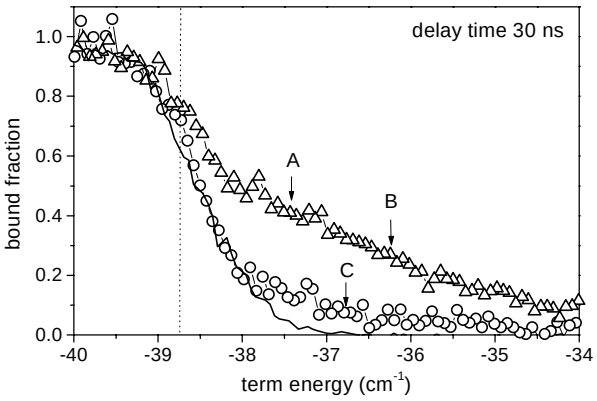

Figure 5.3: *Bound state population as function of the frequency of laser. The unipolar pulse was applied 30 ns after laser excitation. Both polarizations of the laser field with respect to the static electric field are shown (open circles: parallel polarization, open triangles: perpendicular polarization). The solid line represents the integrated PFI signal as a function of the wavelength of the exciting laser when no unipolar field pulse is applied. The labels A (E=-37.4 cm^{-1}), B (E=-36.2 cm^{-1}), C (E=-36.8 cm^{-1}) are markers which will be referred to later on. The vertical dotted line depicts where the classical ionization limit is at 40 V/cm.*

5.3 Experimental Results: Frustrated Ionization

In Fig. 5.3 the open triangles and circles show the "recombined" fraction, for perpendicular and parallel polarization of the laser-excitation with respect to the static electric field of 40 V/cm, when 30 ns after excitation we apply an unipolar pulse which dips the field down to 0 V/cm and back up again to 40 V/cm as a function of the term energy.

In a static electric field of 40.0 V/cm the photoionization threshold is lowered by -38.7 cm^{-1}, therefore states with a principal quantum number of 54 or higher ionize, since they are above the field-induced saddle point in the modified Coulomb potential. In Fig. 5.3 we show the recorded bound state signal as a function of the wavelength of the exciting dye laser in a static electric field of 40.0 V/cm without an electric field kick (solid line). A sharp step is observed in the PFI signal as a function of the wavelength of the exciting laser. Also the position of this step agrees with the theoretically predicted value of the threshold $E = E_0 - \frac{1}{16n^4}$. However, when we ramp the field down and back up again after excitation with a laser pulse with a polarization perpendicular to the electric field, it appears that we are able to "recombine" free states to bound states. Fig. 5.3 depicts this effect: the step function shape at the position of the saddle point in the static electric field case totally diminishes when after excitation in a static electric field a unipolar pulse is applied, indicating that we are indeed able to induce bound states from states above the field induced saddle point. Note that for the perpendicular case, even for excitation of states 5 cm^{-1} above the saddle point, a bound fraction of at least 0.1 is recorded.

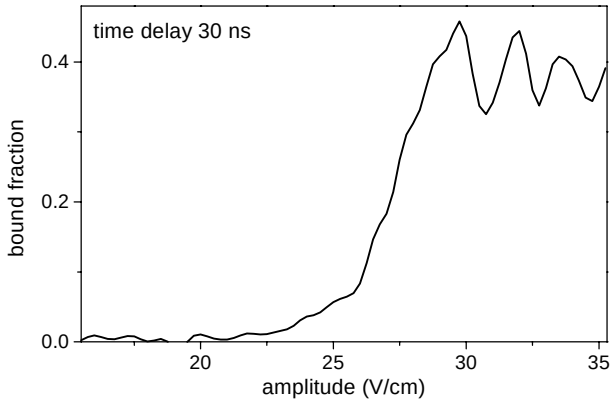

Figure 5.4: *Bound fraction as a function of the unipolar pulse amplitude. The unipolar pulse was applied 30 ns after laser excitation of Rydberg states with a term energy of* $E = -37.4\ cm^{-1}$ *(position A in Fig. 5.3).*

In Fig. 5.4 the bound fraction is plotted versus the amplitude of the unipolar pulse for a fixed wavelength (position A in Fig. 5.3), showing that for amplitudes lower than 25 V/cm no "recombination" occurs. For amplitudes higher than 27 V/cm pronounced oscillations are observed. In section 5.5 we discuss how interfering pathways in the Stark-map (see Fig. 5.1) can yield such oscillations.

5.4 Experimental Results: Lifetime Measurements

We are able to extract information on the lifetime involved in the "recombination" process, when we fix the wavelength to a value which excites the rubidium atoms above the saddle point and scan the delay time of the unipolar pulse with respect to the time of excitation. In Fig. 5.5 the bound fraction as a function of the time delay for different values of the wavelength of the ionizing laser is depicted. We again can clearly see that the lifetimes of the parallel excited states are substantially shorter than the lifetimes in the perpendicular case [79]. However, even well above the saddle point there are still states which have surprisingly long lifetimes for both the parallel and for the perpendicular case. This can be understood with the help of semi-classical arguments: in the case of parallel polarization each scatterwave evolves partially towards the saddle point (along the polarization axis, m=0), while for perpendicular polarization not much scatter wave travels towards the saddlepoint (mainly m=2).

5.5 Origin of the Oscillations

Oscillations were observed (see Fig. 5.5) for unipolar pulse amplitudes higher than 27 V/cm. Below we will discuss two possible models describing these oscillations qualita-

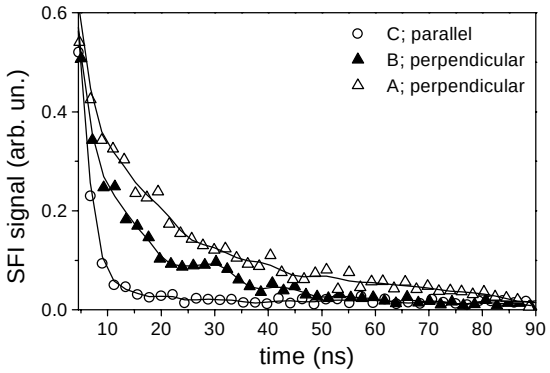

Figure 5.5: *The three traces show the bound state population as a function of the time delay of the unipolar field pulse with respect to the ionizing laser pulse. The labels A, B, C correspond to the markers in Fig.5.3. Traces A and B represent data taken with perpendicular polarization, while trace C represents data taken with parallel polarization.*

tively. The first model accounts for the phase accumulation of individual Stark states. During an avoided crossing the wavefunction ($\Psi(t)$) with an amplitude c, can be split up into two states with the wavefunctions: $a\Psi_1(t)$ and $d\Psi_2(t)$ (with $a^2 + d^2 = c^2$, see Fig. 5.6). Since the energy levels are time dependent in a time varying electric field ($E(t) = -\frac{1}{2n^2} + \frac{3}{2}F(t)nk$, where n is the principal quantum number and k the parabolic quantum number), the two wavefunctions accumulate their own amount of phase (ϕ): $\Psi_i(t) = \psi_i e^{-iE_i t} = \psi_i e^{-i\phi_i}$. If in a additional crossing the two states "meet" again, they can destructively or constructively interfere. Constructive interference occurs when the phase difference is an integer multiple of 2π, while destructive interference occurs when the phase difference is an integer multiple of π [76]. When the amplitude is varied in this experiment, the ramp rate ($\frac{dF}{dt}$) is varied, and thus the amount of phase collected by the different states is varied. A rough estimation of the phase difference due to crossings in the Stark-map for states with a principal quantum number of $n = 50$, can be done with the following expression, by taking only into account the reddest ($k = -n$) and the bluest ($k = n$) states of two adjacent n-manifolds:

$$\Delta\phi = \Delta E \Delta t \approx 4 * \frac{3}{2}\Delta F nk \frac{\Delta F}{S} = 6\frac{\Delta F^2 n^2}{S} \tag{5.1}$$

with ΔF the electric field difference between two consecutive crossings ($\approx$ 0.1 V/cm), and S the slew rate of the electric field pulse. For a slew rate of 4.0 $Vcm^{-1}ns^{-1}$ this phase difference is 0.3 rad. Peaks (constructive interference) are retrieved with a period of $\Delta F \approx 2$ V/cm (see Fig. 5.5), this would correspond to a phase difference of 6 rad which is very close to 2π, where we would expect constructive interference again. We therefore propose that the oscillatory behavior could be due to interference effects in the Stark-map induced by avoided crossings.

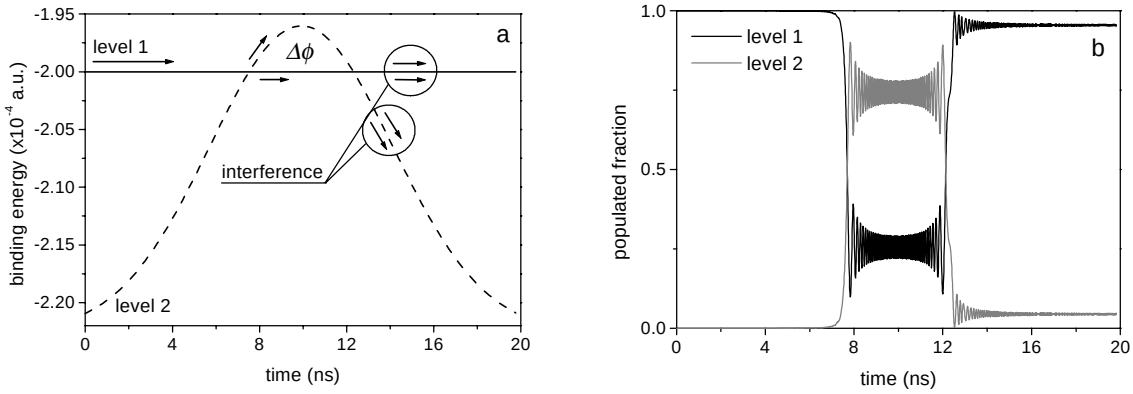

Figure 5.6: *Interference by a double Landau-Zener crossing. a: The dotted and solid line depict the energy dependence of two different states as a function of time. An initial state $\Psi(t)$ splits up into two states in the first crossing: $a\Psi_1(t)$ and $b\Psi_2(t)$. The phase difference ($\Delta\phi$) of the two states results in constructive or destructive interference when the states "meet" again after the second crossing. b: Population of the two states as a function of time, determined by integrating the Schrödinger equation (see text) for an unipolar pulse amplitude of 35 V/cm.*

To validate this hypothesis the time dependent Schrödinger equation was integrated for a two level model in which the two individual levels interact:

$$i\hbar\frac{\partial\Psi(t)}{\partial t} = \mathbf{H}\Psi(t) = E\Psi(t), \text{ with: } \mathbf{H} = \begin{pmatrix} E_1(t) & \omega_{21} \\ \omega_{12} & E_2(t) \end{pmatrix}$$

, where $\boldsymbol{\omega}_{ij}$ is the coupling between level i and level j, while E_i is the (time dependent) energy of state i. The coupling can be estimated with: $\omega_{ij} = \frac{\delta_m}{n^4}$, with δ_m the absolute value of the quantum defect ($l = m$). For rubidium $\delta_2 = 0.35$, which leads to a coupling of $\sim 10^{-8}$ atomic units. In the model the two levels were the middle Stark state ($k = 0$) of $n = 51$, t, and the reddest Stark state ($k = -n + 1$) of $n = 52$, which have an avoided crossing at $\sim$ 9 V/cm. A Gaussian pulse shape of 9 ns duration (FWHM) was used to describe the time dependence of the electric field. The energy dependence of the states as a function of time is depicted in Fig. 5.6a for the two states for an unipolar pulse amplitude of 35 V/cm. At t=0 the high energy state is populated and we calculate the population distribution of the two states after applying the unipolar pulse (see Fig. 5.6b). In Fig. 5.7a the population distribution as a function of the amplitude is plotted. Clear oscillations are retrieved revealing that the experimentally observed modulations could be due to interference in the Stark map. It should be noted that the two-level model is an over simplification of the experiment, since far more Stark states are involved.

The second model is based on the Landau-Zener theory (see also Chapter 2) and accounts for all the Stark levels from $n = 40$ to $n = 60$ in the Stark map. First we create a "Landau-Zener grid" determined by the energy dependence of Stark levels of several n-manifolds with respect to electric field (see Fig. 5.1). At t=0, we start out with populating

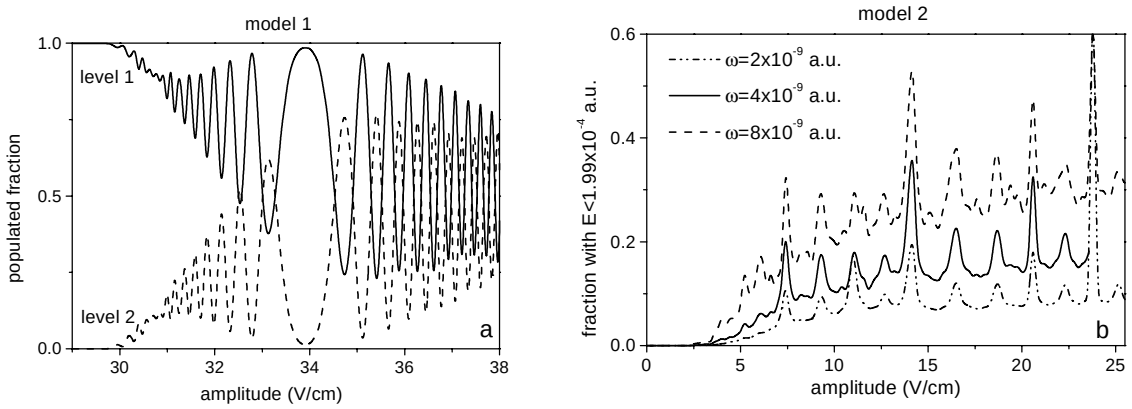

Figure 5.7: *Results of the two models discussed in the text to explain the oscillations in Fig. 5.4. a: calculated state distribution of a two level system in a time varying electric field, using the Schrödinger equation. b: Calculated fraction of the initial population which ends up below an energy of* -1.99×10^{-4} *a.u., using the Landau-Zener approximation, for three different values of the coupling strength* ω*.*

one specific state ($n = 51$, and $k = -5 \rightarrow E = -1.94 \times 10^{-4}$ a.u.) in an electric field of 27 V/cm. When the field is varied, level crossings between Stark states will occur. We define P_1 and P_2 to be the populations in state 1 and 2 respectively before a crossing and $\overline{P}_1$ and $\overline{P}_2$ the populations after a crossing. We will use A to be the probability state 1 evolves adiabatically into state 2 after the crossing, and D the probability that state 1 evolves diabatically into state 1 after the crossing. Thus after the crossing the populations are:

$$\overline{P}_1 = D \cdot P_1 + A \cdot P_2 \text{ and } \overline{P}_2 = A \cdot P_1 + D \cdot P_2.$$

The probability for state 2 to evolve in state 1 is A, and for state 2 to evolve in state 2 is $D = 1 - A$. The probability for a diabatic crossing is determined by the Landau-Zener approximation:

$$D = \exp(-2\pi \left|\omega_{12}\right|^2 / \left|\frac{dE_1}{dt} - \frac{dE_2}{dt}\right|)$$

with $\frac{dE_i}{dt}$ the derivative of the Stark energy to time: $\frac{dE_i}{dt} = \frac{dE_{n,k}}{dt} = \frac{3}{2}nk\frac{dF}{dt}$.

Such a calculation is performed for several amplitudes of the unipolar pulse. After each calculation the population with an energy less than $E = -1.99 \times 10^{-4}$ a.u. (thus more deeply bound than the initial state) is determined. In Fig. 5.7b the determined population (with $E < 1.99 \times 10^{-4}$ a.u.) is plotted as a function of the amplitude for an unipolar pulse of 9 ns (FWHM). Again a modulated signal is retrieved, but this time not due to interference effects of the Stark states. Instead the modulation occurs due to different pathways in the Stark map for different amplitudes of the unipolar pulse.

5.6 Critical Slew Rate

We have shown that a fast field kick drives a substantial part of the population, initially above the saddlepoint and free to ionize, back into bound states. Especially in the case of perpendicular polarization we achieved efficient "recombination" probabilities. The lifetimes of states in the field induced continuum that were excited with light polarized perpendicular to the electric field are on the order of tens of nanoseconds while the times were shorter for parallel polarization, although still in the nanosecond regime.

In terms of Landau-Zener crossing (see also Chapter 2) the observed effects can only be understood if we follow path B in Fig. 5.1. This means that we are performing experiments in the diabatic regime, implying that the slew rate ($\frac{\Delta F}{\Delta t}$) of our unipolar pulses is greater than the critical slew rate for a diabatic passage from a state i to a state j. This critical slew rate (S_{crit}) can be calculated with the help of the following formula [2]:

$$S_{crit} = \frac{\omega_0^2}{\partial(E_i - E_j)/\partial F} \propto \frac{(n^{-4})^2}{n^2} = n^{-10} \tag{5.2}$$

where ω_0 is the size of the avoided crossing and $\partial E_i/\partial F$ is the derivative of the term energy of a certain state as a function of the field. The coupling ω_0 can be written as $\omega_0 = \frac{\delta_m}{n^4}$, where δ_m is the absolute value of the quantum defect δ_l (only taking into account the contribution from the lowest l state: $l = m$). If we introduce the factor $\frac{S}{S_{crit}}$ (where S is the slew rate of the pulses used in our experiment) we find that in our case (at $n = 55$) this factor is $\frac{S}{S_{crit}} = \frac{4}{0.1}\ (Vcm^{-1}ns^{-1}) = 40 \gg 1$, which indeed places our experiments in the diabatic regime.

We would like to stress that the PFI signal clearly shows that we induce bound states from classically free states, and that the effects seen in the experiment are not due to lifetime enhancement of classically free states. However we did observe that with amplitudes lower than 25 V/cm we were not able to induce bound states. Apparently for those amplitudes the slew rate is below S_{crit} and no diabatic passage can be made. When we use laser radiation which is polarized parallel to the electric field, creating $m = 0$, "recombination" is strongly reduced. Still there is 10 percent of the initial population which is being "recombined" at -37 cm^{-1}, 2 cm^{-1} above the saddlepoint. The lifetime of the states photoexcited with parallel polarization is considerably shorter and thus a smaller fraction survives the 30 ns waiting time (e.g. Broers *et al.* [79]). Besides, the $m = 0$ character induces larger avoided crossings than in the case of perpendicular polarization (creating mainly $m = 2$), which also makes it harder to create bound states by Landau-Zener crossings.

5.7 Connection to Other Experiments

Let us now reconsider a microwave ionization experiment in a static electric field: if after a certain set of cycles of a single microwave pulse, a substantial part of the originally bound population is promoted to the field induced continuum, it will still not ionize due

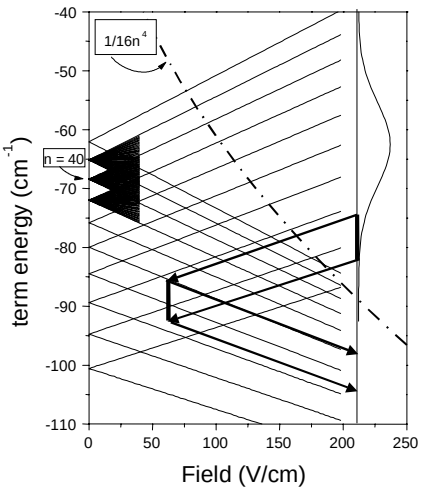

Figure 5.8: *Schematic representation of the experiment performed by Bensky et al. [78]. A broadband optical pulse is used to excite states above the saddlepoint in a static electric field of 212 V/cm. After applying a half cycle pulse of about 1.5 kV, they were able to observe bound states induced by the THz radiation. In this chapter we argue that the inevitable second half cycle, can also play a significant role, because of additional redistribution of states above the saddlepoint after the first unipolar feature, affecting the recombination signal.*

to the relatively long lifetimes involved. Therefore the Stark states still induce Landau-Zener crossings in the microwave field resulting in Above Threshold Ionization (ATI) [80] behavior. Above threshold microwave ionization experiments were already performed by Gallagher *et al.* [81,82] in the non-perturbative regime where the intensities from optical ATI experiments were scaled down to the microwave regime. Here, we suggest that even much lower intensities of microwave fields in a static electric field already suffice as an alternative way to induce ATI.

Another point worth noting is that we have seen an effect of unipolar pulses as long as 9 ns. General unipolar pulse experiments are performed in the sub-picosecond regime, where THz half-cycle pulses with an amplitude of the order of 1 kV are generated by illuminating biased semiconductor wavers with a powerful femtosecond laser pulse [83]. Bearing in mind that this half-cycle pulse propagates through vacuum, it can not be a real half cycle pulse by Maxwell's laws. It should at least have another half cycle of opposite polarity so that the pulse has zero impulse. Generally, one supposes that this second unipolar feature has a width at least an order of magnitude larger than the first and therefore a much lower amplitude, thus contributing to minor effects in the actual experiment (a detailed study of the effect of the second unipolar feature of THz pulses is presented in Chapter 3). However we have shown that unipolar pulses with relatively long widths and small amplitudes can effect excited states to a great extent.

Below we argue that such a second unipolar feature can contribute to the recombi-

nation effects observed in the experiments performed by Bensky *et al.* [78] in the THz regime. In those experiments a broadband laser pulse ($\Delta E = 10$ cm^{-1}) was used to excite states above the saddle point in a static field of about 200 V/cm. They were able to recombine 5 percent of the generated excited states with the help of a THz 5 kV half-cycle pulse delayed on the order of picoseconds relative to the photoionizing laser pulse. Graphically the excitation scheme is depicted in Fig. 5.8. After the first fast unipolar feature redistribution has occurred of the excited states. Part of these redistributed states will be very close to the saddle-point with positive energy. The fraction of the redistributed population just above the saddle-point will depend on the energy transfer of the wavepacket created by the first fast unipolar feature and thus by the exact timing of the delay of the "half-cycle" pulse. These states will not contribute to the recombination signal for perfect unipolar half-cycle pulses. Based on the experiments presented in this chapter we believe that this small portion of the population in the continuum can become bound by the slower second unipolar feature of the THz radiation. In other words, due to the second slower unipolar feature there is some probability that these states will be redistributed to negative energy, so that it does contribute to the bound state signal. Consider for instance redistributed states (after the first fast unipolar feature) in the vicinity of: $\varepsilon = 2E/E_c$= -1.68 (scaled energy, see Fig. 5.8), which corresponds in our experiment to a term energy of -32.7 cm^{-1}. We estimate the duration (30 ps) and amplitude (150 V/cm) of the second unipolar feature in the experiments of Bensky *et al.* by requiring that the total impulse should be zero, and that the duration of the "slowest" second unipolar feature is restricted by the plate separation over which the static electric field is applied. The fraction $\frac{S}{S_{crit}}$ (at $n = 35$) is now $\frac{5000}{1}$ $(Vcm^{-1}ns^{-1}) = 5000$, and therefore their second unipolar feature mainly induces diabatic behavior, just as in our experiments. One can scale the duration of the second feature in the pulse of the experiments of Bensky *et al.* to our n states as follows: $\frac{\Delta F}{\Delta t}$ scales as n^{-10}, while ΔF scales as n^{-4}, therefore Δt scales as n^6. This means that a pulse of 30 ps duration at $n = 35$ would correspond to a pulse of 0.5 ns at $n = 55$, which is in fact not far off from our conditions. Further experiments are required to determine the role of the slow feature in this type of recombination experiments.

In summary, we have observed "recombination" of Stark atoms by unipolar field pulses. Lifetimes in the order of nanoseconds have been measured implying that Landau-Zener transitions in the field induced continuum are possible in a microwave field, giving rise to ATI. Oscillations were observed when the amount of "recombined" population was (experimentally) recorded as a function of the unipolar pulse amplitude. Two models are presented which give a possible explanation for the observed oscillations. A suggestion is made on the contributions of non-unipolar features on half-cycle THz recombination experiments.

Chapter 6

Pulsed Field Recombination

We present a novel approach to the preparation of neutral (anti-)matter. The scheme is based on recombination of a free electron and an ion, and can be considered as the time inverse of pulsed field ionization. We have obtained promising results on rubidium: at low densities already efficiencies of 0.3 % were obtained. This is orders of magnitude more than has been achieved in previous recombination studies.

6.1 A Novel Recombination Scheme

The recombination of an anti-proton with a positron is one of the hurdles in the process of making neutral anti-hydrogen atoms. Existing recombination schemes for the formation of neutral atoms such as dielectronic recombination [20, 84–88] and dissociative recombination [89] cannot be used due to the absence of internal structure of the (anti-)proton. Recombination of a proton and an electron to form an atom is only possible when a third body takes away the excess energy of the captured electron (see also Chapter 1). This third body can be a spectator, in which case this mechanism is known as three body recombination (TBR) [11, 20]. In order to achieve sizeable recombination rates TBR is studied in high density plasmas at low temperatures ($\sim$4 K) [11]. When this third body is a photon, this mechanism is known as radiative recombination (RR) [15]. RR can be stimulated by a laser-field (Stimulated Radiative Recombination, SRR [16–18]) and becomes more efficient for lower laser frequencies (scaling as ν^{-3}) and temperature of the plasma's. Another recombination scheme, that relies on charge exchange with positronium was suggested by E.A. Hessels *et al.* [90]. They predict a high recombination rate but so far this scheme is not realized in practice.

In this Chapter we present a third and efficient mechanism for the recombination of free electrons with free ions, using pulsed electric fields ($\nu \sim 0.1$ GHz). The scheme is schematically sketched in the upper panel of Fig. 6.1. An ion is situated in a static electric field. The static electric field modifies the Coulomb potential such that a saddle point is created (Fig. 6.1a). If an electron passes over the saddle point in the modified Coulomb potential, it will take a small, but not negligible, amount of time to return to the saddle point and escape from the ion (Fig. 6.1a). If the static field is turned off (Fig. 6.1b) before

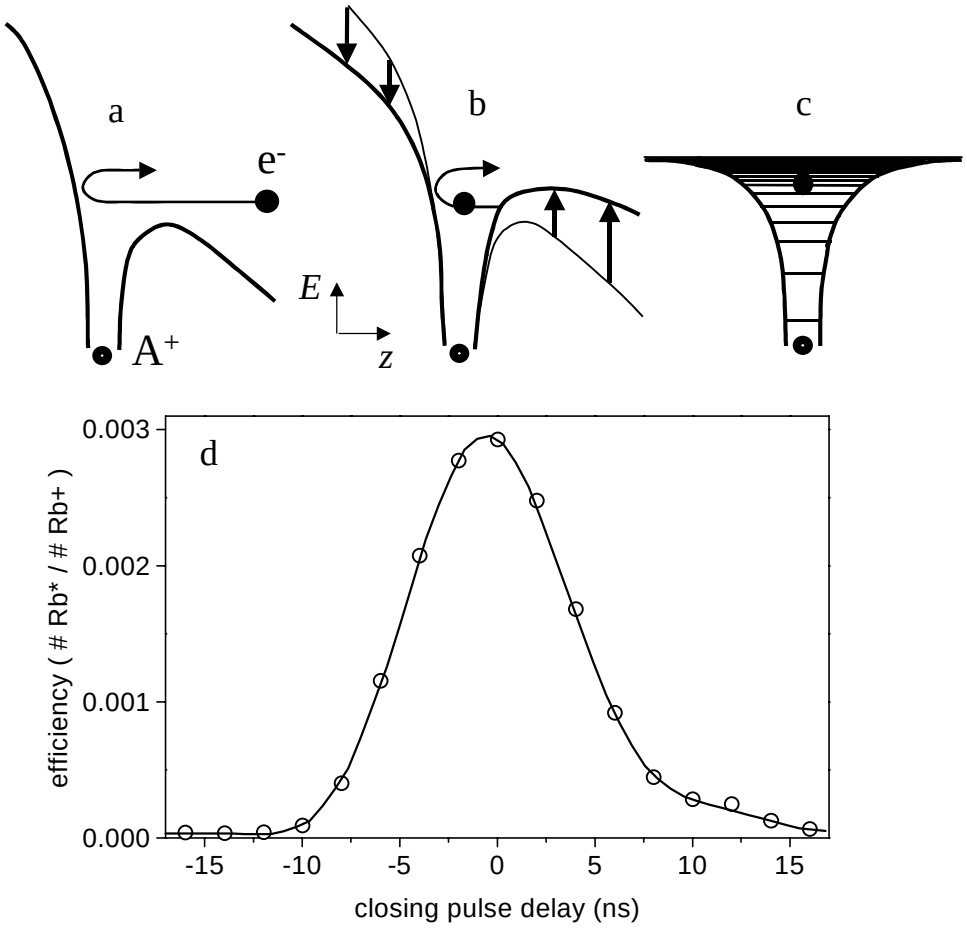

Figure 6.1: *Schematic representation of the Pulsed Field Recombination scheme: (a): An ion awaits in a static electric field an electron, which is decelerated and has its turning point at the ion. (b): When the electron is at the turning point, the electric field is quickly turned off. (c): If the field is turned off during the turning of the electron, a bound state is formed. (d): Experimentally observed efficiency (number of recombined atoms divided by the number of free Rb ions) as a function of the delay (τ) of the quick turnoff (1.5 V/cm to 0.2 V/cm in 1.0 ns).*

the electron returns to the saddle point, it will remain bound in a highly excited state (Fig. 6.1c). In the experiments reported in this chapter the electrons start out with a kinetic energy of 0.75 eV and are decelerated by a static electric field of 1.5 V/cm, such that the electrons have their turning at the position of a rubidium ion source. The time required for the electron to travel from the saddle point, to the rubidium nucleus, and back to the saddle point is roughly 1 ns for the fields and energies used in this experiment. In Fig. 6.1d the experimentally determined efficiency (number of recombined rubidium atoms divided by the number of free rubidium ions) of this scheme is depicted as a function of the delay of the fast field turn off. This delay is with respect to the time when the free electron has its turning point in the electric field. Clearly, a maximum number of recombination events is recorded at zero delay. Note that efficiencies up to 3.0×10^{-3} are obtained.

We will show that this scheme of Pulsed Field Recombination (PFR) can work for any atom. PFR does not rely on core-scattering, arising from quantum defects of non-hydrogenic atoms [2]. As we show later, the PFR scheme produces an atom in a Rydberg state, a state with a high principal quantum number ($n \approx 200$) [2]. PFR can be viewed as the inverse process of Pulsed Field Ionization [2,35] (discussed in Chapter 2), in which a pulsed electric field ionizes a Rydberg state. The latter process is used in atomic physics to determine the principal quantum number of a Rydberg state [30], and in physical chemistry it forms the basis of ZEKE-spectroscopy [37, 38], determining the photoionization potential and vibrational structure of large molecules.

6.2 Experimental Realization

The PFR scheme was experimentally realized as follows: a pulsed electron source [91] was created by photoionizing lithium atoms in a static electric field of 1.50 V/cm, with a pulsed (9 ns duration) narrowband ($\Delta\lambda <$ 0.2 cm^{-1}) dye laser (operating at 30 Hz). Typically electron pulses of 9 ns duration, with about $(5 \pm 2) \times 10^4$ electrons in a volume of 0.02 mm^3 were produced. The electric field is created by two parallel capacitor plates (separation: 10.0 mm) over which a voltage is applied (Fig. 6.2a). The ionizing laser pulse is focussed to a diameter of 50 μm to minimize the energy spread of the created electron pulses. After ionization, the free electrons are pushed towards the anode plate (connected to ground) through which a small hole is drilled, covered by a grid. After passing through the anode, the electrons enter a field-free region of 15.0 mm, after which another set of parallel capacitor plates (with small holes, covered by a grid) is situated. Since the final plate is on -1.50 V the electrons turn around halfway between these plates, separated by 10.0 mm. In this region a cloud of rubidium ions is awaiting the electrons. To minimize the spread of the electrons during their travel towards the ions in directions perpendicular to the direction of propagation, a magnetic field was implemented, parallel to the direction of propagation (B_z = 2.5 mT). Typically $(5 \pm 2) \times 10^3$ Rb ions were produced in a volume of 2.0 mm^3. The ions were produced by photoionizing rubidium atoms in a static electric field of 1.50 V/cm, 50 ns before the lithium atoms were ionized,

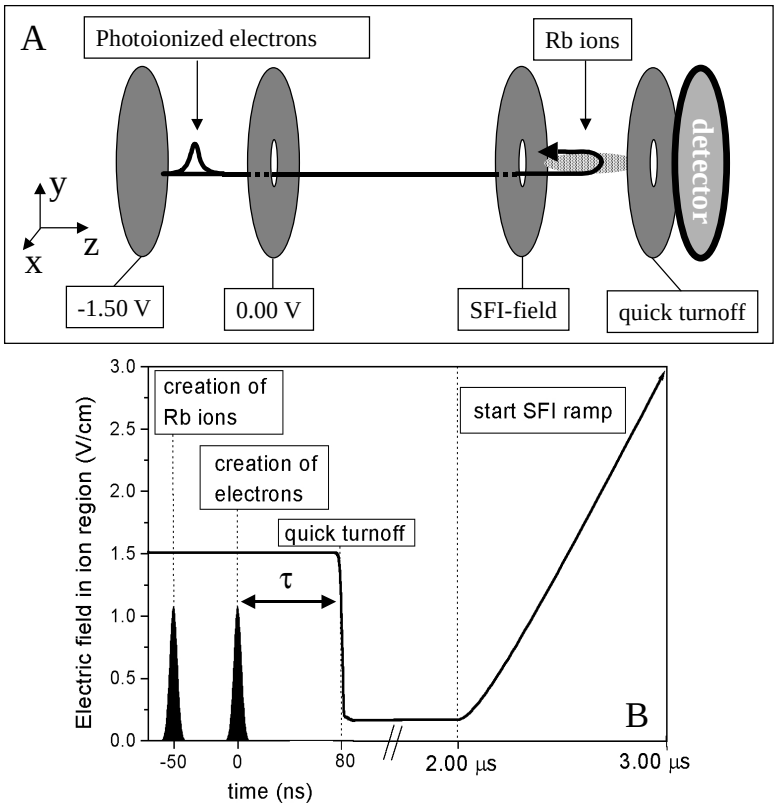

Figure 6.2: *a: Experimental setup. A static electric field of 1.50 V/cm pushes electrons towards the rubidium ion region, where the ions await the electrons in an opposite electric field. The cathode plate is connected to a fast pulse generator so the field can be turned of within 0.4 ns to 9 ns. The anode plate is connected to a slow pulse generator for SFI detection. b: Timing scheme of the experiment. The graph shows the electric field as a function of time in the ion region and when the electrons and ions were created by photoionization.*

in a two-photon process. The frequency doubled output of a Nd:YAG laser was used for this two-photon process (2x532 nm), resulting in ionized electrons with an initial velocity of 4×10^5 m/s. Therefore, all the electrons originating from ionized rubidium atoms have left this interaction region at the time the lithium photoelectrons are created. Note that the heavy rubidium ions are virtually standing still during our experiment ($\Delta l = 1$ μm in 100 ns). The shape of the ion cloud is $\sim$6 mm in the z- and x-direction, and 60 μm in the y-direction. In the ion source region the electrons are decelerated by the electric field of 1.50 V/cm, and have their turning point at the position of the ion cloud. At that time the field is turned off by dipping the voltage on the cathode plate from -1.50 V to -0.20 V. The electric field turn off is realized by connecting an impedance matched, fast pulse generator to the cathode plate. Different pulse generators were used to study the effect of different fall times of the electric field (90% $\rightarrow$ 10% in 0.4 ns, 1.0 ns, 9.0 ns respectively).

The number of Rb ions is kept low with respect to the number of free electrons to prevent the effect of "trapping" the electrons in the attractive potential of the ions. For 5×10^3 ions in a sphere with a volume of 2.0 mm^3, the electrons feel an attractive field of 110 mV/cm at the edge of this sphere. Such a low density plasma is therefore not stable when the ion region is biased after the quick turn off to an electric field of 200 mV/cm. The experiments were performed in a vacuum chamber with a background pressure of 5×10^{-7} Torr.

6.3 Experimental Results and Classical Description

Most recombination processes are characterized by cross-sections. In our PFR scheme it is more appropriate to give the volume in which the electron has to be at the moment of the quick turn off to recombine with the ion. We define the interaction volume V_{int} as the volume of space for which an electron with an initial velocity (0,0,v$_z$) will recombine with the ion after the electric field is ramped down to 200 mV/cm; it is not necessary to use a distribution in velocity due to the very low effective temperature of the electron source. This interaction volume can be estimated with the following formula:

$$N(\tau) = \rho_{ion}\rho_e V_{over} V_{int} \tag{6.1}$$

where $N(\tau)$ is the number of recombinations at a certain delay (τ) of the quick turn off, ρ_{ion} is the ion density, ρ_e is the electron density, V_{over} is the macroscopic overlap volume of the electron- and ion cloud, and $V_{int} = \int_{-\infty}^{\infty} f(t'-\tau)v_{int}(t')dt'$, where $f(t) = \sqrt{\frac{4\ln 2}{\pi\alpha^2}}\exp(\frac{-t^2 4\ln 2}{\alpha^2})$ is a function which describes the time profile of the electron pulses (α is the duration of the electron pulses: 9 ns). Typically to have 15 recombination events per 5×10^4 electrons in an overlap volume of 0.02 mm^3 and an ion density of 2.5×10^6 cm^{-3} (these numbers were experimentally realized) this observed interaction volume is $(1.2 \pm 1.0) \times 10^{-10}$ cm^3. A theoretical estimate of V_{int} is obtained by classically solving Newton's equations, with a force equal to: $\mathbf{F}(t) = q(\mathbf{E}(t) + \mathbf{v}(t) \times \mathbf{B}/c)$. The electric field ($\mathbf{E}$) is the superposition of the Coulomb potential of the ions and external field, $\mathbf{v}$ is the velocity of the electrons and $\mathbf{B}$ is the magnetic field. An interaction volume of 0.25×10^{-10}cm^3 is found for a 9 ns electron pulse, which agrees very well with the estimated value from the experimental data. We note that the spatial extent of such an interaction volume corresponds to Rydberg states around $n \approx 200$. A more detailed description of the interaction volume is presented in Chapter 7. Note that the radius of the interaction volume is two orders of magnitude smaller than the average distance between neighboring ions, which means perturbations from unrecombined Rb^+ ions are not important for this experiment.

A detailed picture of the state distribution of the pulsed field recombined Rydberg atoms was obtained by Selective Field Ionization [2] (SFI, see Chapter 2). In short, this technique makes use of the fact that Rydberg states of an atom can be ionized if a strong enough electric field is applied. The relation between the value of the electric field at

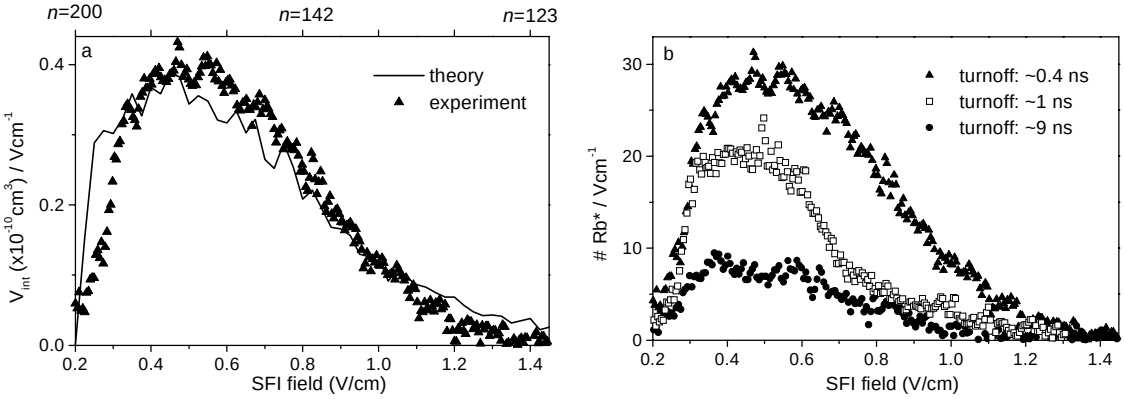

Figure 6.3: *a: Calculated state distribution of the recombined Rydberg atoms compared with the experimental state distribution. The experimentally determined interaction volume ((1.0±0.7)x10^{-10} cm^3) is varied within its error to optimize the comparison with theory (V_{int} = 0.3x10^{-10} cm^3). b: Recorded state distribution by the Selective Field Ionization (SFI) detection scheme. The three curves show the state distribution for different turnoff times.*

which field ionization classically occurs and the principal quantum number n of a state is (in atomic units): $F = (\frac{E}{2})^2 = \frac{1}{16n^4}$. If the electric field is ramped in time and the field at which Rydberg atoms decay is monitored, the populated Rydberg states can be approximately deduced. To calculate the SFI spectrum, we propagated Newton's equation with the experimental ramp rate. In our experiment we use a field ramp of 2.00 V/cm in 1.80 μs, 2 μs after the fast field turn off (Fig. 6.2b). The field ramp pushes the field ionized electrons towards the cathode plate through which a hole was drilled and covered with a grid. The electrons are recorded by a set of Micro-Sphere-Plates (MSP's). In this way we record at which times, and hence at what field strengths, electrons are being field ionized. During the two microseconds after the quick turn off and before the SFI ramp, effects of TBR and RR are ruled out since the rates of these processes are far too low at our densities (rate ~ 1 s^{-1}). Moreover we checked for different delays of the SFI field what the total amount of recombinations was and this value did not have the tendency to increase for longer delays.

In Fig. 6.3a the SFI state distribution of the 0.4 ns turn off is compared with theory. Note the excellent agreement between experiment and theory. Only at higher SFI fields (lower n) there is a small discrepancy between experiment and theory. This could be due to a slight difference in shape of the quick turn off used in the calculation and in the experiment. The shape of these traces show that recombination to very highly excited states is most efficient. From the calculations an average principal quantum number can be retrieved: $< n >= 170$, with $\Delta n = \sqrt{< n^2 > - < n >^2} = 23$. This agrees with the estimated interaction volume, which predicted recombined states in the order of $n = 200$. Calculations with and without core scattering showed no qualitative and quantitative

difference in the recombined state distribution indicating that the non-hydrogenic Rb^+ core plays no role in the capture step.

The PFR dynamics was probed even further, by measuring the Rydberg state distribution for different turnoff times of the electric field from -1.50 V/cm to -0.20 V/cm at zero delay (Fig. 6.1d). In Fig. 6.3b three state distributions are depicted for different electric field turnoff times (averaged over 1000 laser shots). At the fastest field ramp used, not only more electrons are recombined, but also the captured state distribution extends to more deeply bound states. This can be explained by the fact that PFR relies on turning off the field before the electron can return to the saddle point. The change in energy of the electron from the ramp down of the field is $\Delta E = -e\int_{-\infty}^{\infty}(\frac{dF}{dt})z(t)dt$ where $z(t)$ is the time dependent z-coordinate of the electron. The time derivative of the field is a purely negative function. If $\frac{dF}{dt}$ is sharp, then there will be some trajectories for which z(t) is purely negative over the whole width of $\frac{dF}{dt}$. If $\frac{dF}{dt}$ is broad, $z(t)$ will go from positive, to negative, and back to positive over the width of $\frac{dF}{dt}$. Thus, the fast ramp downs (sharp $\frac{dF}{dt}$) give larger energy losses than the slow ramp downs (broad $\frac{dF}{dt}$). Moreover, the electron pulses in the PFR experiment are $\sim$9 ns long. Faster turnoffs use a smaller fraction of the electron pulses for recombination, resulting in a mismatch of the electron pulse duration and the duration of the fast field turnoff. We anticipate that making the electron pulses as short as the turnoff in time will increase the efficiency even more.

The connection of PFR can be made towards SRR in the low frequency domain. One moves from a limit where the optical period is much shorter than the time dynamics involved in the atomic system (e.g. the orbiting period of the captured electron), to a region where the field pulses have a duration on the order of the time dynamics involved in the atomic system. Therefore this novel mechanism can be best described as an intermediate between TBR and SRR, in which no plasmas are required.

6.4 Discussion and Conclusions

A potential application of this new recombination technique is the creation of atomic anti-hydrogen [11, 94, 95]. Observations of atomic anti-hydrogen are reported in Ref. [26, 92], where a low number of anti-hydrogen atoms were observed with relativistic energies. So far the most promising schemes to produce cold atomic anti-hydrogen are based on a combined trap [93], where one relies on the interaction between positrons and anti-protons at very low relative velocities and low temperature. To date, the study of these recombination schemes is done with normal matter. In Ref. [94] such a combined trap is described, where typically $>10^5$ protons and 10^6 electrons (corresponding density: 10^8 cm^{-3}) in the combined trap were detected. However, up to now no successful experiments on the formation of neutral- or anti-matter have been reported in this configuration. We foresee that the implementation of the third route of recombination, as introduced here, can in fact produce a sizeable number of recombined neutral anti-matter atoms (in a high Rydberg state) in the already realized combined trap. If the overlap volume is maximal (the anti-proton plasma takes up the same volume as the positron plasma), the positron

density is 10^{7-8} cm^{-3}, and the number of trapped anti-protons is 10^5, our scheme can produce 10^2-10^3 recombined anti-hydrogen atoms in a single experiment (assuming the same V_{int} as is observed in our measurements). The exact implementation of PFR for the experimental realization of atomic anti-hydrogen production is currently investigated, and discussed in Chapter 9.

In summary, we have observed recombination of rubidium ions with free electrons with the use of fast electric field pulses. The process can be seen as the inverse process of field ionization. Efficiencies as high as 3×10^{-3} have been achieved and a simple improvement (reducing the electron pulse duration mismatch) can raise the efficiency significantly. The observed effect can be understood with arguments which do not require mechanisms relying on the magnitude of the quantum defects of non-hydrogenic atoms, indicating that the PFR mechanism works for any atom. In fact in Chapter 7 we report on experiments where Li ions and free electrons were recombined with the PFR scheme. Moreover we propose that our scheme is a promising avenue for the formation of neutral anti-matter. Although we restricted the discussion in this chapter to the recombination of rubidium ions and electrons, the technique of PFR is in principle also applicable for the formation of neutral molecules, such as C_{60} as discussed in Chapter 8, anions [96], and ion-pair states [97].

Chapter 7

Pulsed Field Recombination with a Penning Trap

The Pulsed Field Recombination scheme is used to recombine free electrons with Li^+ ions to produce neutral Li atoms in a high Rydberg state ($n \approx 180$). The experimental conditions mimic some of the conditions under which one tries to recombine anti-protons and positrons to produce cold anti-hydrogen. In the current experiments we have trapped electrons in a Penning trap ($B \approx 35$ mT). Subsequently these electrons were recombined with spatially separated Li^+ ions. The recorded efficiency is 2.0 % versus 0.3 % in previous experiments. Several experiments were performed to study the dynamics of Pulsed Field Recombination in more detail.

7.1 The Pursuit of Anti-Hydrogen

In the previous chapter a novel and controllable recombination scheme was presented, demonstrated with rubidium ions and free electrons. The scheme was named Pulsed Field Recombination (PFR), since it can be seen as the time inverse of Pulsed Field Ionization [2,35] (see also Chapter 2). It was stated that PFR could be used to recombine any sort of atom or molecule with free electrons, with the potential application to create atomic anti-hydrogen by recombining a free positron with an anti-proton (for an overview of anti-matter see Chapter 1.6). In this Chapter new experiments are presented in which the PFR scheme is studied in more detail, and in a configuration resembling more the conditions under which recombination of positrons and anti-protons is pursued.

Recombining an anti-proton and a positron into an anti-hydrogen atom enables the first high precision comparison between neutral matter and anti-matter. The ATRAP and ATHENA collaborations at CERN have the prestigious goal to produce cold (4 K) and trapped anti-hydrogen atoms in order to compare an anti-atom with its complementary atom: the hydrogen atom. Precise comparisons are a test for the CPT theorem which states that nature is invariant under the combined operations of Charge conjugation, Parity conjugation and Time reversal [100–102]. This means that every particle state must have an anti-particle state with equal mass, spin, and lifetime, but opposite magnetic

moment, and charge. Moreover gravity experiments on neutral anti-matter can test the Weak Equivalence Principle [103,104] which states that a particle behaves the same under the influence of gravity as an anti-particle. Neutral anti-matter is required for these experiments since the smallest stray electric and magnetic fields already strongly influence charged anti-matter particles.

We report on new experiments using "ordinary" matter to study the recombination dynamics of the PFR scheme. There were four major motivations for performing these experiments. The first is that in a typical PFR experiment one uses the inertia of an ion (with respect to the small inertia of an electron) to enable an electron to approach the ion in a static electric field. One therefore might expect that a decrease in the efficiency of the PFR scheme is observed when one tries to recombine free electrons to ions with less mass (such as a proton). To test if the PFR scheme could indeed be used to recombine lighter ions with free electrons we have used lithium ions. Lithium being 12 times lighter than rubidium, resembles much more a proton, although it is still 7 times heavier. The second motivation was that the previous experiments on PFR were performed in a geometry far different from the geometry used by ATRAP at CERN, where one will study recombination of *trapped* positrons and *trapped* anti-protons in Penning traps [108–111]. In the previous experiments we produced electron pulses with a well defined kinetic energy by photoionizing Li atoms in a static electric field by means of a narrow-band dye laser, instead of starting out from trapped electrons. Thus in order to show that the PFR scheme can indeed be used in the geometry at CERN we have build an electron trap. A third motivation was to investigate what the effect is of a different total quantum defect of the recombined atoms on the recombination dynamics. It was stated [98] that PFR can be used to recombine any sort of ion with a free electron. Lithium has a total quantum defect of 0.452 ($\mu_0 = 0.4$, $\mu_1 = 0.05$, $\mu_2 = 0.002$) and rubidium a total quantum defect of 7.15 ($\mu_0 = 3.13$, $\mu_1 = 2.65$, $\mu_2 = 1.35$, $\mu_3 = 0.02$), a comparison of the previous experiments in rubidium with the current experiments in lithium could reveal a dependance of the recombination dynamics on the total value of the quantum defect. The last motivation was to increase the recombination efficiency of the PFR scheme.

We report on the detailed study of the recombination efficiency in a Penning trap configuration as a function of the temperature of the electrons in the trap and as a function of the storage time of the electrons in the trap. We also studied whether a magnetic field in the range of 10 - 60 mT changed the recombination dynamics and the effect of a small residual electric field after the recombination event. A theoretical description using semi-classical calculations is presented. These semi-classical calculations give deeper insight on the states which are being formed in the recombination process and are used to probe the recombination dynamics not measurable by experiment.

7.2 Scheme and Efficiency

In order to study PFR one needs electron pulses with a well defined controllable energy, free ions with little kinetic energy, and the ability to quickly turn off the electric field in

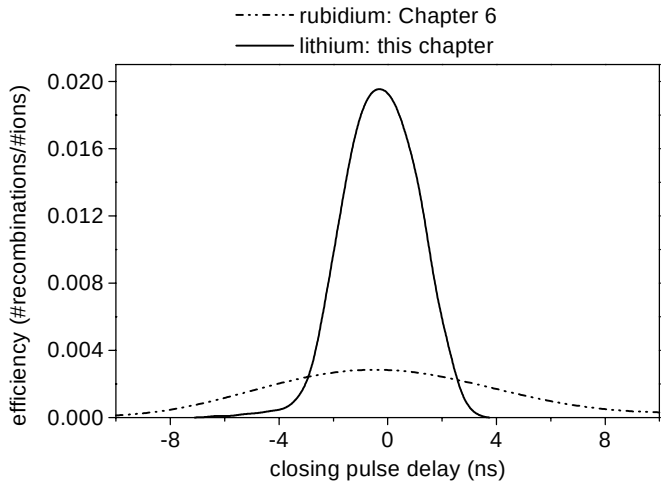

Figure 7.1: *Experimentally observed efficiency (number of recombined atoms divided by the number of free ions) as a function of the delay of the quick turnoff. The solid line represents data taken where we studied recombination of free electrons and lithium ions with the use of an electron trap. The dashed line represents data from previous work [98] (Chapter 6) where we studied recombination of free electrons and rubidium ions in a trapless geometry.*

which the ions are situated. The electron trap configuration allowed us to produce ∼4 ns electron pulses. This was achieved by filling the electron trap with electrons and then quickly opening the trap, resulting in a electron pulse. In the current experiments the electrons leaving the trap have a kinetic energy of 1.5 eV and are decelerated by a static electric field of 3.0 V/cm, such that the electrons have their turning at the position of a lithium ion cloud. The time required for the electron to travel from the saddle point, to the lithium nucleus, and back to the saddle point is about 1 ns for the fields and energies used in this experiment. This time is comparable to the turn off time of the static electric field (90% → 10% in 0.8 ns).

In Fig. 7.1 the experimentally determined efficiency (number of recombined atoms divided by the number of free ions) of this scheme is depicted as a function of the delay of the fast field turn off. This delay is with respect to the time when the free electron has its turning point in the electric field. Clearly, a maximum number of recombination events is recorded at zero delay. A comparison with the previous experiments with rubidium ions shows clearly that the efficiency (3.0×10^{-3}, Chapter 6 [98]) has gone up by almost an order of magnitude (2.0×10^{-2}) and that the electron pulses are much shorter. The increase in efficiency is mainly due to the fact that the electron pulses are shorter in time (from 11 ns [98] to 3.8 ns) and that we had better control over the overlap volume of the ion cloud and the volume of the electron pulses. We achieved the highest efficiency (6%) so far when we used the PFR scheme to recombine a free electron with a free ionic carbon cluster in a trapless environment [99]. Note that Fig. 7.1 shows that PFR can be used in

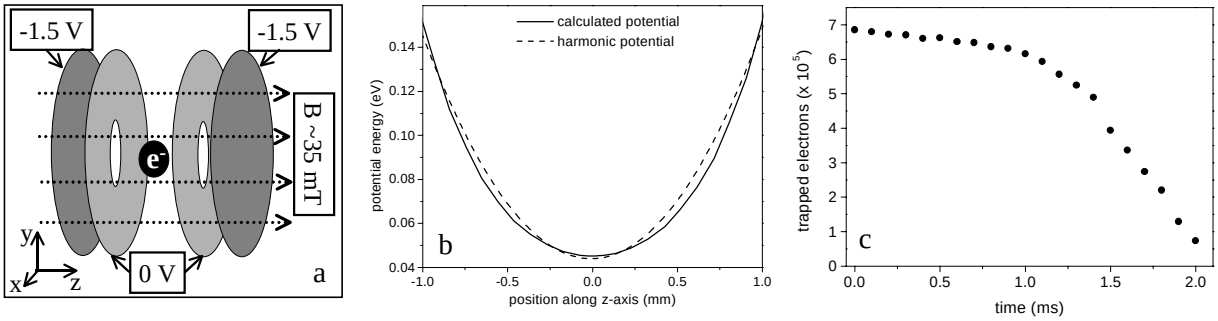

Figure 7.2: *a: Schematic representation of the Penning trap, consisting of two flat capacitor plates and two ring electrodes. The lifetime of this trap was measured to be 1.5 ms at a background pressure of $\pm 10^{-6}$ Torr. b: Solid line: a calculation of the on-axis potential inside the Penning trap using SIMION, showing the harmonicity of the potential (dotted line: harmonic potential). c: The number of trapped electrons as a function of the storage time. The lifetime was mainly affected by the background pressure. The minimum required magnetic field was 12 mT and increasing the magnetic field beyond this value hardly affected the lifetime of the trap.*

geometry of trapped electrons and light ions.

7.3 Experimental Realization

Our Penning trap consists of two stainless steel parallel capacitor plates (thickness 1.0 mm) of 30.0 mm in diameter and two stainless steel ring electrodes (thickness 0.5 mm) with an outer diameter of 30.0 mm and an inner diameter of 4.0 mm (Fig. 7.2a). The two parallel capacitor plates (electrode 1 and 4) are separated by 5.0 mm, and a hole of 10.0 mm was drilled through them covered by a grid, so that electrons could pass through these plates, but the plates still behave as flat capacitor plates. The two ring electrodes were placed in between the parallel capacitor plates (electrode 2 and 3). The ring electrodes are separated from each other by 2.0 mm and each ring electrode was separated by 1.0 mm from the closest flat capacitor plate. A potential well was created in the z-direction for electrons if one biased the two parallel capacitor plates with a negative voltage and if one biased the ring electrodes with a higher voltage. In these experiments the parallel capacitor plates were biased by a voltage of -1.5 V and the ring electrodes were biased in the range of 0.0 to -0.40 V. The minimum of the potential well was right in between the two ring electrodes, as shown by the SIMION potential calculation in Fig. 7.2b. However the electrons would still be able to escape the trap in the x-y-direction. To prevent the electrons from escaping the trap in the x-y-direction, a magnetic field of several tens of mT in the z-direction was used. We have used SIMION [139] to calculate the shape of the potential well on the z-axis in order to design a plate configuration which produces

as much as possible a harmonic potential in order to mimic the conditions of the ATRAP setup at CERN.

We filled the electron trap by photo-ionizing gas-phase lithium atoms. A jet of these alkali atoms comes from a resistively heated oven. The lithium atoms were ionized by means of two synchronized dye lasers pumped by the second harmonic of a Nd:YAG laser (532 nm), which produced laser pulses of about 7 ns duration with a repetition rate of 10 Hz. The first dye laser was used to excite the 2s electron to the $2p_{1/2-3/2}$ state in lithium (670.97 nm, 150 μJ) and the second dye laser (tunable from $340 - 350$ nm, 1.8 mJ per pulse) was used to drive the transition from the 2p state into the continuum. By connecting a fast pulse generator on parallel capacitor plate 4 (Fig. 7.3a) the voltage could be switched from -1.5 V to +1.0 V within 800 ps on this plate. This enabled us to empty the trap at any time, and record the electrons on a (micro sphere plate) detector. Care was taken for correct impedance matching. In this way the time dependance of the number of electrons at any time after the filling of the trap could be measured in a destructive way (Fig. 7.2c). We were able to fill the trap with about $7(\pm 2)\text{x}10^5$ electrons and the recorded lifetime was about 1.5 ms determined by the background pressure ($\pm 10^{-6}$ Torr) in the vacuum chamber.

At 10.0 mm from the Penning trap plate configuration another ring electrode was placed (electrode 5, outer diameter 30.0 mm, inner diameter 10.0 mm), which was used as the central electrode of an Einzel lens configuration. 10.0 mm behind the Einzel lens two parallel capacitor plates (electrodes 6 and 7) were situated separated by 5.0 mm. A hole of 10.0 mm was drilled through these parallel capacitor plates covered by a grid to minimize distortions on the electric field in between these parallel capacitor plates. In between these parallel capacitor plates an homogeneous electric field was created of 3.0 V/cm. The first plate was connected to a ramp generator (Avtech, AV-1000-C) which could bias the plate from -5.0 to +5.0 V and ramp the voltage at a well defined time from the bias voltage to +10 or -10 V, with a controllable slew rate (10% - 90% in 5 ns to 1 ms). This voltage ramp was required to perform Selective Field Ionization (SFI [2,50]) in order to measure how many recombined atoms were created and in which Rydberg state (discussed below). The last plate (electrode 7) was connected to a fast pulse generator (SRS DG535) ramping the voltage down from -1.5 V to any voltage in between -1.5 V and + 1.0 V within 0.8 ns. Again care was taken to match the impedance of the parallel capacitor plate to the output of the fast pulse generator. The complete plate configuration (Fig. 7.3a) was placed in the heart of 2 coils (outer diameter 12.5 cm) in the Helmholtz configuration producing a tunable magnetic field of 0.0-64.0 mT. This setup enabled us to first trap electrons (Fig. 7.3b), then pulse the trap open so that the electrons acquired a well defined kinetic energy and travel towards the Einzel lens (Fig. 7.3c), guide the electrons towards the two parallel capacitor plates so that they would pass through the grid in the cathode plate of the two parallel capacitor plates, and finally slow down the electrons by the static electric field such that they would turn around halfway in between these parallel capacitor plates ± 80 ns after the trap was pulsed open (Fig. 7.3d). During the turning of the electrons around the ion cloud, the voltage on the last capacitor plate is quickly decreased from -1.5 V to typically +0.1 V to recombine the electrons with the

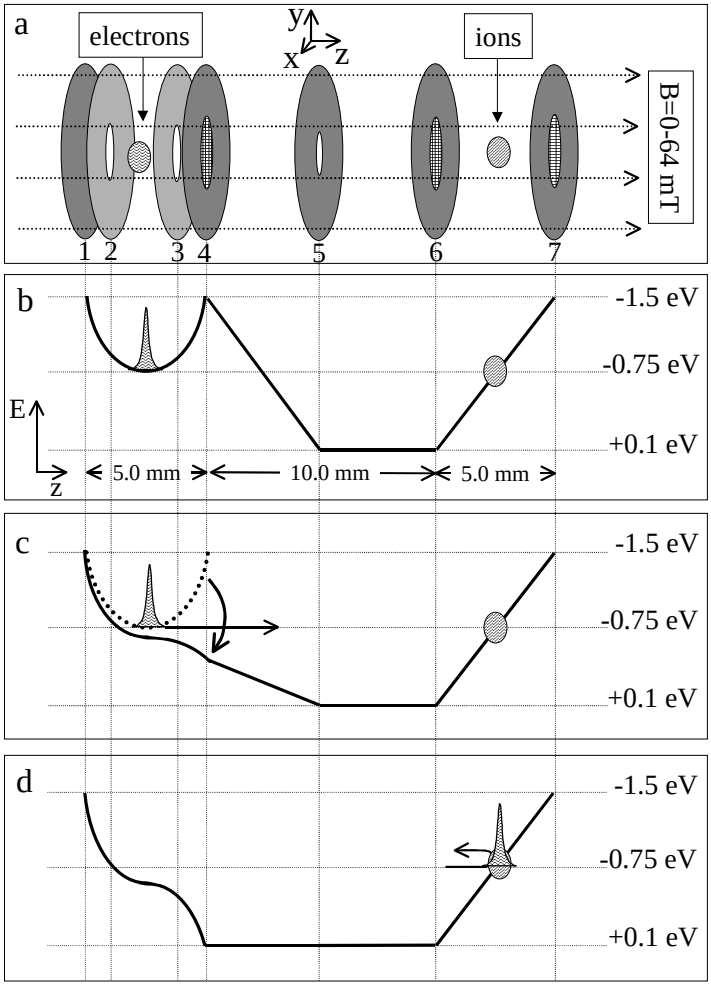

Figure 7.3: *a: Experimental configuration. Two (Micro Sphere Plate) detectors were used to record either electrons or ions. One detector was placed on the left of plate 1 to measure the number of trapped electrons in a destructive way. The other was placed on the right of plate 7 to measure how much ions were created before the recombination event and to measure electrons created from our recombined atom detection scheme. The first four plates on the left hand side form the Penning trap. Note that grids are used to enable electrons to travel from one region to the other. The fifth plate is used as an Einzel lens. In between plate 6 and 7 ions are awaiting the electrons in a homogeneous electric field which could be quickly turned off by switching the voltage on plate 7. Plate 6 was connected to a ramp generator in order to perform Selective Field ionization of the recombined atoms. b-d: Schematic representation of the creation of electron pulses from the trap and their flight towards the ions.*

free ions by means of the PFR scheme. A small static electric field is left over in this region of 200 mV/cm to ensure that any unrecombined free electron is accelerated out of this region and to prevent the effect of "trapping" the electrons in the attractive potential of the ion cloud. For the volumes and densities used in the experiments, the electrons feel an attractive field of <10 mV/cm at the edge of these volumes. Such a low density plasma is not stable when the ion region is biased with an electric field of 200 mV/cm.

In between the parallel capacitor plates a second atomic beam of lithium atoms was directed by means of a resistively heated oven. Lithium ions were ionized either by using the same lasers to produce the electron pulses and aligning the beams on the second atomic beam (scheme I: used for experiments where the electrons were stored in the Penning trap for times shorter then 500 ns) or by using a third dye laser (scheme II: used for experiments where we studied the recombination efficiency as a function of storage time of the electrons in the trap) pumped by the second harmonic of a Nd:YAG laser, synchronized to the other two dye lasers. This laser produced 548.4 nm laser pulses with an energy of ±10 mJ. The light was then frequency doubled in a KDP crystal and resulted in a collinear beam of 548.4 nm (±9 mJ) and 274.2 nm (± 700 μJ). This collinear beam excited the 4p state in lithium by means of the 274.2 nm light and then ionized lithium atoms by driving the transition from this 4p state into the continuum. All the laser beams were created such that their diameter was 2 mm. Typically we would produce a cylindrically shaped ion cloud containing ∼5000 ions, with a diameter of 2 mm and a length of 10 mm ($\rho_{ion} \approx 1.6 \times 10^5$ ions/cm^3).

7.4 Experimental Results

Timing is essential in a PFR experiment. This can be seen in Fig. 7.1: if we turn off the static electric field before the electrons reach the ions halfway between the parallel capacitor plates, the electrons will hardly be slowed down and will pass the ions without being recombined. If we turn off the static electric field too late the electrons will turn around at the ions but will gain kinetic energy again due to the static electric field and will leave the ion region in the opposite direction without being recombined. If we turn off the static electric field at the moment the electrons turn we record a maximum recombination efficiency of 2.0 %. From Fig. 7.1 we also retrieve the time profile from the electrons since we record a Guassian profile with a width of 3.8 ns which means that we have created electron pulses of 3.8 ns. The electron pulses are produced by pulsing open the electron trap in 0.8 ns and therefore one can expect that electron pulses are created of 0.8 ns. The fact that the pulse duration is 6 times longer is mainly due to Coulomb repulsion which results in an enlargement of the electron cloud. The enlargement of the electron cloud is mainly restricted in the z-direction since the presence of the magnetic field prevents the cloud from blowing up in directions perpendicular to the z-axis. This, in turn, will result in different travelling times towards the ions and therefore a broadening of the time duration of the electron pulses. Note that the time duration of the electron pulses is much shorter than in the previous experiments where the electron pulse duration was limited

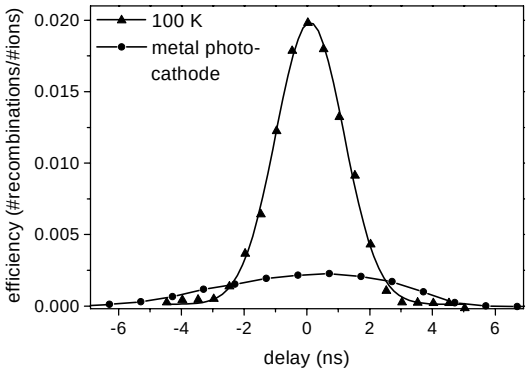

Figure 7.4: *The recombination efficiency as a function of the delay of the quick turnoff. The triangles represent data where we filled the trap with electrons with a well-defined transverse kinetic energy. The circles represent data where we filled the trap with hot electrons with a very ill-defined kinetic energy (see text).*

by the duration of the photoionizing laser pulses ($\sim$ 10 ns).

In order to study the effect of the temperature of the trapped electrons in the trap on the recombination dynamics we have used scheme I to produce the ionic cloud containing $5(\pm1) \times 10^2$ ions in a volume of 7.9×10^{-3} cm^3. The ion cloud was produced in a static electric field of 3.0 V/cm, 2 ns after the electron trap was filled. We filled the electron trap by ionizing the lithium atoms 74 cm^{-1} above the ionization limit resulting in $7(\pm2) \times 10^5$ trapped electrons with a kinetic energy of 0.9 meV ($\sim$ 100 K). At the instant the electron trap is filled, this kinetic energy results mainly in motion along the z-direction since the polarization of the ionizing laser is along the electric field and thus electrons will mainly be emitted along the z-axis. The bandwidth of the ionizing laser was less than 0.2 cm^{-1} resulting in an additional energy spread of less than 0.3 K. However the noise generated from the pulse generators and voltage supplies connected to the electrodes cannot be neglected and will have an effect on the temperature of the electron cloud ($\sim$ 10 K). We also filled the trap by directing the 348.0 nm beam on a metal plate so that high kinetic energy ($>$ 1000 K) electrons with a large energy spread were created in random directions and $3(\pm1) \times 10^5$ electrons were trapped. Then 300 ns later the trap was pulsed open producing 1.5($\pm$0.1) eV electron pulses that travelled towards the ions to be recombined. In Fig. 7.4 the efficiency as a function of the time delay of the quick turn off is depicted for the "cold" and "hot" photocathode electrons. Clearly it is seen that the highest efficiency was obtained for lower temperatures of the trapped electrons. The fact that the efficiency increases for lower temperatures of the trapped electrons can be understood as follows. Due to the low energy spread, more electrons will have their turning point at the same time in the static electric field at the ion cloud and thus more recombined atoms are produced with the same number of ions. Moreover if the kinetic energy in directions perpendicular to the z-axis decreases, the cyclotron orbit of the electrons will decrease.

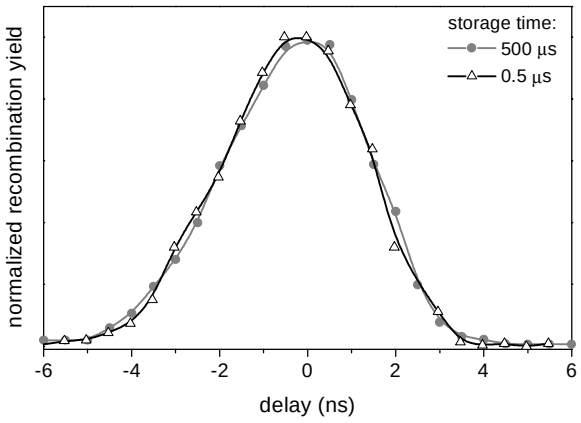

Figure 7.5: *The efficiency as a function of the delay of the quick turnoff, for different storage times of the trapped electrons. The circles show the efficiency for a storage time of 500 μs and the triangles show the efficiency for a storage time of 500 ns.*

As we will discuss below this will increase the recombination efficiency.

One might expect that the storage time of the electrons in the trap can influence the recombination dynamics, since the motional behavior of the electron cloud in a trap is time dependent [109–111] and heating effects from external noise on the plate electrodes can also play a role. During the modest lifetime of 1.5 ms of our trap we have seen a decrease in efficiency which cannot be fully attributed to the loss of electrons from our trap during longer waiting times. The behavior of the recombination dynamics on different storage times was investigated by producing ions with scheme II. In Fig. 7.5 the normalized time delay profile is plotted for two different storage times (500 ns and 500 μs) showing that these profiles are identical. The recorded efficiency for a storage time of 500 ns was 2.0 % and for 500 μs it decreased to 0.7 %. We measured a 5-10 % loss of electrons in the trap over the 500 μs waiting time and thus the 65 % loss in efficiency cannot be attributed to just electron loss from the trap, since the number of recombined atoms scales linearly with the number of electrons in an electron pulse. A possible explanation is that heating effects of the electrons in the trap decrease the PFR efficiency, which will be discussed in more detail below.

A free electron is most likely to get recombined with the PFR scheme when it is close to the nucleus with zero kinetic energy, but essentially the coordinates (for a certain fixed distance to the ion) of the electron relative to the ion do not play a role. This means that it is not appropriate to characterize PFR with a cross section as it is with most other recombination processes. Therefore we introduced the concept of an interaction volume (V_{int}, Chapter 6) to describe the observed efficiency, which is the volume in space around the ion in which the electron has to be with a certain velocity to be recombined. A simple

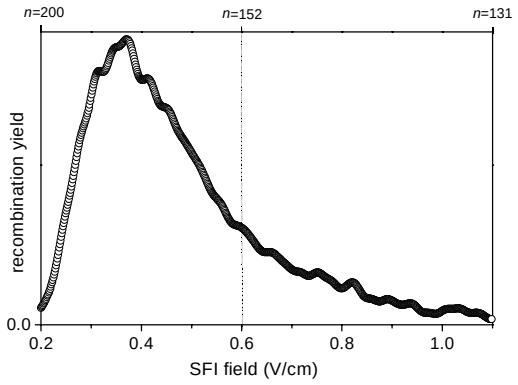

Figure 7.6: *The recorded state distribution by the technique of Selective Field Ionization. Note that indeed states are created around n=180.*

formula then predicts what this V_{int} should be:

$$N_{rec} = \rho_e \rho_{ion} V_{over} V_{int} \tag{7.1}$$

where N_{rec} is the number of recorded atoms $(10 \pm (3))$, ρ_e is the electron density in the electron pulses, ρ_{ion} is the ion density $(6 \pm (2) \times 10^4$ cm$^{-3})$, and V_{over} is the overlap volume of the electron cloud and the ion cloud. The size of V_{over} is determined by the smallest cloud: the electron cloud. We thus obtain a V_{int} on the order of 10^{-10} cm^{-3}. Such an interaction volume would correspond to the space occupied by a Rydberg state around $n \approx 180$. This indicates that high Rydberg states are produced around $n \approx 180$, by means of the PFR scheme. In the next section the interaction volume is discussed in more detail.

To verify this hypothesis we used the technique of Selective Field Ionization [2, 50] (SFI, Chapter 2), to probe the bound state distribution after the recombination event. The relation between the value of the electric field at which field ionization classically occurs and the principal quantum number n state is (in atomic units):

$$F = (\frac{E}{2})^2 = \frac{1}{16n^4} \tag{7.2}$$

By ramping a static electric field in time and monitoring at which time ionization occurs one can deduce the bound state distribution of an atomic or molecular system. Typically we ramp the electric field with a slew rate of 1.70 V/cm per μs, from 0.20 V/cm to 5.0 V/cm. In Fig. 7.6 a SFI trace is depicted of the recombined states when during the recombination event the electric field in the ion region is switched from 3.0 V/cm to 0.20 V/cm in 0.8 ns. The SFI detection started 1.4 μs after the recombination event. Clearly it is seen that we mainly produce states which are ionized by the lowest SFI fields. If we use Eq. (7.2) to determine which bound states we have produced we indeed observe that we are making Rydberg states with a principal quantum number around $n \approx 180$, in perfect agreement with the principal quantum number we estimated from our observed

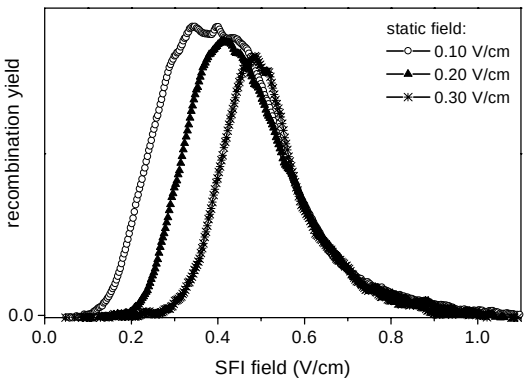

Figure 7.7: *The recorded state distributions for different values of the residual field after the recombination event. The open squares represent data for a residual field of 100 mV/cm, the solid triangles for a residual field of 200 mV/cm, and the open circles for a residual field of 300 mV/cm. It is clearly seen that an increase of residual field resulted in field ionization of the highest bound states.*

efficiency and the V_{int} deduced from it. In Fig. 7.7 we show 3 SFI traces where we varied the residual electric field after quick turn off. Similar states are produced, but we loose the highly excited states for stronger residual fields, which are unstable in the residual electric field.

We have also studied the effect of varying the magnetic field strength on the PFR dynamics. This parameter could be varied over the range of 13 mT to 64 mT. For fields lower than 13 mT the Penning trap would become unstable and the lifetime of the trap was strongly reduced. In Fig. 7.8a three different SFI traces are depicted for different magnetic fields. In Fig. 7.8b we plot the efficiency for various magnetic field strengths. For higher magnetic fields we record more recombined atoms. The increase in recombination efficiency can be explained by two effects. The first effect is of the nonzero temperature of the electrons cloud, which introduces a nonfinite velocity in directions perpendicular to the z-axis (transverse velocity). This means that for increasing temperatures of the electron cloud this transverse velocity increases and thus the cyclotron orbit increases. If the radius of the cyclotron orbit becomes comparable or larger than the radius of V_{int} the efficiency will decrease. This effect can be suppressed if the value of the magnetic field is increased since the cyclotron orbit is then reduced. The radius of V_{int} (10^{-10} cm^{-3}) is typically several micrometers (3 μm). The radius of the cyclotron orbit of the electrons can be estimated by: $r_c = \frac{\sqrt{2kTm}}{eB}$ and is also 3 μm if the transverse kinetic energy is 10 K in a field of 25 mT. The second effect of increasing the efficiency can be that a stronger magnetic field guides the electrons better to the ions so that the number of electrons arriving at the ion cloud increases.

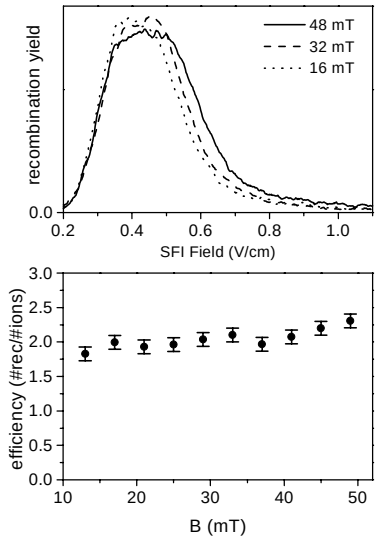

Figure 7.8: *a: The recorded state distributions for different values of the magnetic field strengths. An increase in recombination efficiency is observed for higher magnetic field strengths. b: Recombination Efficiency as a function of the magnetic field strength.*

7.5 Interaction Volume

So far we have discussed how the recombination efficiency can be understood in terms of an interaction volume which is an indication for the volume occupied by the created Rydberg state. A numerical estimate of V_{int} is obtained by classically solving Newton's equations, with a force equal to: $\mathbf{F}(t) = q(\mathbf{E}(t) + \mathbf{v}(t) \times \mathbf{B}/c)$. The electric field ($\mathbf{E}$) is the superposition of the Coulomb potential of the ions and external field, $\mathbf{v}$ is the velocity of the electrons and $\mathbf{B}$ is the magnetic field. An interaction volume of 3.0×10^{-10} cm^3 is found for a 3.8 ns electron pulse. Fig. 7.9b shows what V_{int} looks like if one considers the probability to get captured into any bound state when one recombines with a turn off of the static electric field from 1.5 V/cm to 0.2 V/cm in 0.8 ns. Clearly it is seen that there is a certain minimum volume beyond which no bound states can be formed. However any bound state with a volume larger then this minimum volume can in principle be formed. Notice that the maximum recombination probability is at $\rho = 0.8 \times 10^5$ *a.u.*, which would correspond to a Rydberg state with $2n^2 = \rho \rightarrow n = 187$. The minimum volume is in fact limited by two parameters: the value of the static electric field before the quick turn off and the slew rate of the quick turn off. For high values of the static electric field one can access more deeply bound states when a free electron passes over the saddlepoint in the modified Coulomb potential (this fieldstrength scales as n^{-4}), but the time dynamics will also be faster. Roughly one can say that to create a certain bound state one needs to turn off the static electric field within the time the electron turns around the ion in the volume occupied by that state. This time is given by the Keppler orbiting time and

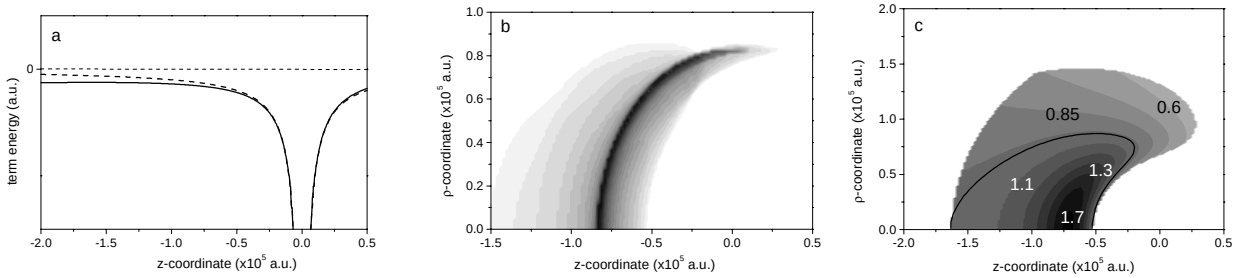

Figure 7.9: *a: Dotted line: Coulomb potential. Solid line: modified Coulomb potential by an electric field of 200 mV/cm. b: Recombination probability versus the turning point position of the electron in the Coulomb potential of the ion ($\rho = \sqrt{x^2 + y^2}$). Dark colours correspond to high probabilities. c: Contour plot of the energy of the recombined electron for t at the peak of the recombination volume. The energy contours ($E(|\mathrm{E}_{cut}|)$) increase linearly from the contour near $z = -0.7 \times 10^5$ a.u. and $\rho = 0$. The thick line shows the division between electrons that recombine with energy below the classical ionization threshold and those above.*

scales as n^2. Thus to create more deeply bound states one has to implement a higher static electric field with a higher slew rate. In our experiments we do not fully turn off the static electric field, and a static electric field of ∼200 mV/cm is still present after the quick turn off. Therefore recombined states with a principle quantum number higher than $n = 200$ are not stable and will field ionize. In Fig. 7.9c we show what the binding energy distribution is of the recombined states if we calculate the points to be captured into states with negative energy. The black line depicts the border between true bound and temporary bound if after the recombination event a residual electric field of 200 mV/cm is presents. Clearly we obtain the same minimum V_{int} for which recombination occurs, but now also a maximum volume occupied by the recombined states is observed induced by the static electric field. This effect can also clearly be seen in Fig. 7.7: by varying the residual electric field we have in fact control over which states we are making. For very little residual electric field, very high Rydberg states remain stable and are recorded in the SFI trace. For greater residual fields the very high Rydberg states become unstable and are ionized by the residual field.

An interesting feature arises when one records the state distribution or V_{int} as a function of the delay of the electric field turn off. In Fig. 7.10a V_{int} is calculated for different delays of the electric field turn off, and a decrease of V_{int} is observed for longer delay times. This indicates that, on average, for longer delay times more deeply bound states are made. In Fig. 7.10b this is indeed verified, where the state distribution is calculated for different delay times. In previous experiments with rubidium ions [98] (Chapter 6) the state distribution as a function of turn off time was investigated experimentally, showing that the state distribution for longer delay times was indeed extended to more deeply

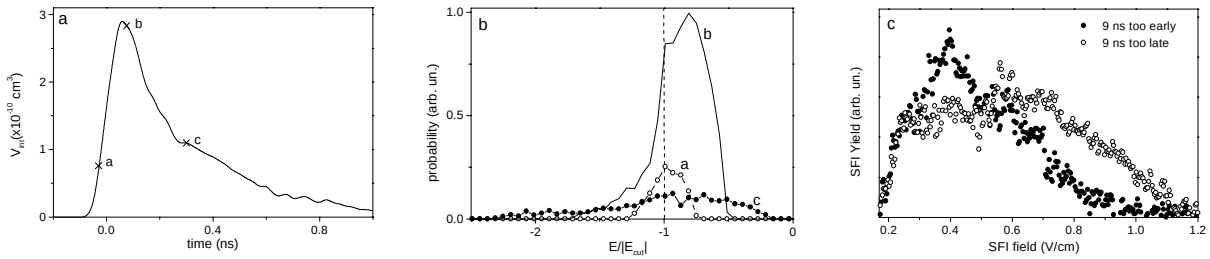

Figure 7.10: *a: Calculated V_{int} as a function of the delay time of the electric field turn off. A smaller V_{int} is calculated for longer delay times. The markers a, b, and c will be used in Fig. 7.10b. b: Calculated state distribution for different delay times (the markers a,b, and c correspond to the markers in Fig. 7.10a). $\frac{E}{|E_{cut}|}$ is the energy of the state divided by the classical ionization limit in a field of 200 mV/cm ($E = 2\sqrt{F}$). Open dots: delay time = -0.030 ns. Solid line: delay time = 0.075 ns. Solid dots: delay time = 0.300 ns. c: Experimentally recorded state distributions for different delay times of the electric field turnoff, when rubidium ions are recombined with free electrons (Chapter 6). The electrons were created by photoionizing lithium atoms by a pulsed laser, resulting in electron pulses of 10 ns duration.*

bound states. This effect was convoluted with the time duration of the electron pulses (11 ns) and therefore a difference in state distribution was seen for longer delay times. Two SFI traces at a delay time of 9 ns earlier and a delay time of 9 ns later than the maximum recorded recombination efficiency are depicted in Fig. 7.10c.

7.6 Discussion and Conclusions

The fact that Pulsed Field Recombination works with light atoms with different quantum defects indicates that indeed the PFR scheme is universal and is a promising scheme to recombine an anti-proton and a positron. The first efforts to produce anti-hydrogen with PFR are discussed in Chapter 9. In this work, an efficiency of 2.0 % is recorded and it is demonstrated that PFR can in principle be implemented in a configuration where the charged particles are trapped and spatially separated. The omission of an ion trap is justified since the inertia of the ion (anti-proton) compared to the electron (positron) is such that even in the static fields used in a PFR experiment (maximum field strength: 3 V/cm) the ions have hardly moved during the recombination event ($\pm$ 80 ns). Thus one can load an ion trap, turn off the trapping potentials for 100 ns and turn them back on again with hardly loosing any ions from the trap, while performing the PFR scheme during the 100 ns. Another reason for not building an ion trap is that an ion trap uses inhomogeneous fields. We would however like to use homogeneous (time varying) electric fields after the recombination event to characterize in detail the recombined states we

have produced.

The efficiency was shown to depend on the transverse temperature of the electron cloud and magnetic field strength where the highest efficiency was obtained for low temperatures of the electron cloud and high magnetic field strengths. This was understood by the fact that a faster transverse motion will lead to larger cyclotron orbits. If the cyclotron orbit exceeds the interaction volume, the efficiency of the PFR scheme becomes less. We observed a loss in efficiency for longer storage times of the trapped electrons which is explained by electron loss and heating effects in the Penning trap.

A more detailed description was given about the interaction volume where we explained that the recombination probability is highest when high Rydberg states are created. From the achieved efficiency and the introduced V_{int} it was concluded that Rydberg states with a principal quantum number of $n \approx 180$ are created and this was verified by measuring the state distribution. We have shown that the use of a residual field gives control over the range of created Rydberg states. Moreover, we have demonstrated experimentally and theoretically that the delay time of the electric field turn off strongly influences the state distribution of the recombined states. Longer delay times result in more deeply bound states.

The presented work can be related to a previous observation of recombination using pulsed electric fields [78]. In these experiments unipolar "half-cycle" pulses [4] were used to recombine a free electron with its parent ion: a broadband short (1.5 ps) laser pulse was used to ionize calcium atoms and shortly ($\backsim$ 5 ps) after the ionizing pulse it was recombined again by a unipolar "half cycle" pulse. In the time domain this process can be described as kicking the electron back to its parent ion, while in the frequency domain it is a strong field Raman transition between a virtual state in the continuum with a relative long lifetime and a bound state.

A last point worth noting is that to employ the PIRI [105–107] technique for molecular ion spectroscopy one needs a Rydberg state of a vibrationally cold molecule. In some cases it is not possible to create a Rydberg state in (complex) molecule by means of laser-excitation. We have shown that we can now load an electron trap by means of ionization by a laser pulse, and after 500 μs create a Rydberg state by recombining an ion and a free electron. This means that molecular ion spectroscopy can now be performed on species which were not accessible due to the failure of producing a Rydberg state by laser-excitation.

Chapter 8

Rydberg Carbon Clusters Prepared by Pulsed Field Recombination

The technique of Pulsed Field Recombination is used to recombine a free electron with carbon cation clusters, ranging from C_{60}^+ to C_{50}^+. It is shown that after the recombination the electron is left in a highly excited state. The recombination method produces a Rydberg state ($n \sim 180$) in a large carbon cluster, such as C_{60}, with an electronic energy spread of $\sim 1K$. We measured a recombination efficiency of ∼6%.

8.1 Why Rydberg Carbon Clusters?

The study of core excited cations has gained growing interest with the introduction of zero kinetic energy (ZEKE) [37,38], mass analyzed treshold ionization (MATI) [112], and photoinduced Rydberg ionization (PIRI) [105–107] spectroscopy. In PIRI spectroscopy a core electronic transition is photoexcited in a Rydberg molecule, which then decays by rapid autoionization. Because Rydberg molecules only weakly interact with optical radiation, the absorption wavelengths for a Rydberg molecule are very similar to those of the corresponding cation. A similar technique developed by Fujii *et al.* is called IR/PIRI [106, 107] in which the OH stretching vibration of cations is investigated by means of exciting Rydberg molecules with infrared radiation. There, the coupling of the vibrational with the electronic energy leads to autoionization. Not all molecular systems are accessible for these studies because the preparation of a Rydberg molecule is not always trivial, due to the fact that the temperature of molecules can be hard to control in typical experiments and the many vibrational degrees of freedom in the system. Therefore, up until now, it has not been possible to produce Rydberg states of large carbon clusters [113, 114] such as C_{60}, nor has the (IR-)photoelectron cation spectrum with the technique of (IR/)PIRI spectroscopy been measured. This would be a major achievement in the IR-spectroscopy of fullerenes [115]. In this chapter we report on the observation of carbon clusters in a Rydberg state ($n = 180$, $\Delta n \approx 20$), by means of Pulsed Field Recombination (PFR) [98] as introduced in Chapter 6 and 7.

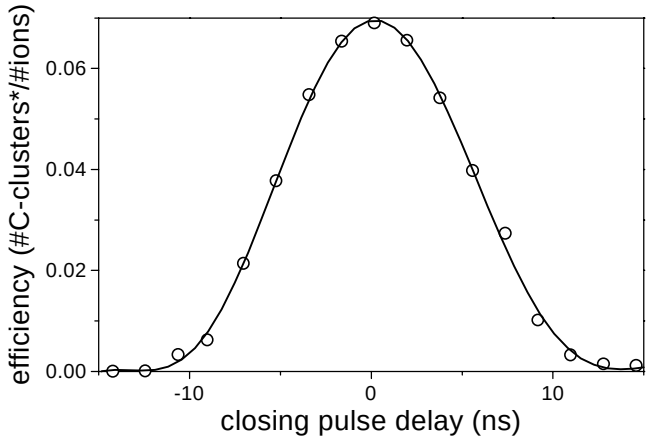

Figure 8.1: *The efficiency (number of recombined carbon clusters divided by the number of free ionic carbon clusters) as a function of the delay of the quick turnoff.*

8.2 Pulsed Field Recombination Scheme

In Chapter 6 and 7, we have experimentally and theoretically shown that an atomic (rubidium or lithium) ion can be recombined with a free electron by means of the PFR scheme. The recombined atom was then left in a highly excited state with a mean principal quantum number of $n \sim 180$ (± 20) [98]. Classical calculations were in excellent agreement with the experimental observations. These calculations showed that the dynamics of the PFR scheme were unaffected by the non-hydrogenic core of the rubidium or lithium atoms. This lead to the prospect that the PFR scheme is a universal method to recombine a free electron with any sort of ion. It was proposed that the PFR scheme can be used to produce 100-1000 cold anti-hydrogen atoms in a single experiment [98] in the already realized combined trap for particles of opposite charge of Gabrielse *et al.* [116](Chapter 6, and 7). In this chapter, we show that the PFR scheme can also be used to recombine a free electron with an ionic carbon cluster (C_{50}^+-C_{60}^+). An experimental method is presented where excited states in "hot" clusters ($\sim$750 K) are prepared with an electronically excited state energy spread on the order of 1 K. This observation opens the way for new approaches for photoelectron spectroscopy (PIRI, IR-PIRI) on complex molecules.

The PFR scheme can best be described as the time inverse of pulsed field ionization of Rydberg atoms [2], where an electron is captured into a bound state, by switching off an electric field at the moment it turns around in the vicinity of an ion (Chapter 6 and 7). In Fig. 8.1 the experimentally determined efficiency (density of recombined Carbon clusters atoms divided by the density of free ionic clusters) of this scheme is depicted as a function of the delay of the fast field turn off. This delay is with respect to the time when the free electron has its turning point in the electric field. Clearly, a maximum number of recombination events is recorded at zero delay. Note that efficiencies up to $6(\pm 4) \times 10^{-2}$ are obtained.

8.3 Experimental Realization

The PFR scheme was experimentally realized in a way very similar as explained in Chapter 6: a pulsed electron source [91] was created by means of photoionizing lithium atoms in a static electric field of 1.50 V/cm, with a pulsed (9 ns duration) narrowband ($\Delta\lambda <$ 0.2 cm^{-1}) dye laser (operating at 10 Hz). Typically electron pulses of 9 ns duration, with about $(5 \pm 2) \times 10^4$ electrons in a volume of 0.01 mm^3 were produced. The electric field is created by two parallel capacitor plates (separation: 10.0 mm) over which a voltage is applied (Fig. 8.2a). The ionizing laser pulse is focussed, creating a focus of 35 μm diameter. Focussing the laser in the direction of the electric field (z-direction) is important since the focus size determines the energy spread of the created electron pulses. After ionization, the free electrons are pushed towards the anode plate (connected to ground) through which a small hole is drilled. A grid covering the hole minimizes the distortions on the electric field. After this region, the electrons enter a field-free region of 15.0 mm, after which another set of parallel capacitor plates (with small holes, covered by a grid) is situated. Since the final plate is on -1.50 V, the electrons turn around halfway between these plates, separated by 10.0 mm. A cloud of ionic carbon clusters is awaiting the electrons in this region. A magnetic field was applied (B_z = 2.5 mT) parallel to the direction of propagation to minimize the perpendicular spread of the electrons during their travel to the ions.

The ionic carbon clusters were produced 500 ns before the photoelectrons were created by photoionizing and fragmenting gas-phase C_{60} molecules (T$\sim$ 750 K) in a static electric field of 1.50 V/cm. The gas-phase C_{60} molecules were produced by a resistively heated oven. We photoionized C_{60} molecules (IP = 7.6 eV) by the fourth harmonic (266 nm) of a Nd:YAG laser. A typical mass spectrum of the created ions is depicted in Fig. 8.2. The multiple ionization with 266 nm mainly produces the higher ionic carbon clusters. Successful recombination experiments were also performed where ionic carbon clusters were produced by photoionizing C_{60} molecules with the second harmonic (532 nm), resulting in average cluster sizes of C - C_7. The smaller cluster size, in the 532 nm experiment, can be understood by the fact that the absorption of multiple photons opens up another decay channel of the C_{60} molecules: fragmentation. Also the effect of delayed ionization is seen in the C_{60}^+ mass peak, which is due to thermionic emission of the highly excited molecular core [117, 118]. Detailed studies of the fragmentation and ionization dynamics of C_{60} are reported in Ref. [113, 117–120]. The decay time of this delayed ionization is measured to be $\sim$ 240 ns. By producing the ionic carbon clusters 500 ns prior to the arrival of the electron pulses assures that the major fraction of the excited C_{60} molecules have ionized at the moment of the recombination event. The C_{60} photoionization yields electrons with a velocity of $> 8 \times 10^5$ m/s. This in combination with the static electric field of 1.5 V/cm, assures that all the electrons of the ionized carbon clusters have left this interaction region at the time the lithium photoelectrons are created. However, the heavy ionic carbon clusters are virtually standing still during our experiment (Δl = 10 μm in 100 ns due to thermal velocity and Δl = 0.1 μm in 100 ns due to the static electric field).

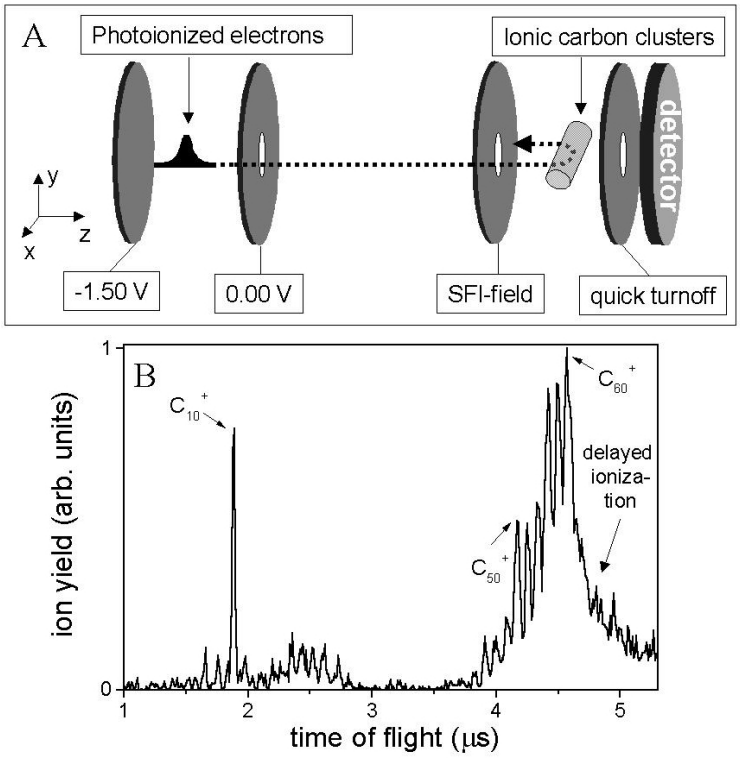

Figure 8.2: *a: experimental setup. A static electric field of 1.50 V/cm pushes the electrons towards the ion region, where the ions await the electrons in an opposite electric field. The cathode plate is connected to a fast pulse generator so that the field can be turned off within 1.0 ns. The anode plate is connected to a slow pulse generator so that after the quick turnoff the population distribution of the created Rydberg atoms can be probed. b: Mass Spectrum of the produced carbon clusters by photoionization of C_{60} molecules with 266 nm.*

The ionic carbon cloud resembles a cylinder with a radius of 35 μm in the z-and y-direction and a length of 10 mm in the x-direction, with a density of $2.4(\pm 0.4) \times 10^7$ cm^{-3}. In the ion source region, the electrons are decelerated by the electric field of 1.50 V/cm, and have their turning point at the position of the ion cloud. At that time, the field is turned off by dipping the voltage on the cathode plate from -1.50 V to -0.20 V in 1.0($\pm$0.2) ns. The electric field turn off is realized by connecting an impedance matched, fast pulse generator (Stanford Research Systems, model DG 535) to the cathode plate. The density of ionic carbon clusters is kept low with respect to the density of free electrons to prevent the effect of "trapping" the electrons in the attractive potential of the ion cloud. For the given volumes and densities, the electrons feel an attractive field of <30 mV/cm at the edge of these volumes. Such a low density plasma is therefore not stable when the ion region is biased with an electric field of 200 mV/cm. The experiments were performed in a vacuum chamber with a background pressure of 5×10^{-7} Torr.

8.4 Results: Interaction Volume

In Chapter 6 and 7 we have demonstrated that the observed efficiency with PFR can be understood by introducing an interaction volume. This interaction volume can be estimated with the following formula:

$$N(\tau) = \rho_{ion}\rho_e V_{over} \int_{-\infty}^{\infty} f(t'-\tau)V_{int}(t')dt' \tag{8.1}$$

where $N(\tau)$ is the number of recombinations at a certain delay (τ) of the quick turn off, ρ_{ion} is the ion density, ρ_e is the electron density, V_{over} is the overlap volume of the electron- and ion cloud, and $f(t) = \sqrt{\frac{4\ln 2}{\pi\alpha^2}}\exp(\frac{-t^2 4\ln 2}{\alpha^2})$ is a function which describes the time profile of the electron pulses (α is the duration of the electron pulses: 9 ns). In the case of ionic carbon cluster production with 266 nm (C_{60}^+- C_{50}^+) we have measured typically 15($\pm$5) recombination events per 5×10^4 electrons in an overlap volume of 0.01 mm^3 and an ion density of 2.4×10^7 cm^{-3}. Using Eq. (8.1), this observation yields an interaction volume of $(1.3 \pm 1.2) \times 10^{-11}$ cm^3. A theoretical estimate of V_{int} is obtained by solving Newton's equations (see Chapter 6 and 7). The electric field (**E**) is the superposition of the Coulomb potential of the ions and external field, **v** is the velocity of the electrons and **B** is the magnetic field. An interaction volume of 2.5×10^{-11}cm^3 is theoretically calculated for a 9 ns electron pulse, which is more than the estimation from the experimental data. The explanation for this will be discussed in section 8.6. We note that the spatial extent of such an interaction volume corresponds to Rydberg states around $n \approx 180$. The radius of the interaction volume is two orders of magnitude smaller than the average distance between neighboring ionic carbon clusters, which means perturbations from unrecombined ionic carbon clusters are negligible in this experiment.

8.5 Results: Rydberg State Distribution

A detailed picture of the final state distribution of the pulsed field recombined Rydberg clusters was obtained with the technique of Selective Field Ionization (SFI, Chapter 2) [2, 50]. A Rydberg state of an atom or molecule can be ionized if an electric field is applied. The relation between the value of the static electric field at which ionization classically occurs and the principal quantum number, n, of a state is in atomic units: $F = (\frac{E}{2})^2 = \frac{1}{16n^4}$. When the electric field is slowly ramped in time and the field at which Rydberg molecules decay is monitored, the populated Rydberg states can be approximately deduced. In our experiment, we use a field ramp of 1.50 V/cm in 1.8 μs, 900 ns after the fast field turn off. This was realized by connecting a voltage ramp to the anode plate of the ion region. The field ramp pushes the field ionized electrons towards the cathode plate through which a hole was drilled covered with a grid. Directly after this plate a set of Micro-Sphere-Plates (MSP's) is situated that records the ionized electrons. In this way, we record at which times, and hence at what field strengths, electrons are being field ionized. During the 900 ns after the quick turn off and before the SFI ramp,

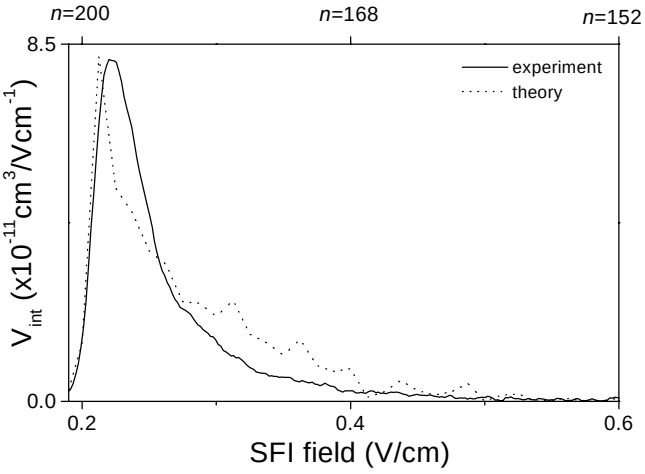

Figure 8.3: *Calculated state distribution (dotted line) of the recombined Rydberg clusters, compared with experimental state distribution (solid line). The experimentally determined interaction volume is varied within its uncertainty to optimize the comparison with theory.*

effects of three body recombination and radiative recombination are ruled out since the rates of these processes (1 s^{-1}) are far too low at our densities.

In Fig. 8.3, the Rydberg state distribution as a result of the PFR by the 1.0 ns turn off is depicted for recombination of the carbon clusters (C_{50} - C_{60}), showing that the state distribution peaks for small SFI fields. Since the 1 ns turn off reduces the electric field to 0.2 V/cm, states with a principal quantum number beyond $n = 200$ are not stable. From Fig. 8.3, it is deduced that Rydberg states are produced around $n = 190$.

8.6 Semi-Classical Calculations

The calculation depicted in Fig. 8.3 shows a direct comparison between theory and experiment, and clearly good agreement is obtained. Starting out with the state distribution obtained from solving Newton's equations ($< n >= 180$ with $\Delta n = \sqrt{< n^2 > - < n >^2} = 20$) the SFI trace is calculated (using the Landau-Zener approximation [50]). To obtain this level of agreement, the polarizability of the ionic carbon clusters and autoionization of the recombined carbon clusters is implemented. The polarizability is included through a local potential $-\alpha/2r^4$ at large distances; $\alpha \sim 540$ atomic units [121,122]. Autoionization of the Rydberg states by interactions of the electron with the hot C_{60}^+, is included through a model that allows the electron energy to change: every time the recombined electron gets within 5 atomic units of the center, it gets a kick in a random direction so that the energy of the electron is just as likely to increase as to decrease. If the kick increases the energy, the electron leaves (autoionization). If the kick decreases the energy, the electron will be in a lower Rydberg state. For this deeper bound state the time to return to the

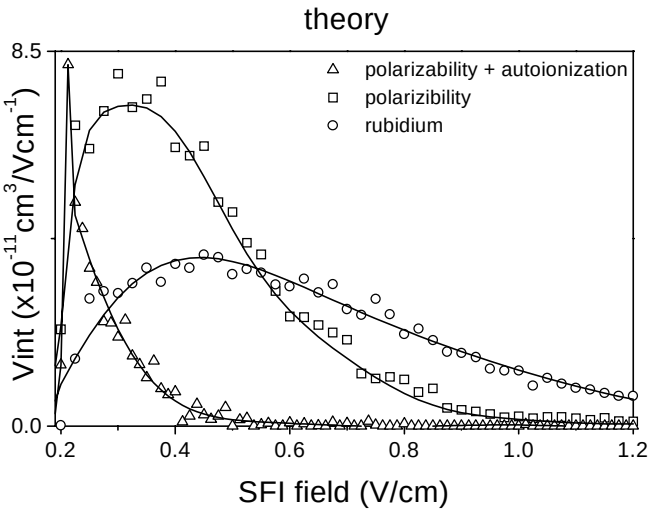

Figure 8.4: *Calculated SFI traces. Open circles: Rb model, weak, elastic interactions with the core. This resulted in an* V_{int} *of 2.5x10*$^{-10}$ *cm*^{3}*. Open squares: the same model, but now the huge polarizability of* C_{60}^+ *is included in the capturing step and in the calculation of the SFI trace. This resulted in an* V_{int} *of 2.7x10*$^{-10}$ *cm*^{3}*. Open triangles: calculation including the polarizability of* C_{60}^+ *and autoionization due to the hot* C_{60}^+ *core, during the 900 ns waiting time. Resulting in a recombination signal loss of about 70%.*

C_{60}^+ decreases, so the electron will rapidly get kicked again. This is like a random walk where the time between steps decreases in one direction and the time between steps increases in the other direction. The resulting V_{int} from this calculation is 0.7×10^{-11} cm^3, in good agreement with the experimental observation: (1.3±1.2)x10^{-11} cm^3. From the calculation, roughly $\frac{2}{3} - \frac{4}{5}$ of the originally recombined electrons are ejected before the SFI detection.

In Fig. 8.4, we present the result of 3 calculations showing the effect of the large polarizability and autoionization on the SFI signal. The dashed line gives the SFI signal for Rb; the polarizability of Rb^+, $\sim$ 9 atomic units, is 60 times smaller than for C_{60}. When we include the huge polarizability of C_{60} molecules, we observe a dramatic change in the shape of the SFI signal. The total Rydberg population remains about the same as can be seen from the unchanged integrated SFI yield. The electron does not get very close ($<$ 20 atomic units) to the ion during the recombination event; V_{int} only depends on the long range Coulomb interaction to a good approximation. The large polarizability of C_{60} causes that the same Rydberg states ionize at lower SFI field strength. The SFI signal does differ because the SFI signal for Rb does not follow the $F = (\frac{E}{2})^2$ rule very well; the relatively small region of space where the potential is non-Coulombic allows the electron to remain attached to the Rb^+ ion for a longer time and it thus emerges at a higher field. When autoionization is included in the C_{60}-model together with the polarizability, we find that high n-states (lower SFI fields) are almost unaffected but the lower n-states (higher

SFI fields) are sensitive to autoionization and we lose a part of the recombined clusters by autoionization. The autoionization rate scales as $\sim n^{-4}$ since it depends on the number of core passages per unit time ($\sim n^{-3}$) and how often the angular momentum (l) is low per unit time ($\sim n^{-1}$).

ZEKE experiments [37, 38] showed that not only l-mixing can be important but also m-mixing, for these high principal quantum numbers. Below we argue why we believe m-mixing does not play a role in our experiments. The only way m-mixing can occur is through a collisional effect of ions [123–125] with the recombined Rydberg carbon clusters. Chupka [123] does not state on which time scale m-mixing occurs, but only states a possible lifetime increase of an additional factor of n due to distribution of the wave function over all m-states. Merkt *et al.* [125] have performed calculations, which show that in 100 mV/cm and at a *fixed* ion distance of 50 μm, m-mixing can occur. However, they state that their model is valid if the field of the ion is less in magnitude than the homogeneous dc field, else the m-mixing is overestimated. In some of their presented data they show the onset of m-mixing at a distance of 10 μm and this corresponds to a field produced by the ion of 144 mV/cm: this is of the same order of the static electric field of 100 mV/cm. Moreover: if there is m-mixing than this should occur within the time of a PFR experiment ($\sim$1 μs). Merkt *et al.* estimate the time it takes to m-mix by using Fermi's golden rule: 0.1 μs. These calculations overestimate the m-mixing value. The estimate goes as follows: the average number of states in a energy width of $6R_h n^2(\frac{F}{5.14\times10^9})$ (energy spread of a Stark manifold, for a certain principal quantum number n, and electric field F) is given by: n^2 (because there are $\sim n$ Stark states with $\sim n$ possible m), from this a density (ρ) can be retrieved. The coupling (V) between Stark states of different m is about 0.3×10^{-4} cm^{-1} at a distance of 50 μm (retrieved from calculations). Using Fermi's golden rule (decay rate of initially prepared state): $\Gamma = 2\pi\rho V^2$, Merkt *et al.* obtain a mixing time scale of 0.1 μs. However this is an overestimate of a factor of 100 for just the m-mixing rate, since Merkt *et al.* used the number of states as n^2 while in fact there are only n different m-levels. This would put the timescale of m-mixing outside the timeframe of our experiments.

Dorofeev *et al.* [124] calculate the m-mixing from *moving* ions under the conditions in ZEKE experiments. They state that m-mixing occurs when there is the situation of a non-collinearly moving ion in combination with a stray DC field. Their conclusion is that m-mixing occurs when: 1) the ion motion is essentially non collinear; 2) the strength of the ion field is of the same order as the stray field (in our experiments that means that the ion has to approach the recombined cluster within 8 μm); 3) the mixing time should be shorter than the time for an experiment to take place (above we have discussed that this is not the case in our experiments); 4) the velocity of the ion should be greater than $170\frac{n}{(\pi-n^{1/2})r_0} = 216$ m/s, but smaller than $170\frac{n^{3/2}}{r_0} = 9616$ m/s, with r_0 the initial distance between the ion and the molecule (in μm). The ion velocity in our experiment is about 130 m/s ($v = \sqrt{2kT/m} = 130$ m/s, with $T = 750$ K). These points strongly suggest that m-mixing does not significantly contribute in our experiment.

Finally a simple calculation can be performed showing that m-mixing in our experiment is not pronounced. The idea is that the electric field of 200 mV/cm reduces the

collisional effect of ions inducing m-mixing. M-mixing occurs when the electric field axis is modified sufficiently by the Coulomb field of a perturbing ion. From the ion density an average ion distance is estimated: 50 μm. The ions have a thermal velocity of $v = \sqrt{2kT/m} = 10^2$ m/s. The amount by which the field axis is changed ($\Delta\theta$) when an ion is moving towards a Rydberg carbon cluster with a velocity ($v = 100$ m/s) perpendicular to the static electric field, after 10 angular momentum oscillation times ($\tau_{osc} = 6$ ns for $n = 200$ and $F = 0.2$ V/cm [2]) is: $\Delta\theta = 10\tau_{osc}\frac{\partial\theta}{\partial t} = 10^{-2}$ rad. This amount is sufficiently low, compared to the effect of angular momentum mixing, to omit the effect of m-mixing in our model. However if the Rydberg clusters are produced to be stored for an extended period of time (> 1 μs), m-mixing will play a significant role.

8.7 Discussion and Conclusions

Besides the potential application of this new recombination technique in the creation of atomic anti-hydrogen, we propose that our scheme can be used in the formation of Rydberg carbon clusters for (IR)-spectroscopy. The way the carbon clusters are prepared leaves them with an internal energy of 750 K, and thus the clusters are excited to various hot bands. This means that laser-excitation of a cluster to a Rydberg series with a very well defined energy, needed for infrared spectroscopy experiments, is impossible. The PFR scheme leaves the recombined clusters in a Rydberg state with an electronic energy spread of 1 K ($\Delta n = 20$ at $n = 180 \rightarrow \Delta$E ~ 1 K). This resembles a narrowband laser-excitation (< 1 cm^{-1}) of a carbon cluster to the Rydberg series, making it possible to prepare a well defined Rydberg cluster.

In summary, we have observed recombination of ionic carbon clusters with free electrons with the use of fast field pulses, resulting in Rydberg carbon clusters. Efficiencies as high as 6.0×10^{-2} have been achieved and a simple improvement (due to the electron pulse duration mismatch) can raise the efficiency significantly. The recombination can be understood with arguments which do not require mechanisms relying on the magnitude of the quantum defects of non-hydrogenic atoms or molecules. This indicates that the PFR mechanism works for any atom or molecule and yields recombined clusters in a Rydberg state with an energy spread of 1 K.

Chapter 9

Pulsed Field Recombination at CERN: a progress report

The progress of the production of cold anti-hydrogen by Pulsed Field Recombination is discussed in this chapter. The described experiments were performed at CERN for the ATRAP collaboration. The ATRAP experiment consists of a large Penning trap to store charged anti-matter particles (anti-protons and positrons). A preliminary scheme is presented in which the trapped positrons and anti-protons could be recombined by the Pulsed Field Recombination scheme. The first attempts of this scheme to observe anti-hydrogen did not succeed. Possible explanations for this failure are given with future directions and suggestions.

9.1 Introduction to Anti-Hydrogen

Dirac predicted a new duality of matter in 1928 [126] when he wrote down his version of quantum mechanics. Dirac was especially concerned that his quantum theory should manifestly respect Einstein's special relativity. Two remarkable predictions resulted from Dirac's theory: the existence of electron spin and the existence of anti-matter [126]. Indeed, four years later, the first charged anti particle was found by Carl Anderson (1931): the positron [21,22]. Gradually physicists learned how to make other charged anti-matter species, such as the anti-proton, with the help of accelerator rings. In those rings charged matter is accelerated so that they almost travel with the speed of light and subsequently they are smashed into each other. In such a collision all kinds of particles are made (energy is transferred into mass, according to $E = mc^2$), including anti-particles, whose mass distribution depends on the collision energy. However, until 1996, no observation was made of the production of neutral anti-matter (see also Chapter 1.6). When a anti-proton passes a heavy target-nucleus close enough, electron-positron pairs are produced accidently. In some rare cases the anti-proton catches the positron from the electron-positron pair and anti-hydrogen is produced. This strategy yielded the first anti-hydrogen observation in 1996 [26]. Nine anti-hydrogen atoms were made with a relativistic velocity and annihilated by collisions within 20 ns. Performing meaningful measurements on just

a couple of high energy anti-hydrogen atoms is impossible and therefore one would like to be able to produce a large quantity of cold (low energy) anti-hydrogen atoms.

The production of cold (4.2 K) anti-hydrogen is the first goal of the ATRAP [28] collaboration, directed by prof. G. Gabrielse, at CERN. This production will allow the careful study of neutral anti-matter and a direct comparison between matter (hydrogen) and anti-matter (anti-hydrogen). Trapped positrons and trapped anti-protons are used as ingredients to produce anti-hydrogen by the recombination of these two charged anti-matter species.

In Chapter 6, 7, and 8 we report on experiments towards the production of anti-hydrogen by Pulsed Field Recombination (PFR) at ATRAP. In section 2 of this chapter we discuss the apparatus and the trapping mechanism of electrons, positrons, and anti-protons. In section 3 the detectors used in the experiments are described. The experimental realization of PFR is sketched in section 4. As will be discussed below, two major problems still need to be overcome to realize PFR with positrons and anti-protons: 1) the reduction of background signal from unrecombined anti-protons, and 2) the reduction of the "motional Stark field". This motional Stark field is due to the presence of a $\sim 6\ T$ magnetic field. A Rydberg atom in such a strong field with a velocity corresponding to a thermal energy of 4.2 K perpendicular to the magnetic field, will experience an electric field of $\sim 14\ V/cm$. Such a field will field ionize a Rydberg atom with a principal quantum number n of 180, while these states are expected to be created with the technique of Pulsed Field Recombination. In the final section of this chapter we discuss strategies to overcome these two hurdles.

9.2 Anti-Proton and Positron Trap at CERN

The ATRAP collaboration at CERN, uses a Penning trap [108] to store the two anti-hydrogen constituents. A Penning trap employs the combination of magnetic and electric fields to trap a charged particle. In general, an inhomogeneous electric field is created by ring electrodes, which are situated inside the bore of a (super conducting) magnet (see Fig. 9.1). The electric field creates a potential well in the z-direction, trapping a charged particle in this direction. The "conning" electric field along the z-direction is inevitably accompanied by an "anti-conning" electric field in a direction perpendicular to the z-direction. A magnetic field is present along the z-direction so that any movement of a charged particle perpendicular to this direction results in the superposition of a cyclotron and magnetron orbit, and the particle is trapped in all three dimensions. A comprehensive and thorough overview of the dynamics of a charged particle in a trap has been given by Brown and Gabrielse [127].

To produce anti-hydrogen, positrons and anti protons are needed. A β-decay radioactive source delivers these positrons. In these experiments a 110 mCi ^{22}Na source is used. The positrons released from this source enter the trap through a 10 μm titanium window, where they pick up an electron and form positronium (the bound state of a positron and an electron). Once this neutral positronium is near a trapping potential, it is field ionized

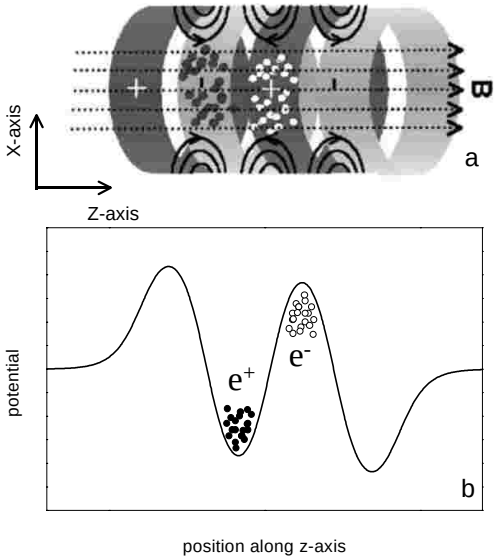

Figure 9.1: *a: Schematic representation of a Penning trap. Ring electrodes are used to create inhomogeneous electric fields, trapping a charged particle in one coordinate (z-direction). A homogeneous magnetic field parallel to this coordinate is used to trap the particle in the other two coordinates (x- and y-direction). b: Potential landscape produced by the ring electrodes.*

(see Chapter 2) by the electric field generated by the trapping potential and depending on the potential well structure the positron or the electron is trapped [128]. A typical trap depth is $\sim$ 3 eV (or 30.000 K). In this manner about $\sim 10^6$ positrons could be loaded in a trap in 40 minutes. Since the experiment is in a cryogenic environment of 4.2 K the hot positrons loose energy by synchotron radiation until their energy is reduced to 4.2 K [127].

The radiation damping rate is proportional to a high power of the transition frequency, and thus for radiation damping to occur, the accelerated motion of the charged particle has to be of high frequency. For electrons, the cyclotron motion has a associated frequency of $\sim$ 150 GHz (10^{-2} K) for the trapping potentials and magnetic field used in these experiments [130], resulting in a cooling rate of $\sim 13\ s^{-1}$ [127]. The axial- and magnetron frequency of the electron has a frequency associated with it of $\sim$ 60 MHz and $\sim$ 150 kHz respectively, and radiation damping becomes insignificant. For heavy particles (for instance the anti-proton) radiation damping can also be neglected since the cyclotron frequency and cyclotron radius is proportional to the inverse mass of the particle, and therefore the damping rate scales as $\gamma \propto \frac{1}{m^3}$, resulting in an extremely small cooling rate. Therefore, to cool heavy particles, a different cooling mechanism is employed, explained below. The axial motion can be resistively damped by an external circuit [109], and the magnetron motion can be damped by sideband cooling [127, 129]. Both mechanisms are explained in section 3.1 of this chapter.

In order to trap anti-protons, one needs free anti-protons. At CERN anti-protons are created by smashing high energy protons into a target. This abrupt stopping of the protons releases a large amount of energy in a small volume so that anti-matter - matter pairs are produced, among which anti-protons and protons. The anti-protons are then collected in the anti-proton decelerator ring (The AD ring, which is an approximate circle with a circumference of 188 m) to cool them down to 5 MeV (stochastic cooling [131,132]), from which they are directed to three different experiments (the ATRAP, ATHENA, and ASACUSA experiment). The anti-protons enter the trap through a degrader window (thin sheet of beryllium) so that they are decelerated to an energy around 1 keV. The anti-protons follow the field lines of the strong magnetic field towards the other side of the trap where they bounce of a potential wall back to the degrader. By this time the degrader is biased such that it creates a potential wall for the anti-protons and the hot anti-protons are trapped. In order to cool the anti-protons to 4.2 K, electrons are loaded into the trap by a field emission point. The hot electrons loose their energy via synchotron radiation and are trapped with an energy of 4.2 K. The simultaneous confinement of the cold electrons and the hot anti-protons enables the cooling of the anti-protons to 4.2 K, by collisions of the hot anti-protons with the cold electrons (sympathetic cooling [133]). Each time a hot anti-proton collides with a cold electron, the anti-proton can loose some energy to the electron, which in turn will loose this energy by synchotron radiation and therefore the ensemble will thermalize to 4.2 K. After a cooling time of 30 seconds the electrons are pulsed out of the trap by three fast (20 ns risetime) and short duration (100 ns) voltage pulses which open the trap. This is done because annihilations of electrons and positrons will occur when anti-protons (accompanied by the electrons) are combined with positrons to produce anti-hydrogen. Due to their large inertia, the anti-protons stay in the trap, while the light electrons escape. Typically 8000 anti-protons can be accumulated in 2 minutes, since every two minutes the Anti-proton Decelerator (AD) delivers a bunch of 8×10^6 high kinetic energy anti-protons and the trapping efficiency of these hot anti-protons is 10^{-3}.

9.3 Anti-Proton and Positron Detectors

9.3.1 Non-Destructive Detection

Just like any charged particle in a trap, the anti-proton and the positron can be detected by a radiofrequency detection technique first reported by Wineland *et al.* [109]. In this technique image charges of the charged particles are measured on the trap electrodes. In practice this is realized as follows: an LCR circuit of high Q is connected between two electrodes. This LCR circuit oscillates at its characteristic frequency: $\frac{1}{2\pi\sqrt{LC}}$. The resistor feeds 4.2 K thermal noise (Johnson noise) into the circuit and therefore into the trap. If this characteristic frequency corresponds to the axial frequency of a charged particle in the trap (the circuit is "tuned"), the frequency response of the "tuned circuit" is altered. An intuitive way of thinking about this is that the Johnson noise is shortened by the charged

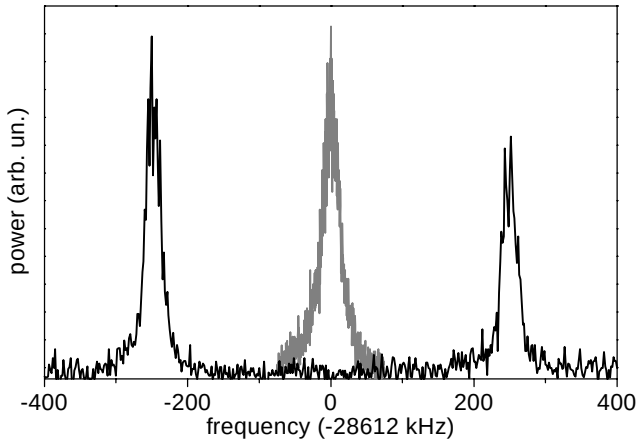

Figure 9.2: *Non-destructive measurement of charged particles in a Penning trap. The Johnson noise spectrum (grey line) is altered into two Lorentzians (black line) with a spacing proportional to the square root of the amount of particles in the trap.*

particles. The uncoupled Lorentzian shape of the Johnson noise spectrum is altered into two Lorentzian's (see Fig. 9.2) with a spacing proportional to $\sqrt{N}$ (where N is the number of particles in the trap), enabling the measurement of the particle number in a trap in a non-destructive manner. Note that only for a cloud in a harmonic potential the particle number can be deduced with accuracy, since the axial roundtrip time of a particle is then independent of its energy. In principle the dynamic range of this detection scheme is such that it can detect any amount of charged particles for perfectly harmonic potentials. In these experiments the smallest cloud size which was detected contained 10^3 electrons and the accuracy was 5 %.

The energy lost in the effective resistance of the tuned circuit induces a damping of the axial motion, until the system is in thermal equilibrium. This is understood by the fact that the current introduced by the image charges through the resistor leads to a voltage $V = IR$ over the resistor and thus to an electric field along the z-axis in the trap. This electric field results in a force on the trapped particle which decelerates it, and thus the axial motion is damped.

Since the magnetron motion is unstable, the cooling of this motion involves adding energy to the particle to force it up the potential hill in the direction perpendicular to the z-direction. The magnetron radius is decreased by applying a radio-frequent drive at a frequency of the sum frequency of the axial frequency and the magnetron frequency. The axial motion is continuously damped by the tuned circuit, so that no energy is added to this motion, however the magnetron motion gains in energy and thus the radius of the magnetron orbit is decreased. A thorough treatment of the resistive and sideband cooling mechanism is given in ref. [127].

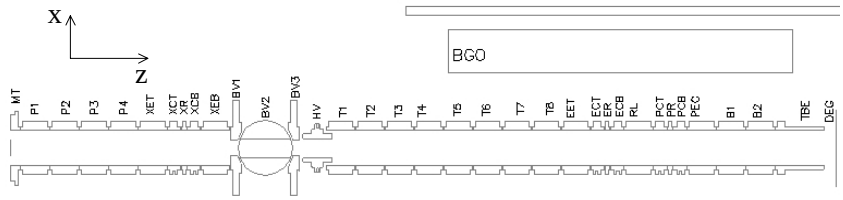

Figure 9.3: *Layout of the trap used at ATRAP. A strong magnetic field (6 T) is present along the z-direction, while the inhomogeneous electric field is produced by the ring electrodes.*

9.3.2 Destructive Detection

Positrons and anti-protons could also be measured destructively, with the aid of scintillators. A BGO crystal was used as a scintillator to record annihilations of positrons and electrons with an efficiency of ∼1%. Scintillating fibers were used to record the photons produced in the annihilation process of an anti-proton and a positron with an efficiency of 50 % (2π detector). The scintillator acts as a medium which collects the photons of the annihilation process. These photons are then directed into photo-multipliers to amplify the signal. A Parallel Plate Avalanche Chamber (PPAC) was also available to detect the anti-protons in a destructive manner. The principle of operation is as follows. A gas is situated in between two grids, which are biased with $\sim$ 1 kV. If an anti-proton enters this region, it will annihilate so that gamma rays are produced. These gamma rays will have an ionizing effect and due to the presence of the strong field, a discharge occurs. This discharge can subsequently be recorded on an oscilloscope. The efficiency of this detector is 50 %. The PPAC and the scintillators were setup to have a temporal response of $\sim$ 50 ns for one single count. From the analogue signal, a digitized signal was made, enabling to count the number of annihilations after a certain trigger.

9.4 Pulsed Field Recombination

9.4.1 Experimental Realization

In Fig. 9.3 the trap layout is depicted. The positrons enter the trap form the left and the anti-protons from the right. Each electrode could be controlled by a DC power supply with a time constant of 0.1 s. The positrons and electrons could be counted in two harmonic trapping regions: XR and ER. The whole experiment was computer controlled from a Faraday cage where all the electrical equipment was situated. Particles could be moved through the trap with hardly any losses, this enabled us to store particles in many configurations.

Pulsed Field Recombination as introduced in chapter 6, 7, and 8 requires fast switching

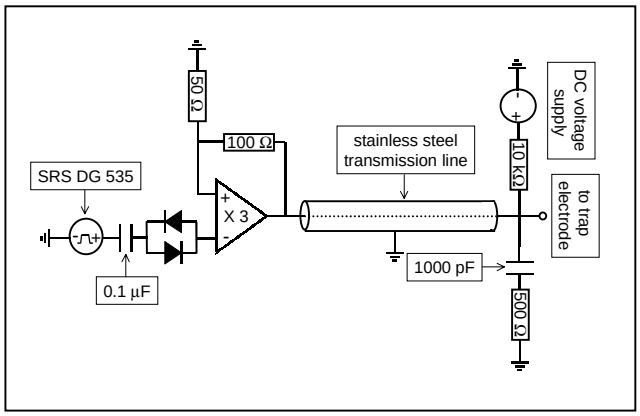

Figure 9.4: *Schematic representation to couple fast voltage pulses on to a trap electrode.*

of electric fields. In order to investigate PFR in the ATRAP configuration, fast micro-coax lines had to be installed, to turn off the electric field in a specific region in the trap on a timescale of nanoseconds. This is in contradiction with the normal operation mode of the trap: in order to have low temperature trapped particles, noise sources are an important issue. Therefore all the voltage lines to the electrodes are strongly filtered (time constants of 0.1 s). Clearly one cannot filter fast lines with such a time constant when one requires nanosecond switching times, and filters had to be omitted on these lines. It was therefore important to keep the number of fast lines as low as possible. Moreover, the voltage source connected to the fast line needs to have a low noise output. Generally, pulse generators are not designed to have low output noise since the device requires a large bandwidth at the output. To tackle this problem a fast diode (1N 44 48 PH) was connected in series with the output of the pulse generator and the trap electrode. The diode only conducts when the voltage exceeds the bandgap voltage so that noise (lower than the bandgap voltage) is suppressed when the pulse generator is not firing.

Two SRS DG 535 pulse delay generators were used to produce fast pulses. In a typical experiment pulse heights of ∼6.0 V were required and therefore we had to amplify the outputs of the SRS DG 535 pulse generators (the maximum output of a SRS DG 535 pulse generator is 4.0 V). This was done by using fast operational amplifiers, or opamps (LM 7171) which have a slew rate of 4.1 $kV/\mu s$. The voltage response of the circuit was fine-tuned by adding a resistor (∼39 ohm) in series with the opamp and the electrode. This resulted in pulses of 6.0 V with a rise and fall time of 22.0 ns. The whole circuit is depicted in Fig. 9.4. Note that the pulse generators are AC coupled so that a DC voltage supply could be connected to give a voltage offset to the applied pulses. The fast lines were connected to electrode T3, T8, and EET. Since the residual noise on the output after the diode into the opamp was also amplified we disconnected the power going into the opamp by a computer controlled relay when fast pulses were not needed.

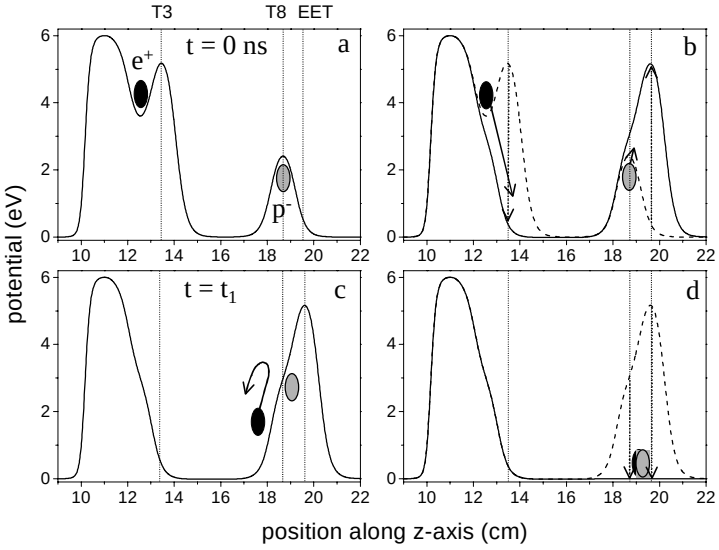

Figure 9.5: *Sketch of the proposed PFR scheme in the ATRAP configuration. At $t = 0$ ns positrons and anti-protons are trapped in spatially seperated wells (a). The positron trap is pulsed open (b) so that a positron pulse is produced with a well-defined energy, while simultaneously the voltage of electrode EET is raised from 0.0 V to 6.0 V. At $t=t_1$ the positrons turn around at the anti-protons (c) and the voltages on electrode EET and T8 are simultaneously switched to 0.0 V, so that the electric field is quickly turned off (d).*

9.4.2 Implementation of the PFR Scheme at ATRAP

A potential well for positrons was created (see Fig. 9.5a), centered at T2 by biasing HV, T1, and T3 to +6.0 V, while T2 was biased to +3.0 V. The voltage on T3 could be switched from +6.0 V to 0.0 V so that he trap was opened and a positron pulse was created with a energy determined by the potential difference of T2 and T3. Electrodes T4, T5, T6, T7, and EET were grounded while electrode T8 was biased to +3.0 V. This created a potential well for anti-protons at T8. Electrode T8 was connected to a pulse generator which supplied 3.0 V negative going fast pulses, while EET was connected to a pulse generator which supplied 6.0 V positive going pulses (see Fig. 9.5a). At $t = 0$ ns the positron trap is pulsed open by switching the voltage on T3, and at the same time the voltage on EET is switched to +6.0 V so that an electric field ramp is created from T7 to EET of 3.0 V per electrode ($\sim$3.0 V/cm). The positrons travel towards the anti-protons and are decelerated by the electric field ramp starting at T7. At $t = t_1$ the positrons turn at the center of T8 and the voltage on T8 is switched from +3.0 V to $\sim$0.0V. Simultaneously the voltage on EET is switched from +6.0 V to 0.0 V. At this moment bound states of anti-hydrogen can be expected. Since this particle is neutral it is not trapped by the superposition of the electric and magnetic fields and thus it starts travelling to the wall of the apparatus with a speed close to the thermal velocity of the

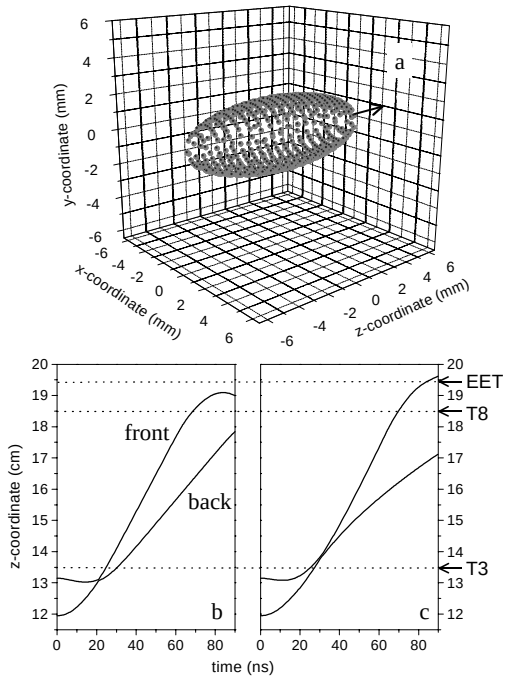

Figure 9.6: *a: Shape of a spheroid,* $\frac{\sqrt{x^2+y^2}}{a} + \frac{z}{b} = 1$*, with* $a = 2.0$ *mm, and* $b = 6.0$ *mm. The arrow indicates the direction of propagation. b: Calculated flight path of the front and backside of a spheroid-like positron pulse (*$a = 2.0$ *mm, and* $b = 6.0$ *mm), when at t=0 ns the positron well at electrode T2 is pulsed open, without taking account for space charge effects. c: same as b, now accounting for space charge effects (density:* 1×10^6 cm^{-3}*).*

anti protons ($v = \sqrt{2kT/m} \approx 300$ m/s, at 4.2 K). At the moment it hits the wall the positron and the anti-proton annihilate with their matter counterparts, producing mainly gamma rays and pions. The pions in turn produce additional gamma rays and all the photons are detected in scintillators surrounding the trap.

Since the amount of anti-proton beam time was limited, we performed several experiments without anti-protons to calibrate the time of arrival of the positrons at T8, and the value of the electric field in the trap. Calculations were performed to simulate the flight path of charged particles in the trap, which are discussed in the next section.

9.4.3 Integration of the Equations of Motion of a Charged Particle in the Trap

For an accurate estimate of how to overlap a positron cloud and a anti-proton cloud by the above described scheme, one needs to model the dynamics of the charged particles in the trap. This was done with calculations based on a numerical integration (Runge-Kutta integration with adjustable step size) of the equations of motion of a charged

positron cloud in the (time dependent) on-axis potential landscape in the center of the trap (the anti-proton cloud was assumed to remain fixed in space during a PFR experiment, due to the inertia of an anti-proton). The shape of a spheroid ($\frac{\sqrt{x^2+y^2}}{a} + \frac{z}{b} = 1$, see Fig. 9.6a) was chosen for the positron cloud, in agreement with the observations of previous studies [134–136]. In this manner the flight path of the positron pulse could be monitored, as well as its change in shape. The change of shape was restricted to the z-direction since the strong magnetic field prevents the expansion or reduction of the cloud size in directions perpendicular to the magnetic field. This enabled us to calculate at what time and where the positron pulse would turn in the potential landscape of Fig. 9.5, so that the right starting conditions could be chosen for a PFR experiment.

The space charge of the positron pulse is an important issue with the densities used ($10^6 - 10^7\ cm^{-3}$). In order the simulate the effect of space charge in the positron cloud during its travel in the time varying potential landscape, the spheroid was cut up in 100 slices. The Coulomb expansion of the spheroid was incorporated by accounting for the electric field generated by all the individual slices at the two ends of the spheroid. In Fig. 9.6b the trajectory of the positron cloud is depicted, when at t=0 the positron well of Fig. 9.5 is pulsed open for the spheroid depicted in Fig. 9.6a. Fig. 9.6c depicts the result with space charge effects. Clearly an enlargement of the cloud is observed in the z-direction due to space charge. However, the pulsed nature of the positron cloud is still clearly apparent on a nanosecond timescale.

9.4.4 Positron Pulses

A first step towards PFR is the creation of positron pulses. Since the loading time of electrons ($10^5 - 10^6$ electrons in 1 minute) is almost 40× faster than the loading time of positrons ($10^5 - 10^6$ positrons in 40 minutes), the initial experiments were performed with electrons. Electron pulses of a duration of $\sim$ 20 ns were produced when we pulsed the electron trap of Fig. 9.7a open. The duration of these pulses was measured in the following manner. An electric field ramp of 3.0 V per electrode was created at T8 and EET ($T8 = -3.0$ V, $EET = -6.0$ V) and an electron well was created at T2 ($HV = T1 = T3 = -6.0$ V, and $T2 = -3.0$ V), filled with $\sim 10^6$ electrons (see Fig. 9.7a-d). Electron pulses were created when T3 was pulsed from -6.0 V to 0.0 V. The electron pulse travels to the field ramp and bounces back to T2 due to this ramp. The calculations were used to simulate the trajectory of the pulse in order to predict the arrival time back at T2. At the moment the electron pulse reaches T2, the voltage on T3 is switched back from 0.0 V to -6.0 V, and the electron pulse is recaught. By slowly moving the electron well to ER, the number of recaught electrons could be counted. The pulse duration was measured by varying the time when the voltage on T3 is switched from 0.0 V to -6.0 V. The result is depicted in Fig. 9.7e. Note that recatch efficiencies of 80 - 90 % are obtained and that also the second and the third roundtrip in the long well are recorded. The same experiment was performed with positrons and similar recatch efficiencies were observed.

The pulse recorded after the second roundtrip has a smaller width (18 ns) and a larger maximum catch efficiency (90($\pm$3) %). This can be explained by a time and/or space

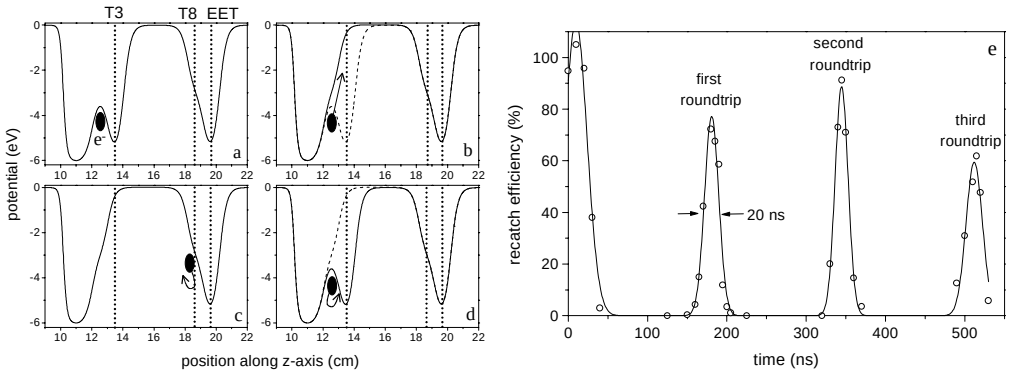

Figure 9.7: *a-d: Recatching electrons in a well at electrode T2 after they have been pulsed out of the same well. At t = 0 ns, an electron well is pulsed open such that electron pulses are created travelling towards a potential wall at electrode T8 and EET (a-b). Due to this potential wall the electrons bounce back to electrode T2, and will arrive there at a well defined time. When the electrons arrive at T2 they turn around again and the same cycle is repeated. However if the voltage on electrode T3 is raised at the right time to its original value, the electrons are recatched in T2 (c-d). e: Recatch efficiency of the above described scheme as a function of the delay time after which the voltage on electrode T3 is raised again.*

focus in between the first and second roundtrip of the pulse. After the second roundtrip the pulse defocusses again as is seen from the pulse recorded after the third roundtrip which width is 25 ns and a maximum recatch efficiency is recorded of only 60($\pm$3) %. It seems that space charge hardly has any effect on time scale of a PFR experiment with these densities, since the recorded width of the electron (positron) pulses (20 ns) is almost the same as the time it takes to open the electron (positron) trap (22 ns) and the width of the pulses hardly increases as a function of time.

The second timing experiment was performed to match the conditions in an actual PFR experiment as much as possible. Instead of bouncing the electrons (positrons) back to T2 to recatch them, the electrons were launched from T2 and caught at T8. This was done in the following way (see Fig. 9.8b): an electron well of $\sim$3.0 V deep was created at T8 ($T8 = -3.0$ V, $EET = T7 = 0.0$ V). Another electron well was created at T2 ($HV = T1 = T3 = -6.0$ V, and $T2 = -3.0$ V), filled with $\sim 10^6$ electrons. Electron pulses were created when T3 was pulsed from -6.0 V to 0.0 V. The electron pulse will travel to the field ramp, were it will decelerate and turn around. At this moment of turning, the potential on T8 and EET is switched from -3.0 V to +3.0 V, and -6.0 V to 0.0 V respectively. The electron with (almost) no kinetic energy is diabatically captured in the created potential well at T8. After the electron catch in T8, the electron cloud is transported to ER in order to count them and deduce the capture efficiency. Again electron pulses were detected and a capture efficiency of 100% was recorded, when the

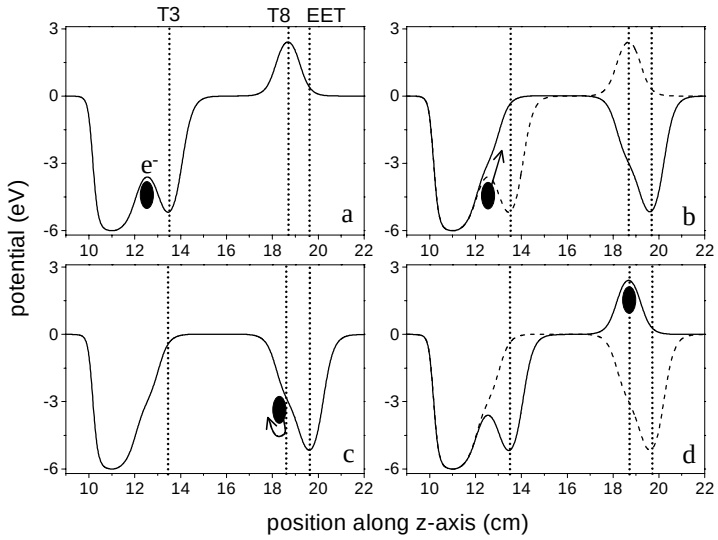

Figure 9.8: *Catching electrons in a well at electrode T8, after launcing them from a well at electrode T2. Electron pulses were created by pulsing the trap at T2 open (a-b), travelling towards electrode EET. At the same time a potential wall at electrode T8 and EET was created, so that the electron pulses would turn at T8. At the moment the electrons turn, the voltage on electrode T8 and EET is switched such that a well is created at electrode T8, diabatically catching the electrons (c-d).*

voltages on electrodes T8 and EET are switched 90 ns after the launch of the electron pulse, in perfect agreement with the predicted value of the calculations.

9.4.5 Calibrating the Electric Field in the Trap

Calibrating the electric field inside the trap is of great importance, since a residual field of 200 mV/cm will already field ionize a Rydberg state of $n = 200$. Calibrations were done with the aid of anti-protons. Anti-protons were loaded in a well at T8 in a configuration resembling as much as possible the circumstances in a PFR experiment (see Fig. 9.9a). About 10^4 anti-protons were loaded into the well at T8. If the voltage on T8 is switched from 3.0 V to 0.0 V, the trap is emptied (see Fig. 9.9b). However, if the voltage is switched from 3.0 V to some value less than 0.0 V, a long well is created from anti-protons from HV to T8 and only half of the trapped anti-protons escape from the trap (see Fig. 9.9c). The other half of the anti-protons is trapped in the long well with an energy corresponding to the potential wall height at T8. Therefore at each roundtrip of the anti-proton pulse in the long well, some anti-protons will spill out of the trap at T8. This will only happen when T8 is pulsed through 0.0 V to some negative voltage. In Fig. 9.10a-d four scintillator responses are depicted when we pulse T8 with four different amplitudes: 2.8 V, 2.9 V, 3.1 V, and 3.2 V. Clearly it is seen that if the voltage is dropped from 3.0 V to 0.1 V,

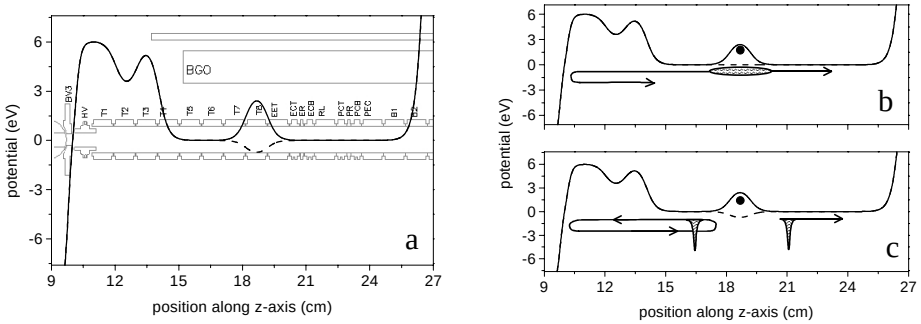

Figure 9.9: *a: Potential landscape used to calibrate the electric field at the region around electrode T8 and EET. Anti-protons were loaded in a well at electrode T8. b: When the voltage of electrode T8 is pulsed to 0.0 V for a long time (1.0 ms), the anti-proton trap is completely emptied. c: When the voltage of electrode T8 is pulsed from +3.0 V to some negative voltage, half of the anti-protons escape and half of them are captured in the long well from the HV electrode to the T8 electrode. By comparing the anti-proton detector response for different amplitudes of the voltage pulses on electrode T8, the voltage and therefore the electric field can be calibrated (see text).*

two anti-proton bursts are produced. The first burst results from anti-protons travelling directly to the degrader electrode where they annihilate. The second burst is from anti-protons first bouncing of the potential wall at electrode HV and then travelling to the degrader where they annihilate. If the voltage is dropped from 3.0 V to -0.1 V or -0.2 V, multiple anti-proton bursts are produced, which are attributed to the creation of a long well from T8 to HV. From these results it was deduced that the electric fields are known within 100 mV/cm.

9.4.6 Pulsed Field Recombination

In a typical PFR experiment 10^5 anti-protons were used and 5×10^5 positrons (density: $10^6 - 10^7$ cm^{-3}). Previous work on PFR [98, 99, 137] (Chapter six, seven, and eight), showed that the amount of recombinations can be estimated with the aid of the following formula:

$$N_{rec} = \rho_{\overline{p}}\rho_e V_{over} V_{int} \tag{9.1}$$

where N_{rec} is the number of recombinations, $\rho_{\overline{p}}$, and ρ_e the anti-proton and positron density, V_{over} the overlap volume of the anti-proton and electron cloud, and V_{int} the interaction volume. The interaction volume is defined as the volume in space in which the positron has to possess a certain velocity to get recombined. For the voltages and slew rates of the electric field pulses used in this experiment, this V_{int} is on the order of 10^{-10} cm^{-3}. If V_{over} is maximal the expected number of recombination is: $10^5 \times 10^{6-7} \times 10^{-10} = 10^{1-2}$.

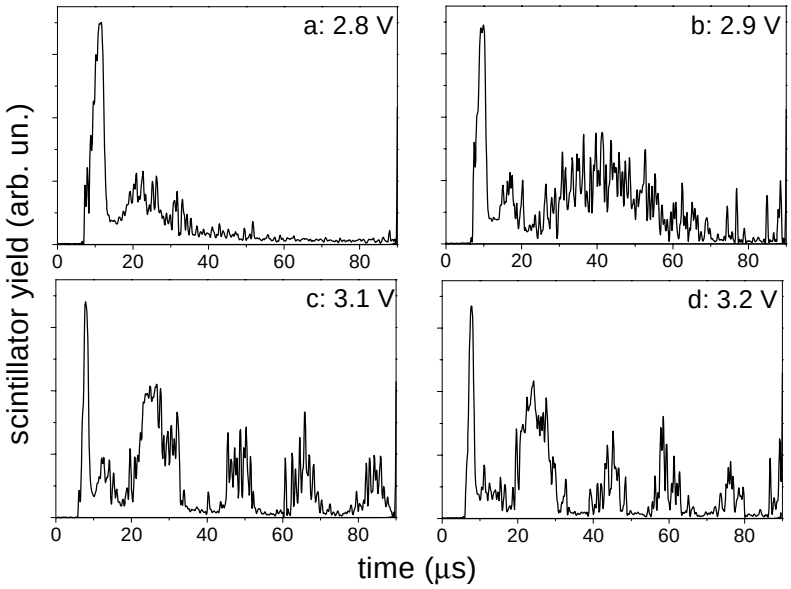

Figure 9.10: *Calibrating the electric field in the trap. Four scintillator responses when at $t = 0$ electrode T8 is pulsed from $+3.0$ V to $+0.2$ V (a), $+0.1$ V (b), -0.1 V (c), and -0.2 V (d).*

From Fig. 9.10 it is seen that approximately 8 μs after pulsing down the electric field in the region of T8 and EET in a PFR experiment, the first unrecombined anti-protons will reach the DEG electrode. At the DEG electrode these anti-protons will annihilate and contribute to a large background signal. The possibly created anti-hydrogen atoms will have an average velocity determined by the thermal velocity of the anti-protons and positrons: $v = \sqrt{2kT/m_p} \approx 300\ m/s$. The time we will expect to see signal from anti-hydrogen atoms, is the flight time of the anti-hydrogen atoms from the center of the trap to the electrode. This shortest distance is 5.0 mm, hence after $\sim 19\ \mu s$ signal can be expected. However at that time, the unrecombined anti-proton background has already appeared on the detector which makes the detection of anti-hydrogen impossible. The signal from positrons is of no concern since the scintillating fibers and the PPAC are not sensitive to positrons.

The first PFR attempt was done with the voltage configuration of Fig. 9.5. Two experiments were performed: the first with anti-protons and positrons, and the second only with anti-protons. Substraction of the signal of the second experiment from the first could reveal an anti-hydrogen signal, if the background signal is not too pronounced. In Fig. 9.11 the detected signal of these two experiments is depicted. No clear anti-hydrogen signal can be observed when the results of the two experiments are compared, possibly due to the fact that the anti-hydrogen signal is much weaker then the background signal and saturation of the detector due to the sudden "dump" of the anti-proton trap.

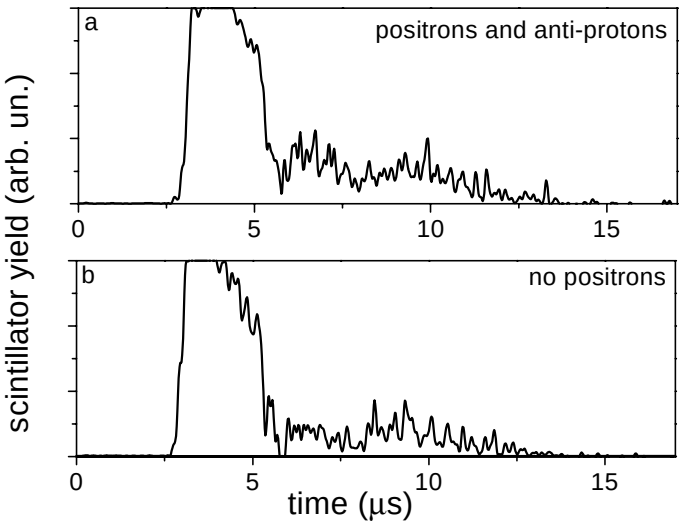

Figure 9.11: *First attempt of PFR. a: PFR scheme with positrons and anti-protons. The anti-proton annihilation yield is plotted as a function of the time after the positron launch. Anti-hydrogen signal is expected after* ~ 19 μs *(see text). b: PFR scheme without positrons, to measure the background signal.*

To circumvent this background problem, a long well was created from the HV electrode to the DEG electrode, so that after a PFR experiment the anti-protons would be trapped and do not contribute to background signal (see Fig. 9.12). The background was greatly reduced but still losses were seen from this long well: in Fig. 9.13a and 9.13b the recorded losses are plotted as a function of time after performing a PFR experiment without positrons. The amount of loss is not fully understood, but can be explained by electrode imperfections which introduce potential discontinuities. These discontinuities can be severe enough for low kinetic energy particles to kick them out of the trap.

Regardless of the losses an attempt was made to produce anti-hydrogen in this configuration. In Fig. 9.13 the results of an experiment with, and without positrons are depicted. Clearly the background is greatly reduced enabling us to digitize the analogue signal from the anti-proton detectors in order to count single anti-proton annihilation events. No statistical significant signal is observed which can be attributed to anti-hydrogen, when an experiment with anti-protons and positrons is performed. Due to the low repetition rate of an experiment (± 1 hr) it was impossible to average over multiple experiments to extract a significant anti-hydrogen signal out of the noise.

It was expected that 10^{1-2} anti-hydrogen atoms could be observed with the densities used in these experiments. The lack of signal can be explained by three limiting factors. The long well can attribute to a loss in detection since the electric fields associated with this long well are substantial enough at the outer ends of this well to field ionize the created Rydberg anti-hydrogen atoms. Therefore the well was made as long as possible to increase the solid detection angle as much as possible. If anti-hydrogen is mainly produced

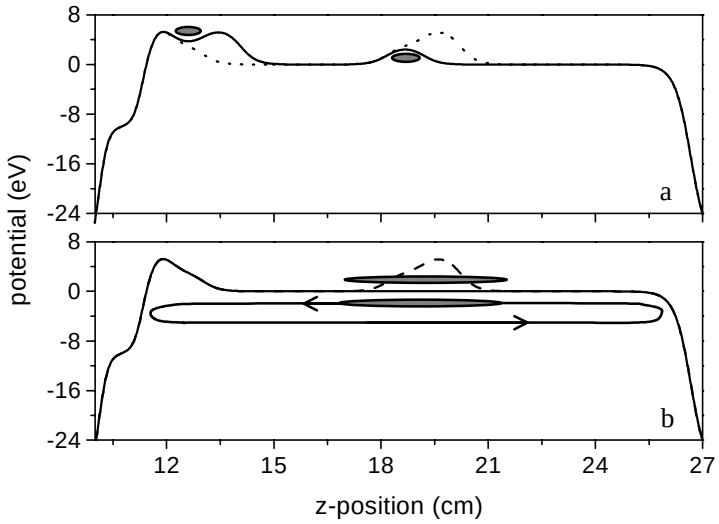

Figure 9.12: *The effect of a long well for anti-protons. Before a PFR experiment, positrons are trapped at electrode T2, and anti-protons are trapped at electrode T8 (a). After a PFR experiment, the positrons are untrapped and will give background signal on the BGO detector, but they will not be detected by the other scintillators, since these are insensitive to positrons. Due to the long well, the unrecombined anti-protons should be trapped, so that they will not attribute to a background signal.*

with a velocity along the z-axis, then the number of detected anti-hydrogen atoms will be significantly lower than our estimate. The second limiting factor is ionization by the motional Stark effect. The motional Stark field will be proportional to the velocity perpendicular to the magnetic field (z-axis). This means that the ionizing effect will be more substantial for anti-hydrogen atoms produced with a velocity directed perpendicular to the z-axis. A third limiting factor on the detection of anti-hydrogen, is that the overlap volume of the positron and the anti-proton cloud is very small, resulting in a low number of recombinations.

9.5 Future Direction

In this chapter, a report is presented in which we described the progress in the creation of anti-hydrogen at the ATRAP experiment at CERN. We have shown that positron pulses with a density of $10^6 - 10^7$ cm^{-3} can be produced of 20 ns duration from a trap, which can be caught in a spatially separated trap with 100 % efficiency. Additional experiments were performed to calibrate the electric field in a specific region in the trap. Finally, the first attempts of PFR were made with anti-protons and positrons. We were however not able to detect any created anti-hydrogen. We propose three improvements for future experiments with PFR to increase the probability of detecting anti-hydrogen.

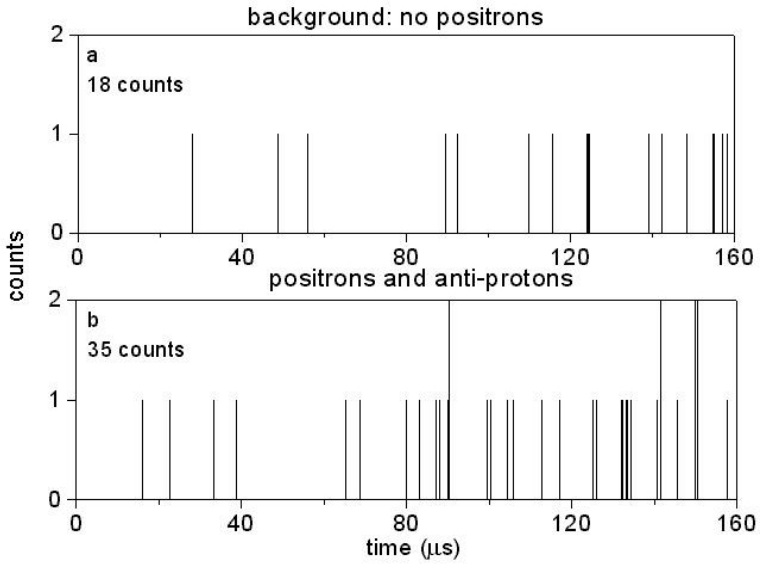

Figure 9.13: *a: Recorded losses from anti-protons, after they were launched in the long well by the PFR scheme. After 1.6 ms, 1836 counts were recorded. b: Recorded signal after performing a PFR experiment with positrons and anti-protons in a long anti-proton well configuration. After 1.6 ms, 1646 counts were recorded. Recording these traces took one night. The total number of anti-protons used in the two experiments is almost the same since after 1.6 ms a similar loss number is recorded (1836 counts vs 1646 counts)*

The first improvement would be to reduce the magnetic field strength, to reduce the motional Stark field. Classical calculations predict that the field required to ionize a Rydberg state, relates to the principal quantum number as follows:

$$v_{\perp}B = F = \frac{1}{n^4} \tag{9.2}$$

where F is the motional Stark field strength, and $v_{\perp}$ is the velocity of the (anti-)atom perpendicular to the magnetic field. Classically, the $E \times B$ term, due to the motional Stark field, gives rize to a stabilizing magnetron-like [127] orbit of the positron around the nucleus. If the radius of the magnetron orbit is larger than the position of the saddlepoint, the system ionizes. We know that $r = \frac{1}{n^2}$, and $V = \frac{1}{r} + Fz$, for an electric field in the z-directions. The position of the saddlepoint is located at: $z = \sqrt{1/F}$, and thus it can be understood that $v_{\perp}B = F = \frac{1}{n^4}$. Notice the analogue with the classical fieldionization law in the case of just the presence of an electric field (Chapter 2):

$$F = \frac{1}{16n^4}. \tag{9.3}$$

In this case ionization occurs when the (field free) binding energy of a Rydberg state is smaller than the energetic position of the saddlepoint. Thus $E = \frac{1}{2n^2}$, $V = \frac{1}{r} + Fz$,

and the location of the saddlepoint is $z = \sqrt{1/F}$. The amount of energy by which the saddle-point is lowered is: $V = 2\sqrt{F}$, leading to $F = \frac{1}{16n^4}$.

The classical calculations were based on a 2D numerical integration of the equations of motion of a positron orbiting an anti-proton in a magnetic field crossed with an electric field in the center of mass frame. The value of the electric field corresponds to the value of the motional Stark field experienced by a Rydberg atom of 4.2 K. Lowering the magnetic field to 2 T would already prevent ionization of a $n = 180$ Rydberg state (see Fig. 9.14). It is not yet clear how the lowering of the magnetic field effects the trapping efficiency of the anti-protons from the AD-ring, and this should be investigated to set a lower limit on the magnetic field strength.

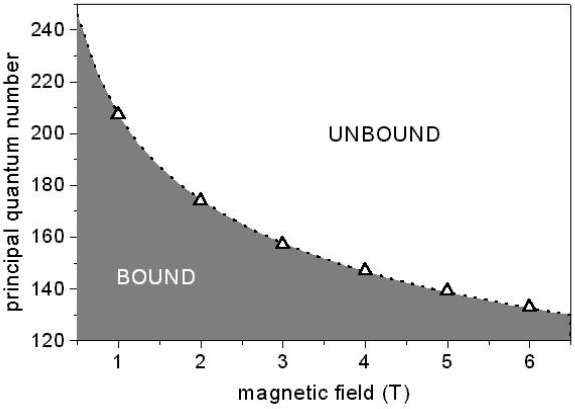

Figure 9.14: *Magnetic field required to field ionize an anti-hydrogen atom with a velocity perpendicular to the magnetic field, corresponding to the velocity of a 4.2 K particle. The open triangles represent the results from the 2-D classical calculation. The dotted line corresponds to (atomic units are used):* $v_\perp B = F = \frac{1}{n^4}$, *with* $v_\perp = \sqrt{\frac{2kT}{m}}$, *and* $T = 4.2\ K$.

It should be noted that the behavior of Rydberg atoms in crossed magnetic and electric fields at these high principal quantum numbers has not yet been investigated. The lifetime of Rydberg states which can classically ionize, could be significant, and there can even be chaotic stable states in $E \times B$ fields. In fact Wiebusch *et al.* [138] have shown that certain states surpassing the saddlepoint in $E \times B$ fields have long lifetimes. If the lifetime of the created Rydberg states is longer than the time it takes the anti-hydrogen to hit the wall, it can be detected.

The anti-hydrogen atoms with a small $v_\perp$ component, hardly experience any motional Stark effect and therefore will not ionize if the induced electric field is small enough. When a long well is used to suppress background signal, these anti-hydrogen atoms with small $v_\perp$ cannot be detected since they will field ionize when they reach the edge of the long well during their travel along the z-axis. On the other hand one could use this field ionization when the anti-hydrogen atoms reach the outer sides of the long well, to detect

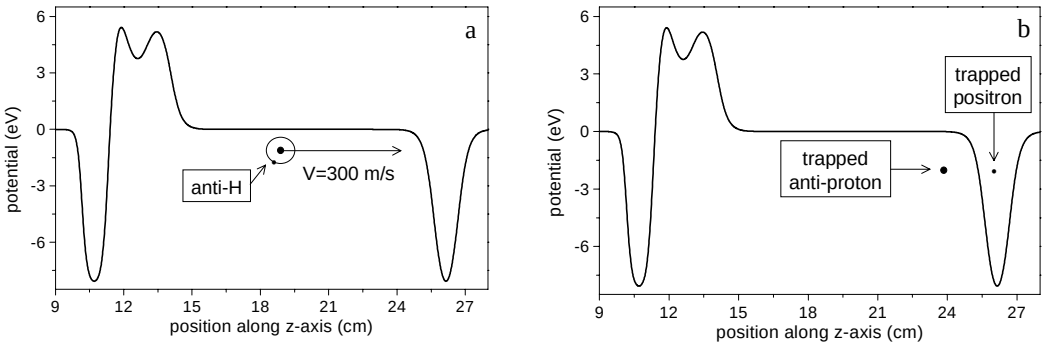

Figure 9.15: *Using a long anti-proton well to detect anti-hydrogen. If anti-hydrogen is produced with a certain velocity along the z-direction, it will reach the outer wall of the long anti-proton well after a certain time (a). Due to the electric field at this potential wall, the anti-hydrogen atom will field ionize, and the positron is captured in the positron well located on the side of this potential wall, while the anti-proton is trapped in the long well (b).*

anti-hydrogen atoms. This can be done by implementing additional wells for positrons on the two sides of the long well. Each time an anti-hydrogen atom field ionizes, the long well is filled with an anti-proton and the positron well on the side is filled by a positron (see Fig. 9.15). After all the recombined anti-hydrogen atoms have field ionized, the positron well can be transported to a harmonic region in the trap, so that the positrons can be counted.

The second improvement would be to use faster pulse generators to produce faster electric field turn offs. The interaction volume is mainly determined by the time it takes to turn off the electric field, since it has to be turned off within the orbiting period of the created Rydberg state. Therefore, a faster electric field turn off results in a state distribution with more deeply bound states and more recombinations for the same charged particle densities. Moreover, deeper bound states are less susceptible to external electric fields and thus the motional Stark effect will be suppressed.

The final improvement would be to lower the temperature of the anti-protons by sideband cooling [127, 130], as is done with the positrons, to reduce the magnetron orbit of the anti-protons. The trapped anti-protons are believed to have large magnetron radii, since a large fraction of the anti-protons do not enter the trap along the central axis of the trap. This results in a rather large cloud size. The positron cloud however, is sideband-cooled after the trapping scheme of positrons, resulting in a possible smaller cloud size then the anti-protons. If the cloud shapes differ very much, the overlap in a PFR experiment will be very small. Only during the last shift of beam time, the axial resonance of the anti-protons in a harmonic trapping potential could be detected, and thus the effect of sideband cooling of anti-protons in a PFR experiment should still be investigated.

Chapter 10

Summary

10.1 Motivation of the Research

In this thesis, the making (Chapter 6, 7, 8, and 9) and the breaking (Chapter 2, 3, 4, and 5) of Rydberg atoms is investigated. The making of an atom can often be done by the time inverse of a mechanism which breaks an atom. Breaking of atoms can be accomplished by time varying electric fields (Chapter 2), or photon fields (Chapter 3, and 4). Time varying electric fields can also be used to frustrate the breaking (Chapter 5), by diabatically switching an ionizing state of an atom into a bound state. The careful examination of the breaking or the frustrated breaking of a Rydberg atom often reveals atomic dynamics, making them ideal to construct and test (quantum) theories. In Chapter 6 we demonstrate that the time inverse of a process described in Chapter 2 (Selective Field Ionization), can be used to make a Rydberg state from a free electron and a free ion (Pulsed Field Recombination).

Making an atom by recombining an electron and a proton is not simple. The recombination is only possible when a third object carries away the excess energy of the captured electron. This third particle can be a second electron (this process is known as three-body recombination), or a photon (radiative recombination). Pulsed Field Recombination (PFR) [98, 99] can be regarded as intermediate between the radiative and the three-body process. One can say that the effect of the third body, stimulating the recombination through its time dependent electric field, is now applied "by hand" in the form of tailored pulses. In Chapter 6, 7, and 8 this novel and efficient recombination scheme is discussed in detail.

In Chapter 9 a progress report is presented on the implementation of PFR for the production of cold (4.2 K) anti-hydrogen. The experiments were performed at CERN for the ATRAP collaboration. This production of neutral anti-matter would enable the direct comparison of neutral matter with neutral anti-matter, which can be used to test CPT invariance and the Weak Equivalence Principle (WEP). To produce such cold anti-matter is the first goal of the ATRAP (Anti-hydrogen Trap) collaboration [28].

In this chapter we summarize experiments in which we use "ordinary" matter to study the recombination dynamics of the PFR scheme. Following the initial demonstration of

PFR in Rb, we continued the experiments by recombining electrons, initially trapped in a Penning trap, with Li ions. There were three major motivations for performing these experiments. To test if the PFR scheme could indeed be used to recombine lighter ions with free electrons, we have used lithium ions instead of rubidium ions, which were used in previous experiments. Lithium being 12 times lighter than rubidium resembles much more a proton, although it is still 7 times heavier. The second motivation was to study PFR in a configuration which had a greater resemblance with the ATRAP experiment at CERN, where recombination of *trapped* positrons and *trapped* anti-protons will be studied in Penning traps [108]. The last motivation was to increase the recombination efficiency of the PFR scheme.

Moreover, we propose that PFR can be used in cation spectroscopy on molecular species for which laser-excitation of a Rydberg state fails (Chapter 8). In Photo-induced Infra-Red Ionization (PIRI) spectroscopy [105–107], the cation spectrum of a molecule is recorded with the aid of a Rydberg state in that specific molecule. Most commonly, such a Rydberg state is prepared by laser-excitation. For complex molecules laser-excitation of a well defined Rydberg state can fail, so that the PIRI technique can not be applied. Recently we have shown that the PFR method can be used to recombine a free electron with a large ionic carbon cluster such as C_{60}^{+}, inducing a highly excited bound state of such a molecule ($n \approx 180$) [99]. This was the first time the existence of C_{60} Rydberg states was observed convincingly.

In addition, a theoretical description is presented with semi-classical calculations. These semi-classical calculations give deeper insight on the states which are being formed in the recombination process and can be used to probe recombination dynamics not probed by the experiments.

10.2 Scheme and Efficiency

In Fig. 10.1 the PFR scheme is sketched. An ion is situated in a static electric field that modifies the Coulomb potential such that a saddle point is created (Fig. 10.1a). If an electron passes over the saddle point in the modified Coulomb potential, it will take a small, but not negligible, amount of time to return to the saddle point and escape from the ion (Fig. 10.1a). If the static field is turned off (Fig. 10.1b) before the electron returns to the saddle point, it will remain bound in a highly excited state (Fig. 10.1c). The time required for the electron to travel from the saddle point, to the nucleus, and back to the saddle point is about 1 ns for the fields and energies used in these experiments. This time is comparable to the turn off time of the static electric field (90% $\rightarrow$ 10% in 0.8 ns). In Fig. 10.1d the experimentally determined efficiency (number of recombined atoms divided by the number of free ions) of this scheme is depicted as a function of the delay of the fast field turn off. This delay is with respect to the time when the free electron has its turning point in the electric field. Clearly, a maximum number of recombination events is recorded at zero delay. A comparison with previous experiments with rubidium ions shows that the efficiency (3.0×10^{-3} [98], Chapter 6) has gone up by almost an order of

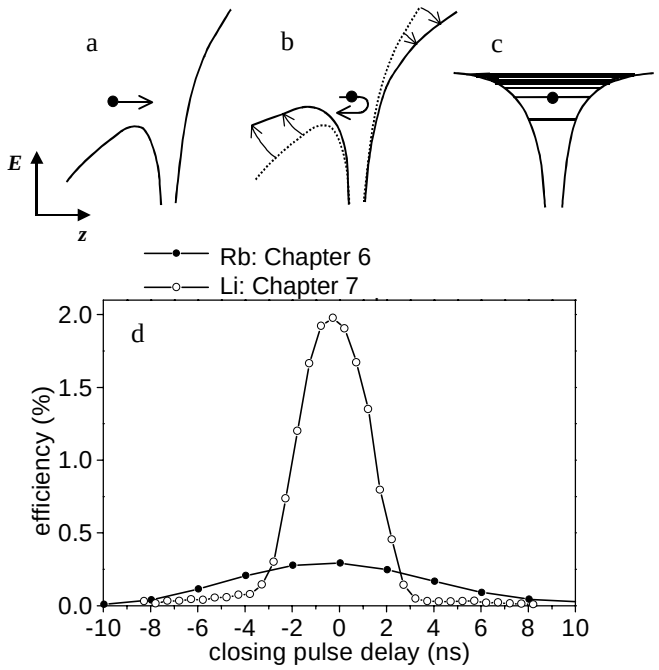

Figure 10.1: *(a-c): Schematic representation of the Pulsed Field Recombination scheme (see text). (d): Experimentally observed efficiency as a function of the delay of the quick turnoff. The open circles represent recombination of free electrons and lithium ions with the use of an electron trap (Chapter 7). The solid circles represent data where we studied recombination of free electrons and rubidium ions in a trapless geometry (Chapter 6).*

magnitude (2.0×10^{-2}, Chapter 7) and that the electron pulses are much shorter. The increase in efficiency is mainly due to the fact that the electron pulses are shorter in time (from 11 ns [98] to 3.8 ns) and that we had better control over the overlap volume of the ion cloud and the volume of the electron pulses. We achieved the highest efficiency (6%) so far when we used the PFR scheme to recombine free electrons with free ionic carbon clusters in a trapless environment [99]. Note that we have shown that PFR can be used in the geometry of *trapped* electrons and *light* ions.

10.3 Experimental

We have used two different setups to study Pulsed Field Recombination. With the first setup we have studied recombination with rubidium ions (Chapter 6) and recombination with ionic carbon clusters (Chapter 8). The second setup (Chapter 7) was designed to mimic as closely as possible the conditions under which anti-protons and positrons should be recombined at CERN to produce cold anti-hydrogen. The essential difference between the setups is the electron source. For the initial experiments (Chapter 6, and 8) we used

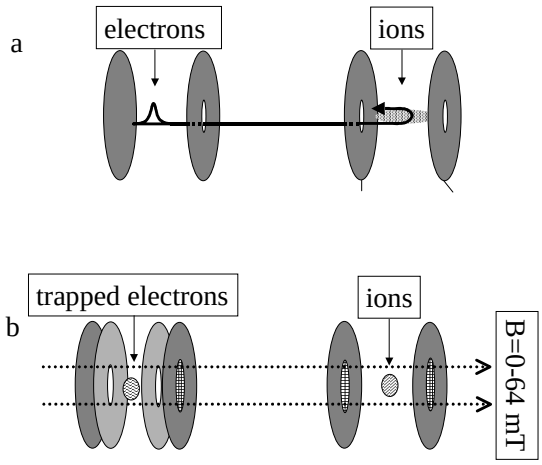

Figure 10.2: *Sketch of the two experimental setups used to study PFR. a: The setup with which we studied recombination of free electrons with Rb^+ and with C_{60}^+. b: The setup with which we studied recombination of free electrons, originated from an electron trap, with Li^+.*

photoelectrons, while the later experiments were performed with electrons from a Penning trap.

10.3.1 Photoelectron Setup

In the first setup a pulsed electron source was created by photoionizing lithium atoms in a small static electric field with a dye laser. Typically electron pulses of 11 ns duration, with about 10^4 electrons in a volume of 0.02 mm^3 were produced. In another region a cloud of ions is awaiting the electrons. Typically 10^3 Rb-ions were produced in a volume of 2.0 mm^3. The rubidium ions were produced by photoionizing rubidium atoms in a static electric field of 1.50 V/cm, 50 ns before the lithium atoms were ionized, in a two-photon process. The configuration is depicted in Fig. 10.2a.

The ionic carbon clusters were produced by photoionizing and fragmenting gas-phase C_{60} molecules in a static electric field. The photoionization mainly produces the higher ionic carbon clusters. The ionic carbon cloud resembles a cylinder with a radius of 35 μm in the z-and y-direction and a length of 10 mm in the x-direction, with about 10^3 ions.

In the ion source region the electrons are decelerated by the electric field of 1.50 V/cm, and have their turning point at the position of the ion cloud. At that time the field is turned off by dipping the voltage on the cathode plate from -1.50 V to -0.20 V. The electric field turn off is realized by connecting an impedance matched, fast pulse generator to the cathode plate.

10.3.2 Penning Trap Setup

The second setup was designed to mimic as closely as possible the ATRAP experiment at CERN, where one will study recombination of *trapped* positrons and *trapped* anti-protons in Penning traps [108]. In this setup we studied recombination starting out with trapped electrons and free ions. We have used SIMION [139] to calculate the shape of the potential well, created by a specific set of electrodes, in order to design a plate configuration which produces as much as possible a harmonic potential in order to mimic the conditions of the ATRAP setup at CERN.

In these experiments we filled an electron trap by photoionizing gas-phase lithium atoms. By connecting a fast pulse generator on one of the electrodes the voltage could be switched. This enabled us to empty the trap at any time and produce electron pulses of 3.8 ns duration. Care was taken for correct impedance-matching of the pulse generator to the trap electrode. We could fill the trap with about $10^5 - 10^6$ electrons and the recorded lifetime was about 1.5 ms depending on the background pressure (10^{-6} Torr).

Lithium ions were produced 3 cm away from the electron trap by using ionizing laser light. Typically we would produce a cylindrically shaped ion cloud containing $10^2 - 10^3$ ions, with a diameter of 2 mm and a length of 10 mm. The last plate was connected to a fast pulse generator which could ramp the voltage down from -1.5 V to any voltage in between -1.5 V and + 1.0 V within 0.8 ns. Again care was taken to match the impedance of the parallel capacitor plate to the output of the fast pulse generator. The whole plate configuration was placed in the heart of 2 coils in the Helmholtz configuration producing a tunable magnetic field of $0.0 - 64.0$ mT. The plate configuration is depicted in Fig. 10.2b.

In all the experiments a small static electric field is present in this region of 200 mV/cm to ensure that any unrecombined free electron is accelerated out of this region and to prevent the effect of "trapping" the electrons in the attractive potential of the ion cloud. For the volumes and densities used in the experiments, the electrons feel an attractive field of <10 mV/cm at the edge of these volumes. Such a low density plasma is therefore not stable when the ion region is biased with an electric field of 200 mV/cm. The experiments were performed in a vacuum chamber with a background pressure of 5×10^{-7} Torr.

The recorded efficiency was almost an order of magnitude higher in this setup compared to the photoelectron setup (see Fig. 10.1d), but the disadvantage is that a Penning trap requires a magnetic field. In the experiments performed in this setup, the maximum fieldstrength was 64.0 mT, while at the ATRAP experiment at CERN the magnetic field-strength in the Penning trap is as high as 6 T. In Chapter 9 we discuss how such a strong magnetic field might perturb the production of anti-hydrogen by PFR.

10.4 Recombination of Lithium and Rubidium

Timing is essential in a PFR experiment. This can be seen in Fig. 10.1d: if we turn off the static electric field before the electrons reach the ions halfway between the parallel capacitor plates, the electrons will hardly be slowed down and will pass the ions without

being recombined. If we turn off the static electric field too late the electrons will turn around at the ions but will gain kinetic energy again due to the static electric field and will leave the ion region in the opposite direction without being recombined. If we turn off the static electric field at the moment the electrons turn and overlap with the ions, we record a maximum recombination efficiency of 2.0 %. From Fig. 10.1d we also retrieve the time profile from the electron pulses since we record a Guassian profile with a width of 3.8 ns (solid line) which means that we have created electron pulses of 3.8 ns. In this case the electron pulses are produced by pulsing open the electron trap in 0.8 ns and therefore one can expect that electron pulses are created of 0.8 ns (Chapter 7). The fact that the pulse duration is 6 times longer is mainly due to Coulomb repulsion which results in an enlargement of the electron cloud. The enlargement of the electron cloud is mainly restricted in the z-direction since the presence of the magnetic field prevents the cloud from blowing up in directions perpendicular to the z-axis. This, in turn, will result in different travelling times towards the ions and therefore a broadening of the time duration of the electron pulses. Note that this time duration of the electron pulses is much shorter than in the experiments with Rb (Chapter 6) where the (photo-)electron pulse duration was limited by the duration of the laser pulses ($\sim$ 10 ns), and that PFR works for both heavy (Rb) ions as for light (Li) ions.

A free electron is most likely to get recombined with the PFR scheme when it is close to the nucleus with zero kinetic energy, but the coordinates (for a certain fixed distance to the ion) of the electron relative to the ion do not play an essential role. This means that it is not appropriate to characterize PFR with a cross section as it is with most other recombination processes. Therefore we introduced an interaction volume (V_{int}, a thorough discussion of V_{int} is given in Chapter 7) to describe the observed efficiency, which is the volume in space around the ion in which the electron has to be with a certain velocity to be recombined. A simple formula then predicts what this V_{int} should be:

$$N_{rec} = \rho_e \rho_{ion} V_{over} V_{int} \tag{10.1}$$

where N_{rec} is the number of recorded atoms (10), ρ_e is the electron density in the electron pulses, ρ_{ion} is the ion density ($10^4 - 10^5$ cm^{-3}), and V_{over} is the overlap volume of the electron cloud and the ion cloud. The size of V_{over} is determined by the smallest cloud: in our case the electron cloud. We thus obtain a V_{int} on the order of 10^{-10} cm^{-3}. Such an interaction volume would correspond to a Rydberg state around $n \approx 180$. We therefore believe that high Rydberg states are produced around $n \approx 180$, by means of the PFR scheme.

To verify this hypothesis we used the technique of Selective Field Ionization (SFI), as discussed in Chapter 2, to probe the bound state distribution after the recombination event. Every bound state in an atomic or molecular system has a static electric field associated with it by which it will be ionized. A highly excited state will be ionized by a relative small electric field compared to a more deeply bound state. The relation between the value of the electric field at which field ionization classically occurs and the principal

quantum number n is (in atomic units):

$$F = (\frac{E}{2})^2 = \frac{1}{16n^4}. \tag{10.2}$$

If one ramps the static electric field in time and monitors at which time ionization occurs one can deduce the bound state distribution of an atomic or molecular system. In Fig. 10.3a a SFI trace is depicted of the recombined states when during the recombination event the electric field in the ion region is switched from 3.0 V/cm to 0.20 V/cm in 0.8 ns (solid triangles). The SFI detection started 1.4 μs after the recombination event. Clearly it is seen that we mainly produce states which are ionized by the lowest SFI fields. If we use equation(10.2) to determine which bound states we have produced we indeed observe that we are making Rydberg states with a principal quantum number around $n\approx$ 180, in perfect agreement with the principal quantum number we estimated from our observed efficiency and the V_{int} deduced from it.

A numerical estimate of V_{int} is obtained by solving Newton's equations to determine the bound state distribution after a PFR experiment. An interaction volume of $0.25 \times 10^{-10}\text{cm}^3$ is found. Using the obtained state distribution ($< n >$ = 180 with $\Delta n = \sqrt{< n^2 > - < n >^2}$ = 20) the SFI trace is calculated (using the Landau-Zener approximation, Chapter 2) and a very good agreement between theory and experiment is observed (Fig. 10.3a, thin line).

10.5 Recombination of Carbon Clusters

The efficiency we obtained when ionic carbon clusters are recombined with free electrons with the PFR scheme (Chapter 8) was as high as $6(\pm 4) \times 10^{-2}$ [99]. Typically we detected about 15 recombined molecules. The fact that in this experiment the highest efficiency was recorded, is attributed to an optimal overlap volume of the electronic and ionic clouds, and the inertia of the large molecular ions (a C_{60}^+ ion is 720 times heavier than a proton). From the achieved efficiency we again conclude with the help of equation (10.1) that we are producing high Rydberg states around $n \approx 200$.

In Fig. 10.3b, the Rydberg state distribution after recombination with PFR is depicted for recombination of the carbon clusters (C_{50} - C_{60}), showing that the state distribution peaks for small SFI fields, and thus for very high Rydberg states. Since the 1 ns turn off reduces the electric field to 0.2 V/cm, states with a principal quantum number beyond $n = 200$ are not stable. From Fig. 10.3b, it is deduced that Rydberg states are produced around n = 190. The calculation depicted in Fig. 10.3b shows a direct comparison between theory and experiment, and clearly good agreement is obtained. To obtain this level of agreement, the polarizability of the ionic carbon clusters and autoionization of the recombined carbon clusters is included in the theory. Autoionization of the Rydberg states by the interaction of the Rydberg electron with the hot C_{60}^+, is included through a model that allows the electron energy to change every time the recombined electron gets close to the core. When the electron gets within 5 atomic units of the ionic core, it receives

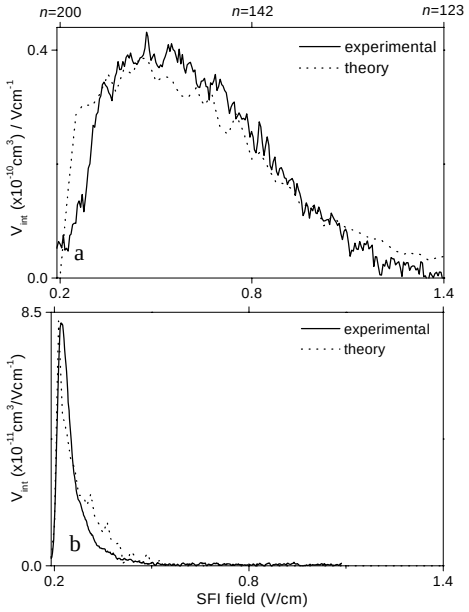

Figure 10.3: *a: Calculated state distribution (dashed line) of the recombined Rydberg atoms compared to the experimental state distribution (solid line). The experimentally determined interaction volume ($(1.0 \pm 0.7) \times 10^{-10}$ cm^3) is varied within its error to optimize the comparison with theory ($V_{int} = 0.3 \times 10^{-10}$ cm^3). b: Calculated state distribution (dotted line) of the recombined Rydberg clusters, compared to the experimental state distribution (solid line). The experimentally determined interaction volume is varied within its uncertainty to optimize the comparison with theory.*

a kick in a random direction so that the energy of the electron is just as likely to increase as to decrease. If the kick increases the energy, the electron leaves (autoionization). If the kick decreases the energy, the electron will be in a lower Rydberg state. For this deeper bound state the time to return to the C_{60}^+ decreases, so the electron will rapidly get kicked again. This is like a random walk where the time between steps decreases in one direction and the time between steps increases in the other direction. The resulting V_{int} from this calculation is 0.7×10^{-11} cm^3, in good agreement with the experimental observation: $(1.3 \pm 1.2) \times 10^{-11}$ cm^3. From the calculation follows that $\sim 75\%$ of the originally recombined electrons are ejected before the SFI detection.

10.6 Anti-Hydrogen

In Ref. [94] a combined trap is described, where typically $> 10^5$ protons and 10^6 electrons (corresponding density: 10^8 cm^{-3}) were detected in the combined trap. At CERN, the ATRAP collaboration employs such a trap to confine positrons and anti-protons with similar particle numbers. Implementing PFR in such a configuration and if the overlap

volume is maximal (the anti-proton plasma takes up the same volume as the positron plasma), the positron density is $10^7 - 10^8$ cm^{-3}, and the number of trapped anti-protons is 10^5, our scheme can produce $10^2 - 10^3$ recombined anti-hydrogen atoms in a single experiment (assuming the same V_{int} as is observed in our measurements). The exact implementation of PFR for the experimental realization of atomic anti-hydrogen production is the topic of Chapter 9. In that chapter we describe recent advances of the production of cold anti-hydrogen by PFR at CERN for the ATRAP collaboration. Pilot studies were performed demonstrating a method to calibrate the electric fields in the trap, and demonstrating that positrons pulses with a time duration of ~ 20 ns can be made from a trap. Unfortunately, the first attempts to produce anti-hydrogen with PFR in the ATRAP configuration did not succeed. Possible explanations, and future directions are given in Chapter 9. In 2001 new attempts will be made to produce cold anti-hydrogen with PFR at CERN.

10.7 Conclusions and Outlook

A detailed study of the Pulsed Field Recombination scheme is presented in which we have shown that PFR is an universal method to recombine a free electron with any sort of ion. Therefore we propose that PFR can be used in the pursuit of the production of cold anti-hydrogen.

Moreover, we have shown that PFR can be used to create a Rydberg state in a large carbon cluster such as C_{60}. The recombination dynamics for these large molecules was shown to be the same, but the survival- and SFI-detection-dynamics differ. A simple model, including autoionization is presented to understand the survival dynamics. We propose that PFR can be used for cation spectroscopy.

Chapter 11

Samenvatting

11.1 Maken en breken van Rydberg atomen

In dit proefschrift wordt onderzocht hoe een atoom opbreekt in een elektron en een ion (ionizatie) en hoe een atoom gemaakt kan worden uit een ion en een elektron (recombinatie). Hiervoor wordt het Rydberg atoom gebruikt. Een Rydberg atoom is een atoom waar één van de elektronen zich in een (hoog) aangeslagen toestand bevindt (zie Hoofdstuk 1.2). In de eerste helft van dit proefschrift (Hoofdstukken 2-4) wordt verslag gegeven van verschillende ionizatie methodes van een Rydberg atoom. Terwijl in de tweede helft een nieuwe manier wordt geintroduceerd om een elektron en een ion te recombineren tot een Rydberg atoom. Deze recombinatie methode heeft als hoofddoel om neutrale antimaterie (antiwaterstof) te maken.

Het opbreken van Rydberg atomen wordt veelal gerealiseerd met behulp van lasers. Lasers kunnen extreme eigenschappen hebben. Er zijn bijvoorbeeld nauwbandige lasers die licht produceren van vrijwel één kleur, maar met een lange pulsduur. Er zijn ook ultra-snelle lasers met een zeer korte pulsduur, maar waarvan de kleur allerminst gedefinieerd is ("breedbandige" laser). De nauwbandige laser wordt ingezet als we de energie niveaus van een atoom nauwkeurig willen bepalen of een goed gedefiniëerde Rydberg toestand in een atoom willen exciteren. De ultra-snelle laser wordt ingezet als de atomaire respons na de excitatie van een atoom als functie van de tijd wordt bestudeerd. De pulsduur van een ultra-snelle laser moet kort zijn omdat de atomaire dynamica vaak zeer snel is (in het picoseconde, 10^{-12} s, regime). Vervolgens moet er ook de beschikking zijn over een detectie mechanisme met afdoende tijds-resolutie. In Hoofdstuk 4 worden experimenten beschreven waar een ultra-snelle detector (de "atomic streak camera") wordt ingezet om op picoseconde schaal te meten hoe een atoom uit elkaar valt door excitatie met een ultra-snelle laser. Deze informatie wordt vergeleken met de informatie verkregen uit experimenten waar het energie spectrum van het betreffende atoom werd opgemeten met een nauwbandige laser. Zodoende werden (nieuwe) inzichten over de atoom dynamica verkregen.

Het elektron in zijn gebonden toestand wordt bij het ion gehouden door het aantrekkende elektrische veld van de twee tegengesteld geladen deeltjes. Het is dus niet verassend dat

een extern elektrisch veld deze binding kan beinvloeden. In de experimenten beschreven in dit proefschrift gebruiken we veelal tijds-afhankelijke elektrische velden om aangeslagen toestanden van een atoom te karakteriseren. Dit is mogelijk omdat er een eenduidige relatie bestaats tussen de sterkte van het elektrische veld dat nodig is om het aangeslagen atoom op te breken en in welke aangeslagen toestand het atoom zich bevindt. Deze karakterisatie staat bekend onder de naam "Selective Field Ionization" (Hoofdstuk 2). Ook wordt er verslag gegeven (Hoofdstuk 5) van een experiment waar wordt aangetoond dat snelle elektrische veld pulsen het opbreken van een atoom kunnen verhinderen.

Het tweede helft van het proefschrift (Hoofdstukken 6-9) handelt over het in elkaar zetten van een atoom uit een elektron en een ion. Dit proces heet recombineren (zie ook Hoofdstuk 1.5). Wederom wordt gebruik gemaakt van een tijds-afhankelijk elektrisch veld. Het blijkt dat een vrij elektron en een vrij ion kunnen worden gerecombineerd als we een ion in een elektrisch veld zetten en het veld snel uit zetten op het moment dat een elektron met zeer weinig snelheid het ion tot zeer dichtbij is genaderd ($< 1\ \mu m$). In Hoofdstuk 6-8 wordt met behulp van diverse experimenten deze nieuwe en efficiente recombinatie methode toegelicht. De methode werd succesvol toegepast op rubidium ionen (Hoofdstuk 6), lithium ionen (Hoofdstuk 7) en grote moleculaire ionen (het C_{60} molecuul, Hoofdstuk 8). Verondersteld wordt dat de nieuwe recombinatie methode ingezet kan worden om elk soort atoom (molecuul) te maken uit een electron en een (moleculair-)ion en dus ook een anti-atoom te fabriceren uit een anti-elektron (positron) en een anti-proton. Hoofdstuk 9 beschrijft de eerste pogingen om neutrale antimaterie te maken door een positron en een anti-ion (anti-proton) met behulp van de nieuwe methode te recombineren. In de rest van deze samenvatting wordt de motivatie voor het maken van neutrale antimaterie toegelicht.

11.2 Wat is antimaterie?

Voor elk elementair deeltje bestaat er een antideeltje met een tegengestelde lading. Als een antideeltje op een deeltje botst blijft er niets over, behalve een hoop stralingsenergie volgens Einstein's $E=mc^2$. Het bestaan van antimaterie werd 'ontdekt' door Dirac toen hij in 1928 bezig was met het formuleren van zijn versie van de quantummechanica. Uit zijn theorie volgde het bestaan van anti-elektronen die om historische redenenen positronen worden genoemd. Zoals atomen zijn opgebouwd uit protonen, neutronen (of op nog fundamenteler niveau: quarks) en elektronen, zo zijn anti-atomen samengesteld uit antiprotonen, antineutronen en positronen.

Tegelijkertijd met Schrödinger en Heisenberg was Dirac bezig met zijn formulering van de quantumtheorie. Dirac was echter van mening dat zijn quantumtheorie moest voldoen aan Einsteins speciale relativiteitstheorie: de theorie moet de juiste energie-impulsrelatie voorspellen: $E^2 = m_0^2c^4 + p^2c^2$ en invariant zijn onder een Lorentz-transformatie. Deze theorie leverde twee opmerkelijke voorspellingen op: het bestaan van elektron-spin en van antimaterie. Hieronder wordt de theoretische afleiding geschetst die tot deze laatste conclusie leidt.

11.2 Wat is antimaterie?

De twee basisprincipes van de quantummechanica zijn de quantisatie van het electromagnetisch veld en het golfkarakter van deeltjes:

$$E = \hbar\omega \text{ en } p = \hbar k \text{ met } k = \frac{2\pi}{\lambda}.$$

De niet-relativistische uitdrukking van de energie van een vrij deeltje is:

$$E = \frac{\mathbf{p}^2}{2m}. \tag{11.1}$$

De golffunctie wordt gegeven door een vlakke golf:

$$\psi(\mathbf{r}, t) = e^{i(\mathbf{k}\times\mathbf{r}-\omega t)}. \tag{11.2}$$

We eisen nu dat de golffunctie een eigenfunctie is van de energie- en de impulsoperator ($\widehat{\mathbf{E}}$ en $\widehat{\mathbf{p}}$):

$$\widehat{\mathbf{E}}\psi = E\psi \equiv \hbar\omega\psi \text{ and } \widehat{\mathbf{p}}\psi = \mathbf{p}\psi \equiv \hbar\mathbf{k}\psi.$$

Dan moeten de operatoren de volgende vorm hebben:

$$\widehat{\mathbf{E}} = i\hbar\frac{\partial}{\partial t},\ \widehat{\mathbf{p}} = -i\hbar\nabla. \tag{11.3}$$

Gebruikmakend van vgl. 11.1, 11.2 en 11.3 geeft de Schrödinger-vergelijking van een vrij deeltje:

$$i\hbar\frac{\partial\psi}{\partial t} = \frac{-\hbar^2}{2m}\nabla^2\psi.$$

Als we echter beginnen met de relativistische energie van een vrij deeltje:

$$E^2 = p^2c^2 + m_0^2c^4$$

verkrijgen we, gebruikmakend van vgl. 11.2 en 11.3, de Klein-Gordon-vergelijking:

$$\hbar^2\frac{\partial^2\psi}{\partial t^2} - \hbar^2c^2\nabla^2\psi + m_0^2c^4\psi = 0.$$

Als we nu weer een vlakke golf als representatie van een vrij deeltje gebruiken, krijgen we:

$$(-\hbar^2\omega^2 + c^2\hbar^2\mathbf{k}^2 + m_0^2c^4)\psi = 0 \implies E \equiv \hbar\omega = \pm\sqrt{c^2\mathbf{p}^2 + m_0^2c^4}. \tag{11.4}$$

Dit resulteert in twee sets golffuncties: $\psi_+ \propto e^{-i\omega t}$ met een positieve eigenwaarde van de energie (en een minimum waarde van $+m_0c^2$) en een set golffuncties: $\psi_- \propto e^{+i\omega t}$ met een negatieve eigenwaarde van de energie (en een maximum waarde van $-m_0c^2$). Diracs interpretatie was nu dat deze negatieve-energietoestanden wel degelijk bestaan,

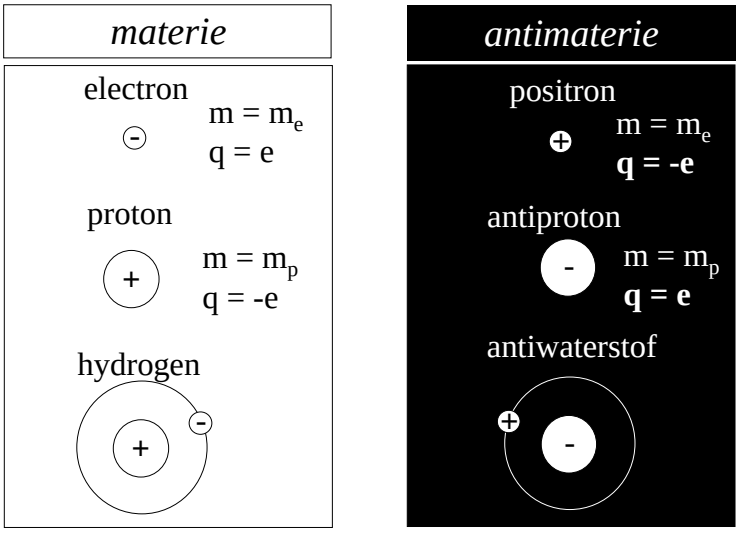

Figure 11.1: *Schematische weergave van waterstof, antiwaterstof en hun bouwstenen.*

maar dat deze alle gevuld zijn met elektronen. Pauli's uitsluitingsprincipe zorgt ervoor dat elektronen met positieve energie niet kunnen vervallen in een reeds bezette negatieve-energietoestand. Twee γ-fotonen met een gezamenlijke energie van $E = 2\sqrt{m_0^2c^4}$=1.02 MeV kunnen een negatieve-energietoestand exciteren naar een positieve-energietoestand. Er blijft dan een "gat" achter in deze negatieve-energietoestand. Dit gat wordt geïnterpreteerd als een elektron met positieve lading: het antideeltje van het elektron, het positron. Kort na Diracs formulering (1928), werd het eerste positron waargenomen door Carl Anderson (1931) [21, 22].

In halfgeleider-fysica wordt Diracs uitleg van de negatieve-energietoestanden nog steeds met groot succes toegepast. In deeltjesfysica heeft de verklaring het nadeel dat deze niet toegepast kan worden op bosonen, waar het Pauli-uitsluitingsprincipe niet voor geldt, terwijl bosonen en antibosonen wel degelijk bestaan.

Na de theoretische voorspelling van antimaterie (1928) en de ontdekking van positronen, werd in de jaren vijftig het antiproton waargenomen (en niet veel later het antineutron). Het werd toen pas mogelijk om een voldoende grote hoeveelheid energie te maken (0.9 GeV) voor dit deeltje met grote massa. De ingrediënten voor antiwaterstof ($\bar{\mathrm{H}}$), de gebonden toestand van een antiproton en een positron (zie Fig. 11.1), zijn dus al geruime tijd aanwezig. Toch heeft het tot 1996 geduurd totdat de eerste 9 antiwaterstofatomen zijn waargenomen bij CERN [26, 92]. Dit vormde het eerste experimentele bewijs voor het bestaan van neutrale atomaire antimaterie in het universum.

Om experimenteel te onderzoeken in hoeverre atomaire antimaterie zich als materie gedraagt, is in 1997 het ATRAP-project [28] bij het CERN in Genève van start gegaan. In dit project, dat wordt geleid door prof. G. Gabrielse van de Harvard Universiteit, werken

9 internationale onderzoeksgroepen samen, waaronder atoomfysici van de Universiteit van Amsterdam en het AMOLF. De ATRAP-samenwerking heeft als eerste doel zeer koude ($T \sim 4$ K) antiwaterstofatomen te maken en deze op te sluiten in een magnetische val.

11.3 Wat maakt antiwaterstof interessant?

Het maken en invangen van atomaire antimaterie is eigenlijk een moderne vorm van alchemie. De waarneming van de eerste negen antiwaterstofatomen in 1996 deed veel stof opwaaien. Niet zozeer omdat er veel geëxperimenteerd kon worden met die deeltjes (ze vlogen met relativistische snelheid tegen de wand) maar omdat er een nieuwe vorm van materie was gemaakt. Nog interessanter zou het zijn om deze anti-atomen voor langere tijd in het laboratorium beschikbaar te hebben, b.v. door ze af te koelen en wandvrij op te sluiten in een magnetische fles. Dat geeft de mogelijkheid om werkelijk iets te meten aan antimaterie.

Hoe gedraagt antimaterie zich bijvoorbeeld onder invloed van de zwaartekracht? Volgens het equivalentie-principe van Einstein (algemene relativiteitstheorie) is er geen verschil tussen de invloed van de zwaartekracht op een deeltje en zijn complementaire antideeltje. Dit principe voorspelt immers dat een (anti)deeltje in vrije val zich precies zo gedraagt als wanneer er geen invloed van de zwaartekracht is. Verschillende versies van het Equivalentie Principe worden gebruikt, die zich beperken tot verschillende soorten fenomenen. Het "Zwakke Equivalentie Principe" beperkt zich tot mechanische grootheden en voorspelt dat alle materie dezelfde zwaartekrachtsversnelling ondergaat. Om experimenteel vast te stellen hoe goed het equivalentie principe opgaat, is geen gemakkelijke opgave. Voor ballistische experimenten (laat antimaterie vallen en kijk naar de verplaatsing als functie van de tijd) is koude (laag-energetische) antimaterie nodig die tot nog toe alleen geproduceerd is in geladen vorm. Een zwaartekrachtsexperiment met geladen deeltjes is echter extreem gevoelig voor elektrische velden en experimenteel nauwelijks uit te voeren. De zwaartekracht op een antiproton wordt bijvoorbeeld al gecompenseerd door een elektrisch veld van 10^{-9} V/cm. Een ballistisch experiment met neutrale materie, zoals een koud antiwaterstofatoom, maakt het mogelijk om de zwaartekracht te bepalen zonder storende invloeden van elektromagnetische krachten.

Een andere belangrijke vraag is of de energieniveaus van een anti-atoom dezelfde zijn als die van gewoon waterstof. Als het antwoord op deze vraag bevestigend is dan ondersteunt dit het zogeheten CPT-invariantieprincipe. Volgens dit principe is elk fysisch proces invariant onder de gecombineerde operatie van ladingsconjugatie (C), pariteitsinversie (P), en tijdsomkering (T). Ladingsconjugatie is de operatie die een deeltje transformeert in zijn antideeltje. Pariteitsinversie is de operatie die een systeem inverteert door de oorsprong van het coördinaatsysteem. Tijdsomkering koppelt een proces aan het proces verkregen door terug te lopen in de tijd. Eigenlijk is het beter te spreken van bewegingsomkering. De nauwkeurigste test van CPT-invariantie tot nu toe is de vergelijking van de massa's van het K^0 meson en zijn antideeltje. Op grond van deze metingen kan worden geconcludeerd dat CPT-invariantie voor mesonen behouden is tot op op een ongelofelijke precisie van

10^{-18}. Voor leptonen (vergelijking van e^+ en e^-) is de bereikte precisie 10^{-12}. De beste CPT-tests voor baryonen hebben nu een nauwkeurigheid van $< 10^{-10}$, en zijn gebaseerd op het vergelijken van de verhouding van lading en massa van het proton (p) en het antiproton ($\overline{p}$) [140] en het H^--ion en het antiproton [141].

De energieniveaus van het H-atoom zijn buitengewoon nauwkeurig te bepalen met behulp van laserspectroscopie. Dit geldt in het bijzonder voor de meting van de frequentie van de 1S-2S twee-foton overgang die mogelijk is met een meetnauwkeurigheid van 10^{-14} [27]. Door metingen aan deze overgang kan zeer precies worden vastgesteld of de spectra van waterstof en anti-waterstof samenvallen, waardoor een verbeterde CPT-test voor baryonen mogelijk is.

Men zou zich kunnen afvragen waarom het vergelijken van het spectrum van een waterstofatoom met zijn antideeltje eigenlijk een CPT-test is. Immers het vervangen van een deeltje door zijn antideeltje gebeurt per definitie door de operatie C. Waar komen die P en T operaties dan tevoorschijn. Het antwoord is ongeveer als volgt: Stel we beginnen met een waterstofatoom in een magnetisch veld en we gebruiken een circulair (σ^+) gepolariseerde laserbundel om een optische overgang te maken (in dit geval verandert het magnetische quantumgetal met $+1$). Als we nu op dit hele experiment in gedachten de operatie C toepassen verandert niet alleen het H-atoom in zijn antideeltje maar ook het magneetveld keert van teken om, omdat de elektronen in de magneetspoel vervangen worden door positronen. Als we vervolgens de operatie T toepassen staat het magneetveld weer in de oorspronkelijke richting, maar nu keert de voortplantingsrichting van het licht om. Passen we tot slot de operatie P toe dan hebben we een situatie die als twee druppels water lijkt op de oorspronkelijke, maar met twee verschillen: het atoom is vervangen door zijn antideeltje en de polarisatie van het licht is omgekeerd (in dit voorbeeld σ^-). CPT-invariantie zegt dus dat de frequentie van de σ^+ overgang in waterstof precies gelijk is aan die van de σ^- overgang voor het anti-atoom en dit kan experimenteel geverifieerd worden door beide deeltjes in een identieke magnetische val op te sluiten.

11.4 Ingrediënten voor koud antiwaterstof

Voordat positronen en antiprotonen samen een neutraal atoom kunnen vormen, moet het een en ander gebeuren. De antiprotonen worden aangeleverd met een energie die 10 ordes van grootte hoger is dan de waarde nodig om ze in te kunnen vangen in een Penning val. Deze energie (typisch enkele MeV) wordt met behulp van een verscheidenheid aan methodes gereduceerd tot enkele Kelvin (meV). De laatste stap van dit koelproces gaat als volgt: de Penning val is reeds gevuld met een wolk elektronen. Deze zijn zo licht dat ze via capacitieve koppeling hun energie dissiperen in een weerstand die in een bad vloeibaar helium hangt. Zeer snel komt dit ingevangen elektronengas in thermisch evenwicht met het vloeibaar helium. De antiprotonen koelen nu via botsingen met dit elektronengas.

Positronen kunnen door hun tegengestelde lading niet samen met antiprotonen in dezelfde Penning val worden gevangen. Het is wel mogelijk om de protonen in een tegengepoolde Penning val nabij die voor de antiprotonen te vangen. De positronenbron is een

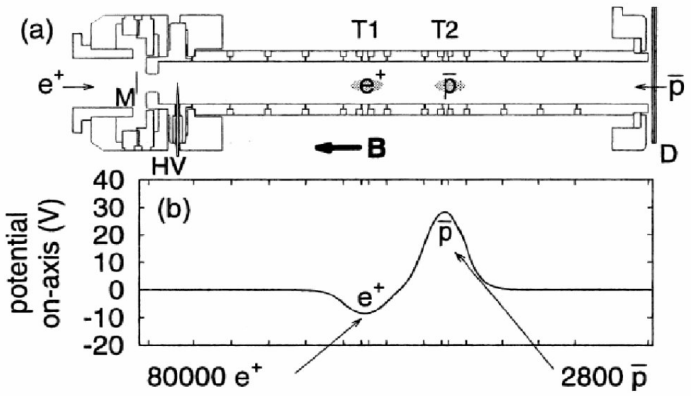

Figure 11.2: *Hybride Penning val waarin zowel antiprotonen als positronen ingevangen zijn, uit Ref. [94].*

radioactief preparaat (beta$^+$-straler). Ook hier geldt weer dat een enorme hoeveelheid energie moet worden gedissipeerd voordat de deeltjes in de Penning val ingevangen kunnen worden. Negen dagen voor het sluiten van de Low Energy Antiproton Ring (LEAR) in CERN, die laag-energetische antiprotonen leverde, werd door de TRAP samenwerking een alles of niets poging gedaan voor de productie van koud antiwaterstof. Veelbelovende hoeveelheden antiprotonen en positronen (meer dan een miljoen van elk) konden afzonderlijk worden ingevangen in een hybride Penning val (zie Fig 11.2). Het tegelijkertijd invangen van koude (4K) antiprotonen en positronen in deze ruimte leverde helaas van beide veel lagere aantallen op [94]. Vorming van anti-waterstof werd niet geobserveerd. Het openen van van de Antiproton Decelerator (AD) machine bij CERN in 1999 betekende een nieuwe start voor het antiwaterstofonderzoek door ATRAP en de concurerende ATHENA samenwerking.

Nu is het simpelweg samenbrengen van een positron met een antiproton ook niet voldoende om antiwaterstof te vormen. De reactie:

$$\overline{p} + e^+ \rightarrow \overline{H}$$

is niet mogelijk, omdat hierbij (bindings-)energie vrijkomt. Normaal gesproken kan de reactie daarom alleen plaatsvinden wanneer er een derde deeltje (foton, elektron of positron) aan de reactie deelneemt zodat de vrijkomende energie hieraan kan worden afgestaan. Dit proefschrift handelt over een nieuwe recombinatie-methode, die de betrokkenheid van een derde deeltje overbodig maakt [98, 99, 137] (Hoofdstuk 6-8). De methode maakt gebruik van recombinatie in een gepulst elektrisch veld ("Pulsed Field Recombination", PFR). Schematisch is de PFR-methode geschetst in Fig. 11.3. Zoals de figuur laat zien heeft de techniek veel overeenkomsten met het vangen van een wesp in een jampotje. Door op het juiste moment het potje dicht te klappen worden positronen gevangen in hoog aangeslagen ($n \approx 180$) toestanden (Rydberg-toestanden). Met koude Li atomen is aangetoond dat

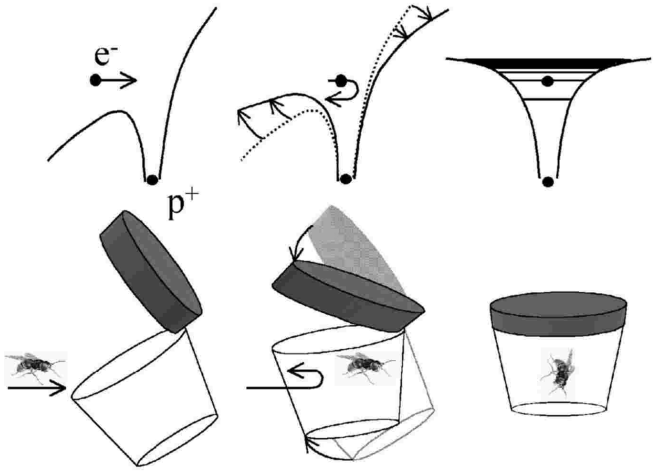

Figure 11.3: *Stel dat een elektron een ion nadert in een elektrisch veld, zo dat het elektron net over het veld-geïnduceerde zadelpunt komt in de Coulomb potentiaal. Uiteindelijk zal het elektron het ion weer verlaten over hetzelfde veld-geïnduceerde zadelpunt. Het elektron doet ongeveer 1 nanoseconde (10^{-9} s) over het omdraaien rond het ion. De crux van de recombinatie methode zit hem nu in het voldoende reduceren van het elektrisch veld wanneer het elektron dichtbij het ion is. Op deze manier eindigt het elektron onder het zadelpunt in een Rydberg-toestand en kan niet meer ontsnappen. Net zoals de wesp alleen in het jampotje zal worden gevangen als de deksel op het juiste tijdstip wordt dicht gedaan.*

de behaalde recombinatie efficiëntie (aantal gerecombineerde atomen/aantal vrije ionen $\approx 10^{-2}$, Hoofdstuk 7) ordes van grootte hoger is dan bij methodes waarbij een derde deeltje betrokken is. De eerste pogingen om met deze methode antiwaterstof te maken voor het ATRAP project, staan beschreven in Hoofdstuk 9.

Wanneer niet voorkomen kan worden dat de anti-atomen met de wand botsen, zullen ze maar kortstondig bestaan. Zodra het lukt om koud antiwaterstof te maken, wacht daarom direkt de volgende opgave om dit wandvrij op te sluiten. Met de wandvrije koeling en opsluiting van atomen is de afgelopen jaren dankzij laserkoeling technieken grote vooruitgang geboekt. Waterstofatomen kunnen bij voldoende lage temperaturen worden ingevangen in een statisch magneetveld en in situ worden bestudeerd met behulp van laserspectroscopie [142, 143]. Het combineren van een Penning val voor geladen deeltjes met een magnetische val voor atomen is nog niet experimenteel vertoond. Met een dergelijke val kan de eenmaal gevangen antimaterie in alle rust onderzocht worden naar zijn eigenschappen.

Bibliography

[1] J.R. Rydberg, Phil. Mag. 5^{th} Ser. **29**, 331 (1890);

[2] T.F. Gallagher, *Rydberg Atoms*, (Cambridge University Press, Cambridge, UK, 1994);

[3] D. You, R.R. Jones, P. H. Bucksbaum, Opt. Lett. **18**, 290 (1993);

[4] R. R. Jones, D. You, P.H. Bucksbaum, Phys. Rev. Lett. **70**, 1236 (1993);

[5] A. ten Wolde , L.D. Noordam, A. Lagendijk, H.B. van den Linden van den Heuvell, Phys. Rev. Lett. **61**, 2099 (1988);

[6] J.A. Yeazell, M. Mallalieu, C.R. Stroud, Jr., Phys. Rev. Lett. **64**, 2007 (1990);

[7] G.M. Lankhuijzen, L.D. Noordam, Phys. Rev. Lett. **76**, 1784 (1996);

[8] W.C. Röntgen, Nature **53**, 274 (1896);

[9] H.A. Bethe, E.E. Salpeter, *Quantum Mechanics of One and Two Electron Atoms* (Springer-Verlag, Berlin, 1957);

[10] D.R. Bates, A. Dalgarno, *Atomic and Molecular processes* (Academic Press, New York, 1962);

[11] G. Gabrielse, S.L. Rolston, L. Haarsma, W. Kells, Phys. Lett. A **129**, 38 (1988);

[12] H.S.W. Massey, D.R. Bates, Rep. on Progr. in Phys. **9**, 62 (1942);

[13] *Recombination of Atomic Ions*, edited by W.G. Graham, W. Fritsch, Y.Hahn, J.A, Tanis, (Plenum Press, New York 1992);

[14] A. Müller, A. Wolf, Hyp. Int. **109**, 233 (1997);

[15] R. Flannery, *Atomic, Molecular, and Optical Physics Handbook*, (AIP Press, Woodburry, NY, 1996);

[16] F.B. Yousif, P. van der Donk, Z. Kucherovsky, J. Reis, E. Brannen, J.B.A. Mitchell, Phys. Rev. Lett. **67**, 26 (1991);

[17] U. Schramm , J. Berger, M. Grieser, D. Habs, E. Jaeschke, G. Kilgus, D. Schwalm, A. Wolf, R. Neumann, R. Schuch, Phys. Rev. Lett. **67**, 22 (1991);

[18] M.L. Rogelstad, F.B. Yousif, T.J. Morgan, J.B.A. Mitchell, J. Phys. B **30**, 3913 (1997);

[19] K.K. Darrow, *Electrical Phenomena in Gasses*, (Williams and Wilkins, Baltimore, 1932);

[20] A. Muller, Comm. At. Mol. Phys. **3**, 143 (1996);

[21] C.D. Anderson, Science **76**, 238 (1932);

[22] C.D. Anderson, Phys. Rev. **43**, 491 (1933);

[23] D.R. Bates, A.E. Kingston, R.W.P Mc Whirter, Proc. R. Soc. A **267**, 297 (1962);

[24] B. Makin, J. Keck, Phys. Rev. Lett. **11**, 281 (1963);

[25] J. Stevelt, J. Boulmer, J.F. Delpech, Phys. Rev. A **12**, 1246 (1975);

[26] G. Baur, G. Boero, S. Brauksiepe, A. Buzzo, W. Eyrich, R. Geyer, D. Grzonka, J. Hauffe, K. Killian, M. LoVetere, M. Macri, M. Moosburger, R. Nellen, W. Oelert, S. Passaggio, A. Pozzo, K. Röhrich, K. Sachs, G. Schepers, T. Sefzick, R.S. Simon, R. Stratmann, F. Stinzing, M. Wolke, Phys. Lett. B **368**, 251 (1996);

[27] M. Niering, R. Holzwarth, J. Reichert, P. Pokasov, Th. Udem, M. Weitz, T.W. Hänsch, P. Lemonde, G. Santarelli, M. Abgrall, P. Laurent, C. Salomon, A. Clairon, Phys. Rev. Lett. **84**, 5496 (2000);

[28] http://hussle.harvard.edu/~atrap/;

[29] T.F. Gallagher, L.M. Humphrey, R.M. Hill, S.A. Edelstein, Phys. Rev. Lett. **37**, 1465 (1976);

[30] T.F. Gallagher, L.M. Humphrey, W.E. Cooke, S.A. Edelstein, R.M. Hill, Phys. Rev. A **16**, 1098 (1977);

[31] J.L. Vialle, H.T. Duong, J. Phys. B **12**, 1407 (1979);

[32] G. Leuchs, H. Walter, Z. Phys. A **293**, 93 (1979);

[33] T.H. Jeys, G.W. Foltz, K.A. Smith, E.J. Beiting, F.G. Kellert, F.B. Dunning, R.F. Stebbings, Phys. Rev. Lett. **44**, 390 (1980);

[34] J.H.M. Neijzen, A. Donszelmann, J. Phys. B **15**, L87 (1982);

[35] F.B. Dunning, R.F. Stebbings, *Rydberg states of atoms and molecules*, (Cambridge University Press, Cambridge, 1983);

[36] L.G. Gray, K.B. MacAdam, J. Phys. B **27**, 3055 (1994);

[37] K. Muller-Dethlefs, M. Sander, E.W. Schlag, Chem. Phys. Lett. **112**, 291 (1984);

[38] E.W. Schlag, *ZEKE Spectroscopy*, (Cambridge University Press, Cambridge, UK, 1998);

[39] D.A. Harmin, P.N. Price, Phys. Rev. A **49**, 1933 (1994);

[40] D.A. Harmin, Phys. Rev. A **56**, 232 (1997);

[41] G.M. Lankhuijzen, L.D. Noordam, Phys. Rev. Lett. **74**, 335 (1995);

[42] D.A. Harmin, Phys. Rev. A **26**, 2656 (1982);

[43] T. Yamabe, A. Tachibana, H.J. Silverstone, Phys. Rev. A **16**, 877 (1977);

[44] D. Banks, J.G. Leopold, J. Phys. B **11**, L5 (1978);

[45] C. O. Reinold, M. Melles, H. Shao, J. Burgdörfer, J. Phys. B **19**, L659 (1993);

[46] N.E. Tielking, T.J. Bensky, R.R. Jones, Phys. Rev. A **51**, 3370 (1995);

[47] J. Bromage, C.R. Stroud, Phys. Rev. Lett. **83**, 4963 (1999);

[48] M.W. Noel, W.M. Griffith, T.F. Gallagher, Phys. Rev. Lett. **83**, 1747 (1999);

[49] J.H. Hoogenraad, R.B. Vrijen, L.D. Noordam, Phys. Rev. A **50**, 4133 (1994);

[50] F. Robicheaux, C. Wesdorp, L.D. Noordam, Phys. Rev. A **62**, 43404 (2000);

[51] W. Sandner, K.A. Safinya, T.F. Gallagher, Phys. Rev. A **33**, 1008 (1986);

[52] D.W. Schumacher, B.J. Lyons, T.F. Gallagher, Phys. Rev. Lett **78**, 4359 (1997);

[53] B.J. Lyons, D.W. Schumacher, D.I. Duncan, R.R. Jones, T.F. Gallagher, Phys. Rev. A **57**, 3712 (1998);

[54] G.M. Lankhuijzen, L.D. Noordam, Phys. Rev. A **55**, 2016 (1995);

[55] D.A. Harmin, Phys. Rev. A **24**, 2491 (1981);

[56] F. Robicheaux, J. Shaw, Phys. Rev. A **56**, 278 (1997);

[57] F. Robicheaux, J. Shaw, Phys. Rev. Lett. **77**, 4154 (1996);

[58] L.D. Noordam, R.R. Jones, Journal of Modern Optics **44**, 2515 (1997);

[59] F. Robicheaux, C. Wesdorp, L.D. Noordam, Phys. Rev A **60**, R3377 (1999);

[60] D.A. Harmin, Comm. At. Mol. Phys. **15**, 281 (1985);

[61] W.E. Ernst, T.P. Softley, R.N. Zare, Phys. Rev. A **37**, 4172 (1988);

[62] A. König, J. Neukammer, H. Hieronymous, H. Rinneberg, Phys. Rev. A **43**, 2402 (1991);

[63] D.J. Armstrong, C.H. Greene, R.P. Wood, J. Cooper, Phys. Rev. Lett. **70**, 2379 (1994);

[64] D.J. Armstrong C.H. Greene, Phys. Rev. A **50**, 4956 (1994);

[65] T.P. Softley, A.J. Hudson, R. Watson, J. Chem. Phys. **106**, 1041 (1997);

[66] U. Fano, Phys. Rev. **124**, 1866 (1961);

[67] G. M. Lankhuijzen, L. D. Noordam, Opt. Commun. **129**, 361 (1996);

[68] A. ten Wolde, L.D. Noordam, A. Lagendijk, H.B. van Linden van den Heuvell, Phys. Rev. A **40** , 485 (1989);

[69] R.G. Rolfes, D.B. Smith, K.B. MacAdam, J. Phys. B: At. Mol. Phys. **16**, L535-L538 (1983);

[70] D.R. Mariani, W. van de Water, P.M. Koch, T. Bergeman, Phys. Rev. Lett. **17**, 1261 (1983);

[71] H.B. van Linden van den Heuvell, R. Kachru, N.H. Tran, T.F. Gallagher, Phys. Rev. Lett. **20**, 1901 (1984);

[72] H.B. van Linden van den Heuvell, T.F. Gallagher, Phys. Rev. A **32**, 1495 (1985);

[73] T.F. Gallagher, C.R. Mahon, P. Pillet, Panming Fu, J. B. Newman, Phys. Rev. A **39**, 4545 (1989);

[74] P. Pillet, H.B. van Linden van den Heuvell, W.W. Smith, R. Kachru, N.H. Tran, T.F. Gallagher, Phys. Rev. A **30**, 280 (1984);

[75] P. Kristensen, G.M. Lankhuijzen, L.D. Noordam, J. Phys. B: At. Mol. Opt. Phys. **30**, 1481 (1997);

[76] G.M. Lankhuijzen, L.D. Noordam, Phys. Rev. Lett. **74**, 335 (1995);

[77] M. Gatzke, B. Broers, L.D. Noordam, R.B. Watkins, T.F. Gallagher, Phys. Rev. A **50**, 2502 (1994);

[78] T.J. Bensky, M.B. Campbell, R.R. Jones, Phys. Rev. Lett. **81**, 3112 (1998);

[79] B. Broers, J.F. Christian, J.H. Hoogenraad, W.J. van der Zande, H.B. van Linden van den Heuvell, L.D. Noordam, Phys. Rev. Lett. **71**, 344 (1993);

[80] M. Gavrila, *Atoms in Intense Laser Fields*, (Academic Press Limited, London, first edition, 1992);

[81] T.F. Gallagher, Phys. Rev. Lett. **20**, 2304 (1988);

[82] T.F. Gallagher, T.J. Scholz, Phys. Rev. A **40**, 2762 (1989);

[83] B.I. Greene, J.F. Federici, D.R. Dykaar, R.R. Jones, P. H. Bucksbaum, Appl. Phys. Lett. **59**, 8 (1991);

[84] V.L. Jacobs, J. Davis, P.C. Kepple, Phys. Rev. Lett. **37**, 1390 (1976);

[85] V.L. Jacobs, J. Davis, Phys. Rev. A **19**, 776 (1979);

[86] A. Müller, B.S. Belic, B.D. DePaola, N. Djuric, G.H. Dunn, D.W. Mueller, C. Timmer, Phys. Rev. Lett. **56**, 127 (1986);

[87] F. Robicheaux, M. S. Pindzola, Phys. Rev. Lett. **79**, 2237 (1997);

[88] L. Ko, V. Klimenko, T.F. Gallagher, Phys. Rev. A **59**, 2126 (1999);

[89] D.R. Bates, Phys. Rev. **77**, 718 (1950);

[90] E.A. Hessels, D.M. Homan, M.J. Cavagnero, Phys. Rev. A **57**, 1668 (1998);

[91] D. Klar, M-W Ruf, H. Hotop, Meas. Sci. Technol. **5**, 1248 (1994);

[92] G. Blanford, D.C. Christian, K. Gollwitzer, M. Mandelkern, C.T. Munger, J. Schultz, G. Zioulas, Phys. Rev. Lett. **80**, 3037 (1998);

[93] J. Walz, S.B. Ross, C. Zimmermann, L. Ricci, M. Prevedelli, T.W. Hansch, Phys. Rev. Lett. **75**, 3257 (1995);

[94] G. Gabrielse, D.S. Hall, T. Roach, P. Yesley, A. Khabbaz, J. Estrada, C. Heimann, H. Kalinowsky, Phys. Lett. B **455**, 311 (1999);

[95] *Non-Neutral Plasma Physics III*, edited by J.J. Bollinger, R.L. Spencer, R.C. Davidson, (AIP Conf. Proc., Princeton, New Jersey, 1999);

[96] C. Desfrancois, H. Abdoul-Carime, J-P Schermann, Int. J. Mod. Phys. B **10**, 1339 (1996);

[97] J.D.D. Martin, J. W. Hepburn, Phys. Rev. Lett **79**, 3154 (1997);

[98] C. Wesdorp, F. Robicheaux, L. D. Noordam, Phys. Rev. Lett **84**, 3799 (2000);

[99] C. Wesdorp, F. Robicheaux, L.D. Noordam, Chem. Phys. Lett. **323**, 192 (2000);

[100] *Niels Bohr and the Development of Physics*, edited by W. Pauli, p. 30 (Pergamon Press, New York, 1955);

[101] J.S. Bell, Proc. Roy. Soc. **A231**, 491 (1955);

[102] R. Jost, *The General Theory of Quantised Fields* (Am. Math. Soc., Providence, 1965);

[103] A. Einstein, Jahrb. Rad. Elektr. **4**, 411 (1907);

[104] C.M. Will, *Theory and experiment in Gravitational Physics* (Cambridge University Press, Cambridge, 1981);

[105] D.P. Taylor, J.G. Goode, J.E. LeClaire, P.M. Johnson, J. Chem. Phys. **103**, 14 (1995);

[106] A. Fujii, A. Iwasaki, T. Ebata, N. Mikami, J. Phys. Chem. **101**, 5963 (1997);

[107] M. Gerhards, M. Schiwek, C. Unterberg, K. Kleinermanns, Chem. Phys. Lett. **297**, 515 (1998);

[108] D. Wineland, P. Ekstrom, H. Dehmelt, Phys. Rev. Lett. **31**, 1279 (1973);

[109] D.J. Wineland, H.G. Dehmelt, J. Appl. Phys. **46**, 919 (1975);

[110] G. Gabrielse, Phys. Rev. A **27**, 2277 (1983);

[111] C.S. Weimer, J.J. Bollinger, F.L. Moore, D.J. Wineland, Phys. Rev. A **49**, 3842 (1994);

[112] L. Zhu, P.M. Johnson, J. Chem. Phys. **94**, 5769 (1991);

[113] H. Yasumatsu, T. Kondow, H. Kitagawa, K. Shobatake, J. Chem. Phys. **104**, 899 (1996);

[114] E.B. Gallogly, Yiham-Bao, Keli-Han, Hua-Lin, W.M. Jackson, J. Phys. Chem. **98**, 3121 (1994);

[115] G. von Helden, I. Holleman, G.M.H. Knippels, A.F.G. van der Meer, G. Meijer, Phys. Rev. Lett. **79**, 5234 (1997);

[116] D.S. Hall, G. Gabrielse, Phys. Rev. Lett. **77**, 1962 (1996);

[117] P. Wurz, K.R. Lykke, J. Chem. Phys. **95**, 7008 (1991);

[118] E.E.B. Campbell, R.D. Levine, accepted for publication in Ann. Rev. Phys. Chem.;

[119] K. Hansen, O. Echt, Phys. Rev. Lett. **12**, 2337 (1997);

[120] E.E.B. Campbell, G. Ulmer, I.V. Hertel, Phys. Rev. Lett. **67**, 1986 (1991);

[121] M.R. Pederson, A.A. Quong, Phys. Rev. B **46**, 13584 (1992);

[122] A.A. Scheidemann, V.V. Kresin, W.D. Knight, Phys. Rev. A **49**, R4293 (1994);

[123] W.A. Chupka, J. Chem. Phys. **98**, 4520 (1993);

[124] D.L. Dorofeev, B.A. Zon, J. Chem. Phys. **106**, 9609 (1997);

[125] F. Merkt, R.N. Zare , J. Chem. Phys **101**, 3495 (1994);

[126] P.A.M. Dirac, *The Principles of Quantum Mechanics*, (4th ed. Oxford University Press, Oxford 1958);

[127] L.S. Brown, G. Gabrielse, Rev. Mod. Phys. **58**, 233 (1986);

[128] J. Estrada, T. Roach, J.N. Tan, P. Yesley, G. Gabrielse, Phys. Rev. Lett. **84**, 859 (2000);

[129] D.J. Wineland, H.G. Dehmelt, Intl. J. of Mass Spec. and Ion Phys. **16**, 338 (1975);

[130] D.S. Hall, *Positrons, Antiprotons, and Interactions for Cold Antihydrogen*, (thesis, Harvard University 1997);

[131] D. Möhl, G. Petrucci, L. Thorndahl, S. van der Meer, Phys. Rep. **58**, 74 (1980);

[132] S. van der Meer, *Physics of Particle Accelerators*, p. 1628 (edited by M. Month and M. Dienes, AIP Conf. Proc. No. 153, AIP, New York, 1987);

[133] D.S. Hall, G. Gabrielse, Phys. Rev. Lett. **77**, 1962 (1996);

[134] D.H.E. Dubin, Physics of Fluids B **5**, 295 (1993);

[135] J.J. Bollinger, D.J. Heinzen, F.L. Moore, W.M. Itano, D.J. Wineland, D.H.E. Dubin, Phys. Rev. A **48**, 525 (1993);

[136] D.H.E. Dubin, T.M. O'Neil, Phys. Rev. lett. **60**, 511 (1988);

[137] C. Wesdorp, F. Robicheaux, L. D. Noordam, in preparation;

[138] G. Wiebusch, J. Main, K. Krüger, H. Rottke, A. Holle, K. H. Welge, Phys. Rev. Lett. **62**, 2821 (1989);

[139] Simion V 6.00, Lockheed Martin Idaho Technologies, Idaho National Engineering Laboratory, United States (1996);

[140] G. Gabrielse, D. Phillips, W. Quint, H. Kalinowsky, T. Trainor, W. Kells, Phys. Rev. Lett. **74**, 3544 (1995);

[141] G. Gabrielse, A. Khabbaz, D.S. Hall, C. Heimann, H. Kalinowsky, W. Jhe, Phys. Rev. Lett. **82**, 3198 (1999);

[142] O.J. Luiten, H.G.C. Werij, I.D. Setija, M.W. Reynolds, T.W. Hijmans, J.T.M. Walraven, Phys. Rev. Lett. **70**, 544 (1993);

[143] K.S.E. Eikema, J. Walz, T.W. Hänsch, Phys. Rev. Lett. **83**, 3828 (1999).

Nawoord

Het individuele karakter van een proefschrift is allerminst een maat voor het aantal mensen die eraan hebben meegewerkt. Het is eerder uitzondering dan regel dat een promovendus alleen aan een experimentele opstelling werkt. Bovendien wordt op AMOLF de samenwerking tussen verschillende groepen gestimuleerd en zijn er talrijke interne samenwerkingsverbanden.

Mijn promotor, Bart Noordam, heeft een centrale rol vervuld in de realisatie van dit boekje. Dit boekje handelt bijvoorbeeld over een nieuwe recombinatie-methode die volledig bedacht is door Bart Noordam. Een aantal jaar terug schetste hij de methode op een velletje en liet deze zien aan een theoreticus. De theoreticus kon nog net zijn lachen bedwingen en meldde dat het een kansloos project was. Niet ontmoedigd werd er toch een poging gewaagd en twee jaar later, toen het experiment was gelukt, moest dezelfde theoreticus toegeven dat dit (ook in theorie) een zeer krachtige recombinatie-methode was.

De theoreticus was niemand minder dan Francis Robicheaux. Francis Robicheaux and Bart Noordam form an unbeatable team in atomic physics. Almost every week I wrote Francis Robicheaux an e-mail with questions relating to atomic physics. An average reply from a theoretician then would be so cryptic that the answer would be useless. Francis Robicheaux, in contrast, would come up with a clear answer always starting with: "an easy way of seeing this ...".

Speciaal wil ik Huib Bakker, Tom Hijmans en Wim van der Zande bedanken voor het doorlezen en beoordelen van diverse manuscripten. Het overleg met de groep van Tom Hijmans binnen het anti-waterstofproject is heel nuttig geweest. Vooral de gesprekken over CPT-symmetrie waren zeer interessant. De kritische kijk van Wim van der Zande op een experiment is bijzonder waardevol en het hardlopen met hem was een prettige afleiding om de frustraties die bij het experimenteren horen kwijt te raken.

Het niet wetenschappelijke hoogtepunt van mijn promotie was de aanschaf van de espressomachine met Marcel Warntjes en Andreas Guertler, ook al heeft dit geleid tot een hardnekkige cafeïneverslaving. Bovendien resulteerde de samenwerking met Marcel en Andreas vaak ook tot wetenschappelijke successen en interessante discussies. Afric, Andreas en Anouk: veel succes met de experimenten.

It has been a great pleasure to work at CERN for two months. This was a very intriguing period, not only because of working with anti-matter, but also because it was the first time I worked in a large collaboration. I would especially like to thank Gerald Gabrielse, Walter Oelert, George Schepers, Joseph Tan, Peter Yesley, and John Estrada with whom I have worked closely during these two months.

De technische ondersteuning op AMOLF is perfect geweest. Ik heb gedurende mijn promotie de kamer van Rob Kemper en Hinco Schoenmaker platgelopen voor advies en om te vragen of ze weer een nieuwe opstelling konden bouwen. Hinco is niet alleen betrokken geweest bij het bouwen van opstellingen maar heeft ook geholpen bij het verkrijgen van de experimentele resultaten die beschreven staan in Hoofdstuk 7. Het ontwerpen van een nieuwe opstelling is tot een kunst verheven door Dick Glastra van Loon. Met zijn

hulp is het mogelijk geweest om een complex idee om te toveren tot een realiseerbare opstelling. Daarnaast heb ik ook veel steun gekregen van de E&I afdeling, voor het advies op gebied van PC's, electronica en het bouwen van complexe schakelingen. Met name Dennis Driessen, Duncan Verheijde en Idsart Attema ben ik veel dank verschuldigd.

Deze enorme academische ondersteuning zou echter niet voldoende geweest zijn om de klus te klaren, ware het niet dat ik veel steun ontving van het "thuis-front". Met name wil ik Ester, mijn ouders en mijn kleine zusje bedanken: jullie hielpen me door dips en luisterde naar mijn vaak onbegrijpelijke geleuter over de Natuurkunde. In het bijzonder wil ik mijn grootmoeder bedanken die me heeft geleerd door te gaan als de omstandigheden moeilijk worden, ik weet zeker dat ze daardoor flink heeft bijgedragen tot mijn promotie.

Kees